2006

The Effect Of Stationary UV Excitation On The Optical Behavior Of Electrochemically Self-Assembled Semiconductor Nanowires

Rajesh A. Katkar
Virginia Commonwealth University

THE EFFECT OF STATIONARY UV EXCITATION ON THE OPTICAL BEHAVIOR OF ELECTROCHEMICALLY SELF-ASSEMBLED SEMICONDUCTOR NANOWIRES

A Dissertation submitted in partial fulfillment of the requirements for the degree of Doctor of Philosophy at Virginia Commonwealth University

by

RAJESH A. KATKAR
B.E., Electrical Engineering, National Institute of Technology, Nagpur, India, 2000
M.S., Engineering, Virginia Commonwealth University, 2003

Director: DR. GREGORY B. TAIT
ASSOCIATE PROFESSOR, ELECTRICAL AND COMPUTER ENGINEERING

Virginia Commonwealth University
Richmond, Virginia
November, 2006

Acknowledgements

A senior colleague once told me that to finish a doctorate, one not only require being very hardworking, but also extremely patient. He didn't mention about any intellectual abilities though. At the end of this long journey, I understood what he exactly meant. During my Ph.D. studies, I went through lots of academic and mental ups and downs. I want to thank everybody who supported me in any aspect during this period.

First and foremost, I thank my parents, my Aai-Baba, who always seemed to be very close to me, even though they were thousands of miles away in India. I thank them for their unconditional love and faith in me. I also thank my brothers, Ajay and Vijay dada, and my sister-in-laws, Mrinal and Anjali Vahini, for supporting me throughout this period. There wasn't a single day passed when I didn't remember Aboli, Ashay and Aswin, the adorable kids in the family.

It was extremely difficult to stay away from such a loving family, and very frustrating not to be able to meet them very often. But my friends made the stay not only easier, but a memorable one. I thank Laxmikant, Sunil, Amol, Naveen and Nagesh for a such a nice time. With them, it was like a home away from home. I would treasure all the happy moments we shared together for all my life. Richmond would always remain a sweet memory. To me, it's the second best city after my hometown, Nagpur.

I thank Dr. Gregory Tait to be my advisor. He taught me everything that I know in the field of Optics and Photonics. I seriously feel that he was the best and the nicest teacher I ever had. I thank him for his support and faith in me.

I would also like to thank Shiva who spent a lot of time to provide a large amount of nanowire samples for my experiments. I also thank all those people who directly or indirectly helped me to perform my work.

Although His existence is questionable to some people in the Science community, I believe in God and thank him for all my accomplishments.

Table of Contents

Page

Acknowledgements ii

List of Tables vii

List of Figures viii

Abstract xii

Chapter

1 Introduction 1

2 Fundamentals 12

2.1 Low Dimensional systems: *1-D* regime 12

2.2 Overview of the typical optical parameters 15

2.3 Excitons 20

2.4 Phenomenon of Interference 26

2.5 Fabrication of the electrochemically self-assembled semiconductor quantum wire array 30

3 Theoretical Modeling 35

3.1 Atomic Optical Susceptibility 36

3.2 Free carrier transitions in a semiconductor crystal 40

3.2.1 Optical dipole matrix 40

3.2.2 Optical inter-band transitions in a semiconductor crystal 43

3.2.3 Quasi-Equilibrium regime in a semiconductor crystal 47

3.3 Inter-band transitions with Coulomb effects: Low excitation regime 51

3.3.1 Hamiltonian 53

3.3.2 Inter-band polarization function 56

3.4 The situation of an unexcited quantum wire: The linear optical properties 57

3.4.1 Bound States (or excitons where $E_{bound} < E_g$) 61

3.4.2 Continuum (ionized) states where $E_v \geq 0$ 63

3.4.3 Optical spectra of quantum wires 64

3.5 High optical excitation condition: Quasi-equilibrium regime 66

3.5.1 Accelerated Fixed Point (AFP) method 71

3.5.2 Pade approximation method 72

3.6 Numerical calculations using Mathematica 74

4 Electromagnetic Wave Simulations 95

4.1 High Frequency Structure Simulation (HFSS) 95

4.2 Major building blocks of *HFSS* 97

4.2.1 Solution type 97

4.2.2 Boundary Conditions 98

4.2.3 Excitations 102

4.2.4 Analysis, Solution Setup, Solve loop and Results 103

4.3 Geometric model of the quantum wire array.....106

4.4 Final simulations for the quantum wire array 111

5 Experimental Analysis.....116

5.1 Theoretical basis for the experiment 116

5.2 Effective amplification of the change in phase-difference.....121

5.3 Initial biasing of the interferometer.....124

5.4 Experimental Setup 127

5.5 Experimental Procedures.....142

6 Results and Discussion.....151

6.1 The plausible sources of size-dependent non-monotonic optical behavior.....151

6.1.1 Screening effects 152

6.1.2 Phase space filling effect.....153

6.1.3 Dielectric confinement and image potentials 154

6.1.4 Direction of optical field polarization 156

6.1.5 Quantum confined Stark effect.....157

6.1.6 Interface states, Fermi level pinning, and built-in field effects..160

6.1.7 Quantum confinement effect.....161

6.1.8 The effect of filling factor 164

6.2 Experimental Data Analysis.....165

6.3 Mathematica and HFSS output.....180

7 Summary and Conclusion 188

List of References.....193

VITA.....206

List of Tables

Page

Table 1: Material parameters for quantum wire semiconductor materials. 81

Table 2: Static dielectric constant of the quantum wire semiconductor materials at *0.95 eV* at (*1308 nm*) and *300* ^{0}K in bulk. 83

Table 3: Optical parameters calculated for *CdS* using Mathematica. 85

Table 4: Optical parameters calculated for *ZnSe* using Mathematica. 86

Table 5: Optical parameters calculated for *ZnO* using Mathematica. 87

Table 6: Optical parameters calculated for *CdSe* using Mathematica. 88

Table 7: Wire diameter and inter-pore separation. 107

Table 8: Real part of permittivity (ε') and dielectric loss tangent values calculated using *Mathematica* for unexcited quantum wires and utilized as an important material parameter in *HFSS*. 112

Table 9: Phase shift of the probe wave (1308 nm) as it passes through the unpumped quantum wire array, as calculated in *HFSS*. 114

Table 10: LED Forward Current vs the *ac* component of the detector output (*in* μV) for *UV* excited *CdS* and *ZnSe* quantum wire arrays. 147

Table 11: LED Forward Current vs the *ac* component of the detector output (*in* μV) for *UV* excited *ZnO* and *CdSe* quantum wire arrays. 148

Table 12: Changes in the optical parameters as calculated in HFSS and Mathematica for *CdS* and *CdSe* quantum wires. 183

Table 13: Changes in the optical parameters as calculated in HFSS and Mathematica for *ZnO* and *ZnSe* quantum wires. 184

List of Figures

Page

Figure 1.1: Density of states function of a 1-Dimensional system.....2

Figure 1.2: Raw atomic force micrograph of a porous alumina film 4

Figure 2.1: The statistical distribution of density of states for *2-D, 1-D* and *0-D* semiconductor structure plots as a function of energy.....13

Figure 2.2: The infinitely deep rectangular cross section of quantum wire 14

Figure 2.3: Optical spectra of a semiconductor near fundamental edge.....20

Figure 2.4: *E-k* relation for Wannier excitons 22

Figure 2.5: *Wannier* and *Frenkel* type of excitons 25

Figure 2.6: Superposition of two waves with phase difference $\Delta\varphi$.....26

Figure 2.7: Michelson, Mach-Zehnder and Sagnac interferometers. Waves travel via different paths and path lengths to form an interference pattern 28

Figure 2.8: Different stages in the fabrication process of porous Alumina.
(A) Growth of Aluminum Oxide,
(B) Fine featured pores being developed,
(C) Enhanced pore growth,
(D) Ultimate pore structure.
D is the inter-pore separation, *d* denotes pore diameter, and *L* is the depth of the pores.....31

Figure 2.9: Ideal structure of anodic porous aluminum oxide.....32

Figure 2.10: SEM image of the porous alumina template 33

Figure 3.1: *E-k* diagram (momentum conservation).....43

Figure 3.2: *Quasi-1D* Coulomb Potential 58

Figure 3.3: Lateral confinement energy (in *meV*) for quantum wires of different materials and diameters, including *100/50/25/15/10/5 nm* 89

Figure 3.4: Variation of unexcited quantum wire permittivity with diameters 90

Figure 3.5: Real part of Permittivity vs Confinement energy variations with diameter for unexcited CdS wires 91

Figure 3.6: Variations in dielectric loss tangent with the quantum wire diameters 92

Figure 3.7: Variations in the refractive index (n) and absorption coefficient (α) of the quantum wires with their diameters 94

Figure 4.1: Block diagram for the HFSS Simulator 96

Figure 4.2: A quantum wire array device: A periodic geometric structure 99

Figure 4.3: Master and Slave surfaces of a hexagonal unit cell 100

Figure 4.4: Wave-port type of excitation 102

Figure 4.5: Adaptive mesh generation 104

Figure 4.6: *SEM* image of quantum wires of *50-nm* diameter. The black spots indicate the quantum wires 108

Figure 4.7: Unit cells that would generate a quantum wire array when placed with a specific periodicity 109

Figure 4.8: The quantum wire array formed using rectangular and hexagonal unit cells 110

Figure 5.1: The interference situation 121

Figure 5.2: Michelson Interferometer 125

Figure 5.3: Bias point on the interference curve 126

Figure 5.4: Pump-probe excitation scheme 128

Figure 5.5: Experimental Setup 130

Figure 5.6: *UV LED* (All dimensions are in *mm*) 133

Figure 5.7: *LED* modulation circuit 134

Figure 5.8: Forward current (I_{diode}) vs *UV LED* power (*mW*) calibration curve 136

Figure 5.9: Detection of the *ac* component 138

Figure 5.10: Photograph of experimental setup 142

Figure 5.11: The Acquire data acquisition plot 146

Figure 5.12: *ac* component (in μV) detected by the lock-in amplifier for four different *10-nm* diameter *UV* excited *ZnSe* quantum wire array samples ..149

Figure 5.13: IR probe laser power vs photodetector voltage calibration curve 150

Figure 6.1: Electric field lines in quantum wire 152

Figure 6.2: Changes in the DOS function with the reduction in wire diameter 162

Figure 6.3: Changes in phase shifts induced by *UV* light in *CdS* quantum wire array 166

Figure 6.4: Changes in phase shifts induced by *UV* light in *ZnO* quantum wire array 167

Figure 6.5: Changes in phase shifts induced by *UV* light in *ZnSe* quantum wire array 168

Figure 6.6: Changes in phase shifts induced by *UV* light in *CdSe* quantum wire array 169

Figure 6.7: Changes in phase shifts as function of wire diameter. The values displayed here are the changes observed at *1.2 mW* of *UV* excitation as a function of wire diameters 171

Figure 6.8: Changes in refractive index as function of wire diameter. The values displayed here are the changes observed at *1.2 mW* of *UV* excitation as a function of wire diameters 172

Figure 6.9: Normalized changes in phase shifts $\Delta\eta$. The plot shows the normalized variations in the phase changes observed by *25 nm* diameter samples as compared to *50 nm* diameter samples,

for all four materials, as a function of *UV* Power. $\Delta\eta$ values are calculated as $\%\left[\delta\varphi(25)-\delta\varphi(50)\right]/\,\delta\varphi(50)$ 173

Figure 6.10: Changes in phase shifts vs wire diameters as a function of *UV excitation* Power in *ZnO* quantum wire array.....174

Figure 6.11: The normalized changes in phase shifts $\Delta\eta$ observed by *10-nm* diameter samples as compared to *25-nm* diameter samples, for all four materials, as a function of *UV* Power. $\Delta\eta$ values are calculated as $\%\left[\delta\varphi(25)-\delta\varphi(10)\right]/\,\delta\varphi(25)$ 176

Figure 6.12: 1-dimensional density of states as a function of wire diameter 177

Figure 6.13: Absorption spectra of ZnO quantum wire array.....178

Figure 6.14: Electric field distribution inside the unit cell of a *50-nm* diameter *CdS* nanowire array structure. Circular semiconductor wire is embedded inside the hexagonal alumina.....181

Figure 6.15: Changes in the real part of permittivity $\Delta\mathrm{Re}(\varepsilon)$ of the quantum wire as calculated using HFSS to match experimentally observed phase shift changes at *1.2 mW* of *UV* pump power.....182

Figure 6.16: Changes in the real parts of permittivity of all quantum wires at various *UV* pump powers as calculated using experimental data and *HFSS* 185

Figure 6.17: Variations in the theoretically calculated (a) real and (b) imaginary parts of the permittivity (ε) as functions of quantum wire diameter in the absence of pump. 186

Abstract

THE EFFECT OF STATIONARY UV EXCITATION ON THE OPTICAL BEHAVIOR OF ELECTROCHEMICALLY SELF-ASSEMBLED SEMICONDUCTOR NANOWIRES

By Rajesh A. Katkar, M.S.

A Dissertation submitted in partial fulfillment of the requirements for the degree of Doctor of Philosophy at Virginia Commonwealth University.

Virginia Commonwealth University, 2006

Major Director: Dr. Gregory B. Tait
Associate Professor, Electrical and Computer Engineering

In this work, we investigate the optical response of the semiconductor quantum wire array when excited by stationary *UV* light. The array is synthesized by selectively electro-depositing the semiconductor material in electrochemically self-assembled porous alumina templates. Our studies are based on the optical behavioral changes in *CdS, ZnO, ZnSe* and *CdSe* quantum wires of *50-, 25-* and *10-nm* diameters.

We use a set of generalized Bloch equations to solve the interband polarization function of the semiconductors derived within the Hartree-Fock approximation, and theoretically model the *UV* excitation effect on the quantum wires. The solutions which

consider the effects of screening, Coulomb interaction between the carriers and many body effects on excitons are generated for a *quasi-equilibrium* regime using a devised accelerated fixed point method. The solution technique is developed in Mathematica to iteratively solve this complex set of equations. The optical constants generated for individual quantum wires are incorporated into a finite-element electromagnetic wave simulator, *HFSS*, to investigate the full behavior of the array of wires. Theoretically calculated values of the dielectric permittivity of the un-excited quantum wires are shown to decrease progressively as the wire diameter reduces.

We perform the experimental analysis using a pump-probe excitation scheme incorporated in a sensitive Michelson interferometer in a homodyne setup. We measure extremely small changes in the phase shift between the interfering *IR* probe beams and hence measure the refractive index changes caused by the *UV* pump. While the decreasing filling factor acts to reduce the optical activity in narrower wire arrays, the shifting of the DOS function with additional quantum confinement serves to increase it. These competing effects give rise to the size-dependent non-monotonic optical activity experimentally observed in *ZnO, CdS* and *ZnSe* nanowire arrays. The simulation results show a rapid increase in the changes in effective permittivity values of the individual quantum wires as diameter decreases. The substantial changes observed in the refractive index for the whole thin film array at intermediate wire diameter sizes may be suitable for optical phase shifting, intensity modulation and switching applications in integrated optical devices.

CHAPTER 1

Introduction

Within the past few decades, an enormous activity has been witnessed in studying the growth and structural, electrical, and optical properties of low-dimensional semiconductor structures such as quantum wells, quantum wires and quantum dots. Various advanced techniques to grow these structures have been developed over the period. More research is being done in growing these structures using different type of materials and fabrication techniques to obtain an extremely uniform distribution of nano-wires and dots, and with an excellent dimensional precision. The electronic and optical properties of the materials are altered due to the increase in confinement, as we proceed towards lower dimensional structures from quantum wells, to wires and dots. In general, the quantum confined structures exhibit a rich variety of enhanced optical properties as compared to their higher dimensional counterparts. The development of new fabrication techniques, the continuous improvements in the existing ones, the possibility of emergence of new physical phenomenon and their potential use in designing various novel and more efficient electronic as well as opto-electronic devices constitute some of the most important motivations behind the strong ongoing research in the area of low dimensional semiconductor structures. In this work, quantum wires or *1-Dimesnional*

semiconductor material systems are of special interest to us.

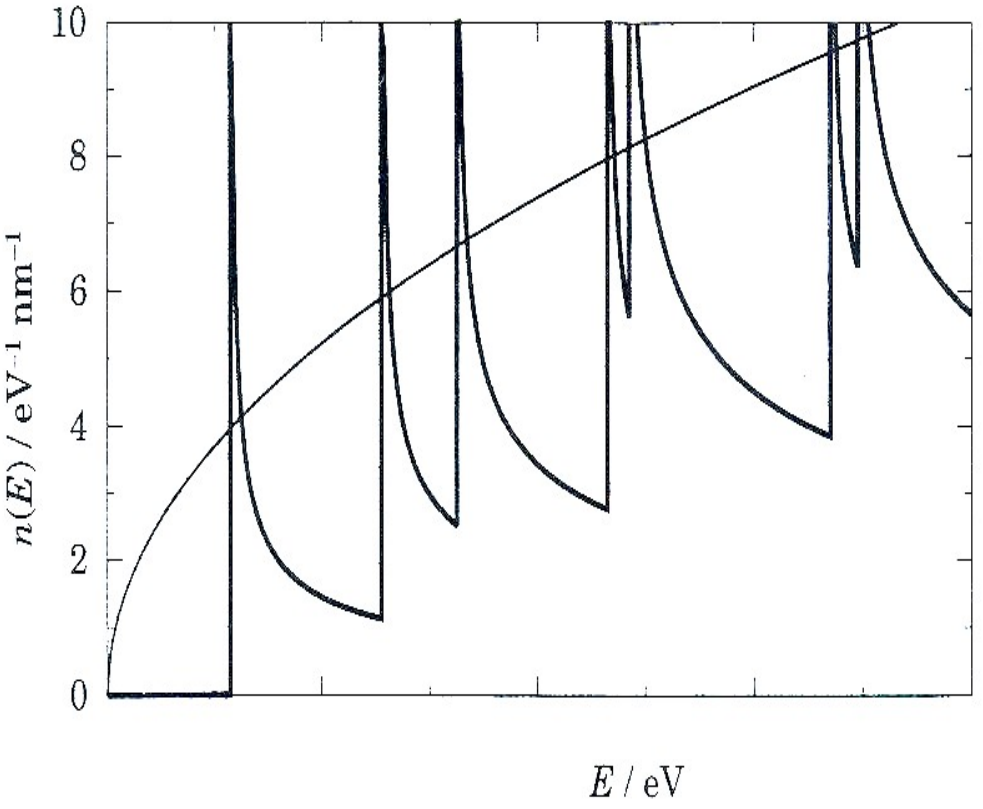

Fig. 1.1 Density of states function of a 1-Dimensional system

Fig. 1.1 shows the density of states functions in bulk and *1-Dimensional* system. Its behavior in a *1-Dimensional* system is a very peculiar one. It diverges at the bottom of each sub-band, and then decreases as the kinetic energy increases. This behavior of the density of states curve is very remarkable as it leads to a whole new set of optical and electrical effects peculiar to quantum wires.

The quantum wires find numerous applications in a wide variety of fields. Since the first suggestions by Sakaki [2] and the experimental realization by Petroff et. al. [3], *1-Dimesional* semiconductor structures have seen a tremendous amount of research. They have already emerged as the versatile nano-scale building blocks of the assembly of photonic devices [4]-[7], including polarization sensitive detectors [5], light emitting diodes [6], and electrical injection lasers [7]. Progress in the fields of such nano-photonic devices requires detailed understanding of how confinement of charge carriers and photons affects optical properties and gives rise to interesting optical phenomenon [7]-[9]. For example, single nano-wires have been recently shown to function as optical waveguides and Fabry-Perot cavities [7]-[10]. Intense optical excitation of a single nano-wire has produced stimulated emission and lasing [7],[11]-[12]. Lasing has also been obtained from quantum wire electrical injection devices. There are also efforts to develop Quantum Wire Tunable *THz* Phonon Detectors [13]. The development of *ZnO* nano-wire based white *LED*s has also been reported to perform stable operation at ambient conditions for long hours [14].

There is also a significant increase in the interest shown by the research community in self-assembled semiconductor nanostructures, which are fabricated by electro-deposition of semiconductor materials in porous alumina films [15]-[24]. These anodic alumina films are fabricated to produce a uniform distribution of arrays of nano-pores, which can be utilized for self-assembly of the semiconductor wires (or dots) of fairly uniform cross-section. The increasing attention towards porous alumina is due to its relatively easy and

low cost processing. Moreover, the anodic alumina films possess an extremely regular and highly anisotropic porous structures, with pore diameters varying from *5-200nm*.

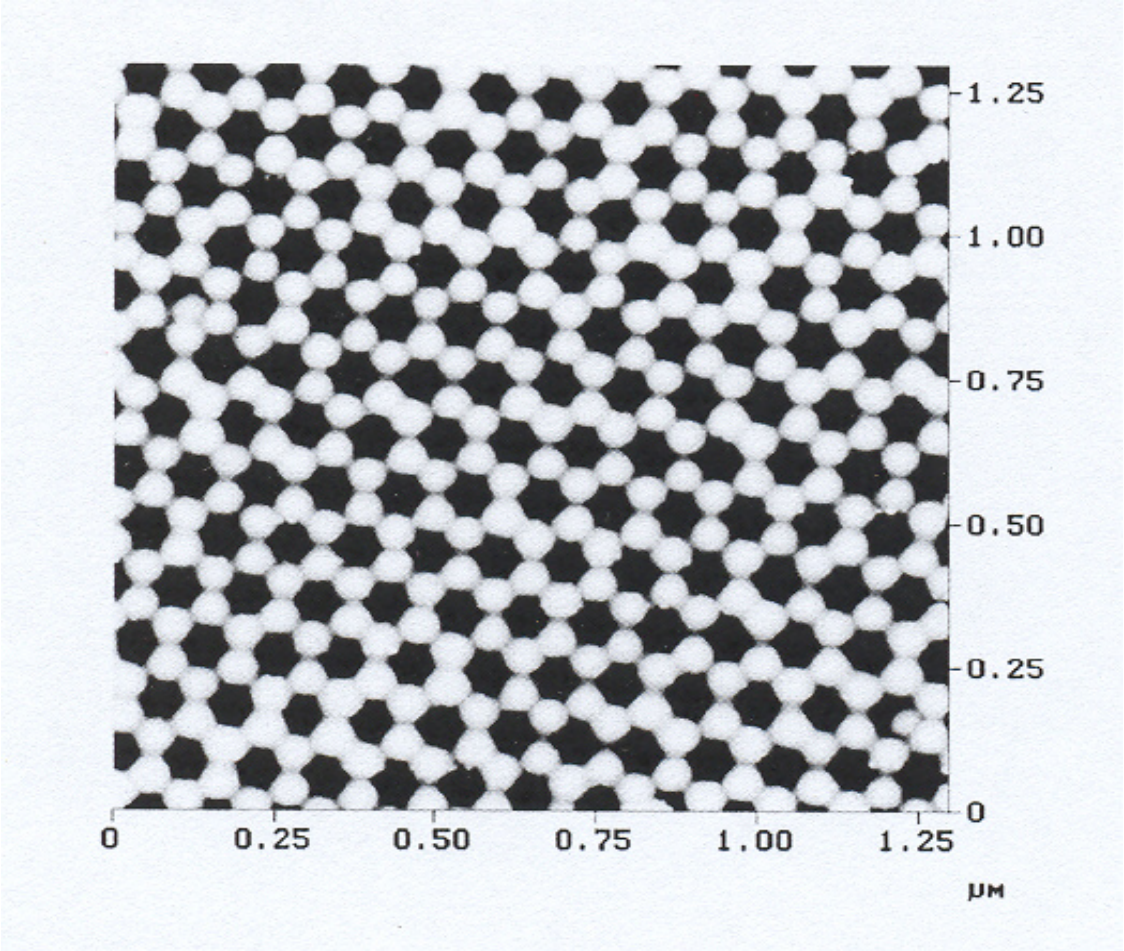

Fig 1.2 Raw atomic force micrograph of a porous alumina film [21]

These pores are uniformly distributed, formed in the direction of growth, and hence are very well suited for growing well aligned arrays of quantum wires and dots. Such structures possess very interesting magnetic, electronic, as well as linear and non-linear optical properties. A giant photo-resistivity in electrochemically self-assembled *CdS* and

ZnSe quantum wires has been reported, that finds applications in the "Normally-ON" infrared detectors [21]. These structures also hold promise in single electronic applications. They also have tremendous prospects in building nano-scale solid-state gate and logic devices suitable for miniaturization, self-assembled neural networks, etc. [22]. Just to name a few more, the applications of these structures also exist in the field of solar cells[25], carbon nano-tubes [26] and magnetic storage [27].

We have focused our research towards investigating the optical properties of quantum wires deposited in these electrochemically self-assembled porous alumina templates. Great interest has been showed by the scientific community in studying the wide band-gap, highly ionic semiconductors such as *ZnO, CdS, GaN, ZnSe, CdSe* for their potential applications in optoelectronic devices in the *blue* and *UV* regions of the electromagnetic spectrum. We have chosen four of these exciting materials for our investigations, namely *CdS, ZnSe, ZnO and CdSe* to be deposited in the porous alumina. All of them belong to *III-V* semiconductor compound system.

CdS has wide fundamental band-gap of *2.5 eV* at *300* ^{0}K. As it is very effective in *visible-UV* spectral region, *CdS* is extensively used in photo-conducting cells [28]. It is also widely used in manufacturing non-linear optical devices [29], heterogeneous solar cells [30], and a lot of other opto-electronic devices in the *visible-UV* range.

ZnSe has played an important role in the development of the blue-green lasers or blue injection lasers [31]. Its large band-gap (*2.69 eV*) and closely lattice matched nature make it more attractive to be used as a passivation layer for *GaAs* and as an insulating layer of

GaAs Field-Effect-Transistors [32]. It is also widely used in various non-linear optical devices [33].

ZnO has a band-gap of *3.35 eV* at *300 ^0K*. Like *CdS*, as it is very effective in the *visible-UV* spectral region, *ZnO* is used as a photo-conducting and fluorescent material. The excellent optical, piezoelectric, and acousto-optic properties of a thin film *ZnO* make it suitable in the fabrication of cell windows [34], gas sensors [35], surface acoustic wave devices [36] and integrated acousto-optic devices [37]. *ZnO* platelets have also been reported for optically pumped lasing at very low pump power [38].

CdSe has a comparatively smaller band-gap of *1.74 eV* at *300 ^0K*. It finds applications in the field of photovoltaic cells, photo-conductive materials, thin-film transistors, as well as optical data recording [39].

Our work is directed towards studying the electrochemically self-assembled quantum wire array structures, fabricated by electro-depositing the above-mentioned wide band-gap materials into porous alumina templates. All the research oriented towards improving the fabrication techniques for growing these nanostructures and thoroughly understanding the underlying physics involved would only improve the quality as well as performance of the devices in which these nanostructure are put into use. The ongoing research and developments in the field of porous alumina have gained pace, on account of its uniform distribution of nano-pores, and an easy, cost effective fabrication process. Their uniformity is especially useful in various optoelectronic devices. Investigation of certain optical behavior of the electrochemically self-assembled quantum wire arrays deposited in porous alumina, with the variations in diameters of the quantum wires, their material

compositions and the *UV* optical excitations, forms the core of this dissertation. We have developed a theoretical model to explain the effect of a stationary *UV* excitation on the optical behavior of this quantum wire array. This theoretical model could be used to calculate optical susceptibility, refractive index and absorption coefficient of the quantum wires under stationary excitation. The model is then incorporated into a finite-element electromagnetic wave simulator to examine the effects of *UV* excitation on the quantum wire array behavior, with the derived theoretical models in effect. We have also performed an experimental analysis using a pump-probe excitation scheme to measure the optical response of this quantum wire array in an optical homodyne setup using a Michelson interferometer.

In this dissertation, we study the effect of stationary *UV* excitation on the optical behavior of the electrochemically self-assembled semiconductor quantum wire array. The quantum wire array is formed, by filling the pores of the porous alumina substrate with the semiconductor material under investigation. For our experiments, we have used four different types of wide band-gap materials, namely, *CdS, ZnSe, ZnO* and *CdSe*. This dissertation work is divided into three major components.

a) Theoretical modeling,

b) Electromagnetic wave simulations, and

c) Experimental analysis.

In the theoretical treatment, we have derived a model to investigate the variations of the optical parameters of cylindrical quantum wires when excited by stationary UV radiation. We have followed a step-by-step approach to reach the final models that we incorporate

in the numerical field simulations. Initially, we disregard the Coulomb interactions between the carriers generated due to optical excitations. Accordingly, electrons and holes are treated as quasi free particles. In this section of our treatment, we also address the transition selection rules, calculate the optical dipole matrix element and discuss the inter-band kinetic equations for the free carriers in a two band approximation. Later, many body Coulomb effects in a low or virtual zero excitation regime are considered. Finally, we extend our treatment to include the optically excited semiconductor quantum wires. As we have used stationary *UV* excitation during our experiments, a quasi equilibrium is assumed to have been reached in the system, meaning the carriers are at thermal equilibrium among themselves within their bands. The total crystal however remains out of thermodynamic equilibrium. The theoretical models are then implemented using mathematical software, Mathematica, to calculate various important optical parameters, like dielectric constant ε (or permittivity) of the wire, its susceptibility, refractive index n, absorption coefficient α, etc.

In the electromagnetic wave simulations, we create a geometric model of the electrochemically self-assembled quantum wire array, assign typical material parameters to the quantum wires depending on what kind of material is used to fabricate the wires and incorporate derived theoretical models into this simulator. Basically, we re-create the same optical pump-probe experiment that is performed on the optical table, but in a simulation environment. We have used Ansoft Corporation's simulation software called *HFSS* (High Frequency Structure Simulator) for the quantum wire array analysis. Instead of using the whole quantum wire array structure, we have divided it into hexagonal unit

cells. The unit cell is repeated using a Master-Slave boundary condition, over the period of $10\times10\ \mu m^2$ to give the effect of an array structure. Master-Slave boundary conditions enable us to model the planes of periodicity such that the electric field of one surface matches the electric field on another to within a phase difference. A single unit cell consists of a cylindrical wire of the semiconductor material embedded in hexagonal alumina. The wire lengths are set at $1\ \mu m$, while simulations are performed for wire diameters that match our experimental samples, e.g. *50, 25 and 10nm*. We have also used an absorbing radiation boundary in which the model surface is electrically open, and the waves can radiate out of the structure and toward this type of boundary. The energy enters and exits the system via the ends of the hexagonal unit cells using a wave port type of excitation. This type of excitation is analogous to the practical situation where the light is incident on the device under test via an infinitely long waveguide. Using an adaptive meshing criterion, the mesh has been tuned to generate a very accurate and efficient mesh in the structure. Finally, a proper solution frequency point is chosen, which corresponds to our experimental value of *1308 nm*, to compute the electrical performance of the device. Using a driven mode type of modal solution set, the *S-parameters* are generated to obtain the phase variations of the wave due to the array structure.

We perform the experimental analysis of the quantum wire array using a pump-probe excitation scheme where we use a Michelson interferometer as a homodyne setup. The interferometer is constructed using *IR* laser probe, to which the quantum wire array sample is completely transparent. The sample is pumped using *UV* pulses. This *UV* excitation induces changes in the absorption coefficient and refractive index of the test

sample, which is continuously probed by the *IR* probe beam. The quantum wire material as well as alumina is completely transparent to the *IR* probe at *1308nm*. Hence, as the quantum wire array sample is placed in one of the beam paths of the Michelson interferometer probed by the *IR* laser, absolutely no change in power is observed at the output of the interferometer. But when the sample is pumped using *365nm UV* radiation of sufficient intensity, as the excitation photon energy is greater than the band-gap of the quantum wire material, a large number of electron-hole pairs are generated. This alters the optical behavior of the sample, including its refractive index and absorption coefficient. An interferometer is extremely sensitive to these changes. When the *UV* light is modulated at *1 KHz*, any *1 KHz* ac component at the output of the interferometer can be easily attributed to the effect of the *UV* excitation in the quantum wire sample. This *ac* component is then measured using a lock-in amplifier. Our calculations, which are explained in the later chapters, suggest that this *ac* component is an accurate measure of the phase changes in *IR* probe laser due the *UV* excitation behavioral changes of the quantum wire array. This component basically is the foundation of all our measurements. We have performed our experiments for four different types of semiconductor quantum wire arrays, namely *CdS, Znse, CdSe* and *ZnO*, each set with three different diameters, *50nm, 25nm* and *10nm*. The optical parametric changes at six different intensity levels of the *UV* pump excitation are measured over four different device sample batches.

Starting with the published values of the bulk dielectric constants of the materials under investigation, we calculate the theoretical permittivity values of the quantum wires using Mathematica. These values are then incorporated into the *HFSS* simulator. The phase

changes observed in all the sets are further matched with the experimental values to obtain the accurate optical parameters for the quantum wires under investigation.

This thesis is organized as follows. Chapter II describes some fundamental physics essential for understanding all the topics covered in our work. Chapter III describes the theoretical treatment for the development of various optical properties of quantum wires under stationary *UV* excitation. In Chapter IV, the theoretical models are incorporated into an electromagnetic wave simulator, HFSS, to study the optical behavior of the quantum wire array. Chapter V describes our experimental analysis of the data generated from the Michelson interferometer constructed as a homodyne setup and the pump-probe excitation scheme. The analysis and co-relation of all the studies performed in the previous chapters is provided in Chapter VI to demonstrate a good agreement in the theoretical and experimental data. Finally, the summary of all the dissertation work and conclusions are provided in Chapter VII.

CHAPTER 2

Fundamentals

2.1 Low Dimensional systems: *1-D* regime

Low-dimensional systems have revolutionized semiconductor physics. Low-dimensional semiconductors are the structures in which carriers behave as though they are free to move only in two or less dimensions. Most of these structures are actually hetero-structures, meaning they comprise more than one kind of material. Real electrons move in all three dimensions but they can be made to behave as though they are free to move only in fewer dimensions. Trapping them in a narrow potential well or a wire that restricts their motion in one, two or three dimensions at discrete energy levels can achieve this. If the separation between these energy levels of the adjoining materials is large enough, the electrons appear to be frozen into the ground state and no motion is possible in this constrained dimension.

Generally, the dimensionality in the single electron states is determined by the length of an electron wave function λ_e (Debroglie wave function) in semiconductors and insulators, while in metals, the length is in reference to the Fermi wavelength λ_f. When the geometrical confinement length of the system is comparable to λ_e or λ_f, the electron motion in that direction is physically constrained and the system dimensionality reduces

by one. In these conditions, the energy of the carriers is descretized, which is in contrast with the near continuum of the energy states for unconfined carriers, as in case of bulk materials. The major effect of reduced dimensionality on the electronic and optical behavior of the material arises from behavior of density of states function in low dimensional system.

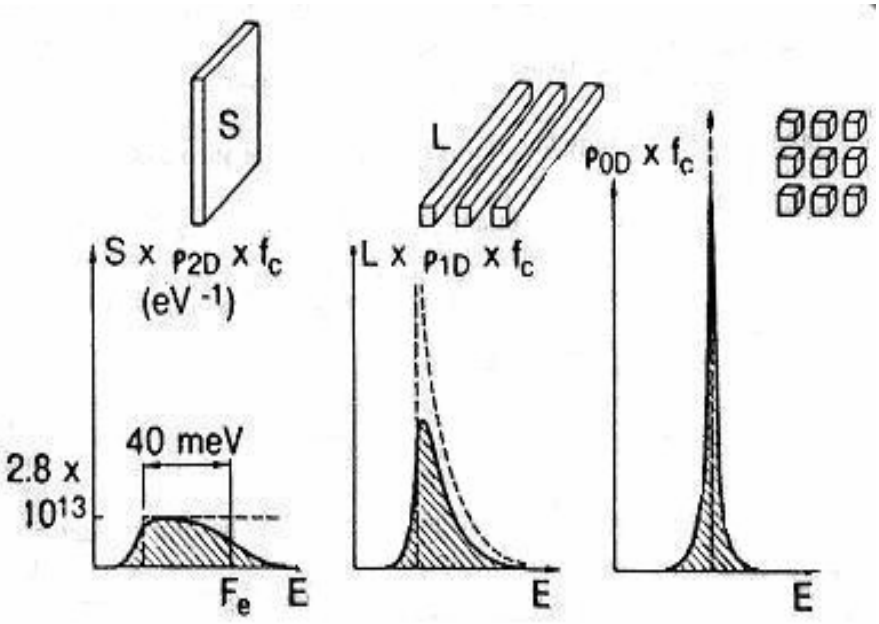

Figure 2.1 The statistical distribution of density of states for *2-D, 1-D* and *0-D* semiconductor structure plots as a function of energy [1]

Fig. 2.1 shows that with reduction in the dimensionality, the density of states gets more confined in the energy spectrum and increases sharply around certain energy values.

If we have to consider the simplest quantum wire geometry, the rectangular cross sectional wires surrounded by infinite barriers would be to the first you would think of, as

shown in Fig. 2.2. In this structure, while the electron movement is restricted in *x*-*y* direction due to the confinement potential, they are free to move only in *z*-direction. It is closely analogous to an electromagnetic wave guide.

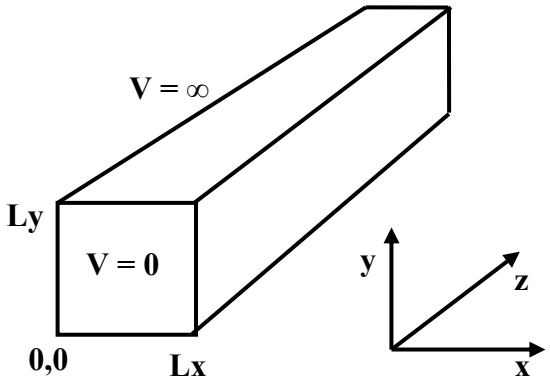

Fig. 2.2 The infinitely deep rectangular cross section of quantum wire.

Within the quantum wire, the potential is zero, while it is infinite outside the wire. Hence, the *2-D* Schrödinger equation in the confined *x*-*y* direction is written as

$$-\frac{\hbar^2}{2m^*}\left(\frac{\partial^2\psi_{m,n}(x,y)}{\partial x^2}+\frac{\partial^2\psi_{m,n}(x,y)}{\partial y^2}\right)=\varepsilon_{m,n}\psi_{m,n}(x,y) \tag{2.1}$$

The total wave-function and the energy would be given as

$$\psi_{m,n,k_z}(x,y,z)=\psi_{m,n}(x,y)Exp(ik_z z) \tag{2.2}$$

$$E_{m,n}(k_z)=\varepsilon_{m,n}+\frac{\hbar^2 k_z^2}{2m^*}=\frac{\hbar^2\pi^2}{2m^*}\left(\frac{m^2}{L_x}+\frac{n^2}{L_y}\right)+\frac{\hbar^2 k_z^2}{2m^*} \tag{2.3}$$

Each value of $\varepsilon_{m,n}$ described by the two principle quantum numbers *m* and *n*, is the total energy due to confinement, and becomes the bottom of *1-dimensional* sub-band. It could be observed that, if L_x is considerably larger than L_y, the *m* levels form a ladder of small steps within the sub-band ladder of well separated *n* levels. However, for $L_x \approx L_y$, the two ladders cannot be clearly separated and many energy levels are degenerate.

The one dimensional density of states function is shown in Eqn.2.4 .

$$n(E) = \frac{L_z}{\pi}\sqrt{\frac{2m^*}{\hbar^2}}\frac{1}{\sqrt{E-\varepsilon_{m,n}}}\Theta\left(E-\varepsilon_{m,n}\right) \tag{2.4}$$

where L_z is the length of the quantum wire.

This density of states function *n(E)* in *1-D* system, also shown in Fig.1.1, is very peculiar on account of its sharp peaks. The behavior of the density of states curve is very remarkable as it leads to a whole new set of optical and electrical effects peculiar to quantum wires.

2.2 Overview of the typical optical parameters

Classically, in a dielectric medium, electrons are assumed to be bound by certain harmonic forces to the positively charged ions. If this medium is excited by a periodic transverse electric field of the light beam, the electrical polarization is induced due to the microscopic displacement of these bound charges. This electric polarization is the macroscopic sum of the dipole moments induced in the crystal by the external field. When an electric field is applied across a crystal, it causes a displacement "*x*" of an

electron with charge "*-e"* from its equilibrium position producing a dipole moment. Accordingly, polarization, which is the dipole moment per unit volume, can be written as

$$P = n_0 ex$$

where "$d = ex$" is the dipole moment and "n_0" is the mean electron density per unit volume. The relation between the polarization P and electric field E describes the nature of the dielectric medium in the linear regime. Accordingly, P can also be defined as

$$P = \varepsilon_0 \chi E$$

where χ is a scalar constant called as electric susceptibility while ε_0 is the permittivity of free space. The electric flux density D is related to polarization P and electric field E as

$$D = \varepsilon_0 E + P$$

Hence from the above equations, electric flux density D can be rewritten as

$$D = \varepsilon E$$

where

$$\varepsilon = \varepsilon_0 (1 + \chi)$$

is a constant called as dielectric permittivity of the medium. The dielectric materials that absorb light have complex susceptibility (i.e. $\chi = \chi' + j\,\chi''$) and hence complex permittivity (i.e. $\varepsilon = \varepsilon' + j\,\varepsilon''$).

The ratio ($\varepsilon / \varepsilon_0$) is called the relative permittivity or dielectric constant of the medium. *In the discussion from here onwards, we would refer the term ε as the relative permittivity or dielectric constant of the medium, rather than assuming it to be an absolute value of the permittivity function. Hence from here onwards, the complex (relative) permittivity*

function is given as $\varepsilon(\omega) = \varepsilon'(\omega) + j\,\varepsilon''(\omega)$ which can describe the optical properties of the medium at all photon energies $E = \hbar\omega$.

From the causality and principle of superposition as applied to a linear medium, the Kramers-Kronig relations linking ε' and ε'' can be derived.

$$\varepsilon'(\omega) = 1 + \frac{2}{\pi}\int_0^{\infty} \frac{\omega_1 \varepsilon''(\omega_1)}{\omega_1^2 - \omega^2}\partial\omega_1 \tag{2.5-A}$$

$$\varepsilon''(\omega) = -\frac{2\omega}{\pi}\int_0^{\infty} \frac{\varepsilon'(\omega_1)}{\omega_1^2 - \omega^2}\partial\omega_1 \tag{2.5-B}$$

Kramers-Kronig relationship allows us to calculate the real part of a (permittivity) function, if the imaginary part is known, and vice versa. This relationship is of fundamental importance.

The complex refractive index $n^*(E)$ can then be written as

$$\begin{aligned} n^*(\omega) &= n(\omega) + j\kappa(\omega) \\ &= \sqrt{\varepsilon'(\omega) + j\varepsilon''(\omega)} \end{aligned} \tag{2.6}$$

where $n(E)$ is called as the ordinary or real refractive index, while $\kappa(E)$ is called the extinction coefficient or the attenuation constant. $n(E)$ and $\kappa(E)$ are both real and positive numbers. A finite value of extinction coefficient κ demonstrates the dielectric losses in the material.

Using equation (2.6), we can write

$$\varepsilon' = n^2 - \kappa^2 \tag{2.7-A}$$

$$\varepsilon'' = 2n\kappa \tag{2.7-B}$$

The absorption coefficient "*α"* determines the decay of intensity of the wave in the medium. The intensity decreases by a factor of *1/e* over the length "*α"*. The absorption coefficient (written in units *1/m*) can also be expressed as the number of photons absorbed per unit distance.

Wave-number *k* is the rate at which the phase of the wave changes due to the medium in the direction of propagation, hence rightly called as propagation constant. In the medium with effective refractive index *n*, the propagation constant "*k"* would simply be expressed as "nk_0" where k_0 is the vacuum wave-number

Using equation (2.6) and (2.7), we can easily calculate the absorption coefficient "*α"* and ordinary refractive index *"n",* as well as extinction coefficient *κ* in terms of the real and imaginary part of the (relative) dielectric functions. They are given as

$$n(\omega) = \sqrt{\frac{\sqrt{\varepsilon'^2(\omega) + \varepsilon''^2(\omega)} + \varepsilon'(\omega)}{2}} \tag{2.8}$$

$$\kappa(\omega) = \sqrt{\frac{\sqrt{\varepsilon'^2(\omega) + \varepsilon''^2(\omega)} - \varepsilon'(\omega)}{2}} \tag{2.9}$$

$$\alpha(\omega) = \frac{4\pi}{\lambda}\kappa(\omega) \tag{2.10}$$

Absorption coefficient *α* can also be written in terms of ordinary refractive index and imaginary part of the dielectric function as [40]

$$\alpha(\omega) = \frac{\omega}{n(\omega)c}\varepsilon''(\omega) \tag{2.11}$$

One of the important relevant discussions about the optical properties of semiconductors is the absorption of photons. Some of the photo-transitions that contribute to the overall absorption in a wide spectral region from far infrared up to ultraviolet spectra are briefly described below [41].

1. *Inter-band Photo-transitions (Band-to-Band)* : When an absorption of a photon causes the creation of electron-hole pair, it is called a Band-to-Band transition.

2. *Impurity to Band Transition* : In doped semiconductors, an absorbed photon causes a transition between bound state of an impurity and the conduction or valence band.

3. *Free Carrier Transition (Intra-band)* : An absorbed photon can transfer its energy to an electron or a hole, thereby increasing its energy within the same band.

4. *Excitonic Transitions* : The absorption of a photon can lead to the formation of an electron and a hole in coupled states which are called excitons.

5. *Phonon Transitions* : Long wavelength photons can be absorbed in the excitation of lattice vibrations, i.e. the process of creating phonons.

Although, impurity to band, phonon and free carrier type of transitions are also important, in the electrochemically self-assembled quantum wires that we use in our experiments, their effects remain negligible and/or irrelevant in the type of studies that we perform. For our topic, inter-band and excitonic types of transitions are the more important phenomena.

2.3 Excitons

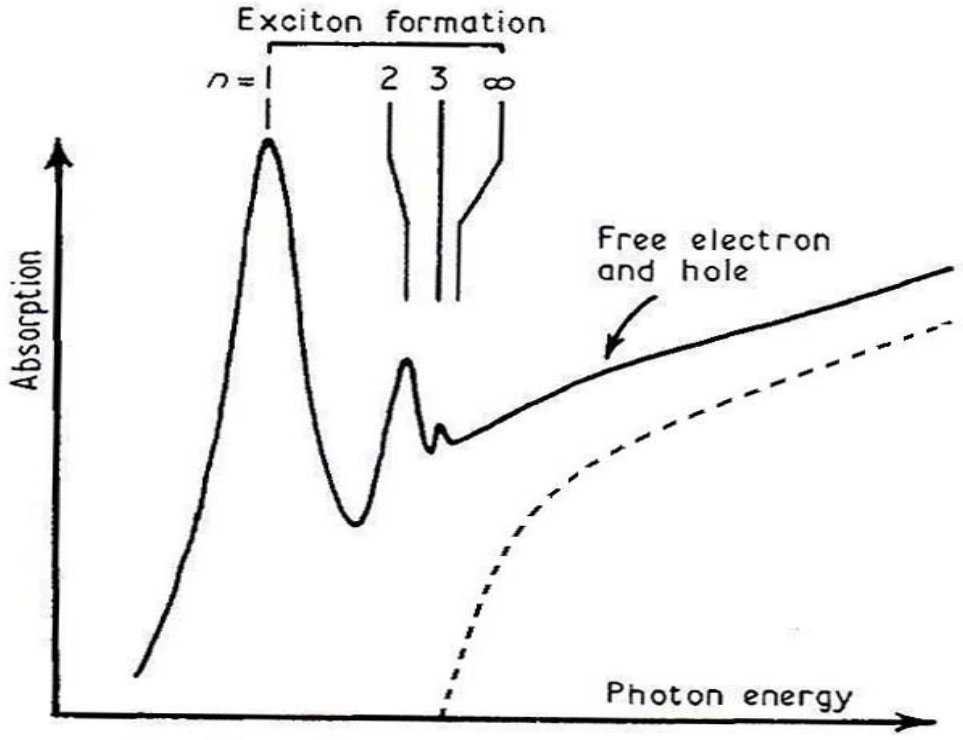

Fig 2.3 Optical spectra of a semiconductor near fundamental edge

An exciton is a quantum of an excitation energy traveling in the periodic structure of a crystal. It is electrically neutral and hence its movement through the crystal gives rise to the transportation of energy, but no charge. When a negatively charged electron and a positive hole situated at a distance *r* apart in free space interact via an attractive force, the effect is considered as a Coulomb interaction. The magnitude of this Coulomb force between the two carriers is given as $e^2 / 4\pi\varepsilon_0 r^2$, where *e* is the carrier charge, while ε_0 is the permittivity or dielectric constant of free space. The electron-hole pair bound together

by this Coulomb force could be considered as a quasi particle called an exciton. Excitons, or these coupled pairs of electrons and holes, can propagate through the crystal as single particles.

A typical band structure of the semiconductor consists of a conduction band and a valence band separated by an energy band gap E_g. Photo transitions are possible between the bands only when the photon energy $\hbar w > \hbar w_g (=E_g)$, where w_g is the threshold frequency to the fundamental band edge. The absorption spectrum for a typical bulk semiconductor is shown in Fig. 2.3 as a dashed curve. The coulomb interaction between the electron and holes, in other words the excitonic effects, are completely disregarded in that absorption spectrum. But, when excitonic effects are taken into consideration, we can observe a series of narrow lines or peaks in the spectrum, even below the fundamental band edge. These effects are usually suppressed at room temperature, but very much pronounced at low temperatures. The behavior of the semiconductor under this situation is shown in Fig. 2.3 as a solid curve. The Corresponding *E-k* relations is shown in Fig. 2.4.

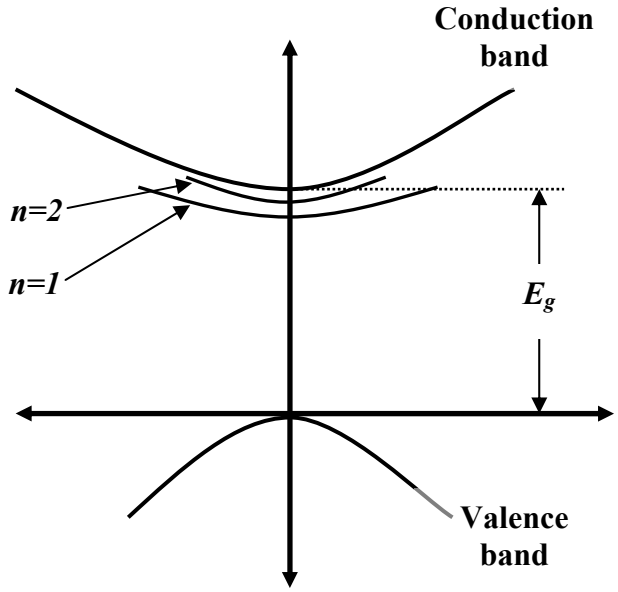

Fig. 2.4 *E-k* relation for Wannier excitons

Using the analogy between the exciton and a hydrogen atom, the bound state energies for this electron hole pair are given by the Rydberg formula

$$E = -\frac{e^2}{8\pi\varepsilon a_0 n^2} \tag{2.12}$$

where quantum numbers n takes the values $n=1,2,3,\ldots\ldots\infty,$ while a_0 is the exciton Bohr radius given as

$$a_0 = \frac{4\pi\varepsilon\hbar^2}{me^2} \tag{2.13}$$

Here, m is the effective reduced mass given as $m_e m_h/(m_e+m_h)$.

As we can observe from the above equations (2.12) and (2.13), the excitonic behavior is closely associated with the relative distance between an electron and a hole comprising that exciton. Accordingly, an exciton can exist in different quantum states, a ground state with lowest energy associated with it, as well as in number of higher excited states. The series of peaks shown in Fig. 1.3 are basically these quantization effects in the optical spectrum of a semiconductor below the fundamental band edge. The excitonic energies depend on various parameters like dielectric constant of the semiconductor material, the effective mass of electrons and holes in it, and so on. Accordingly, different materials would have different excitonic energies associated with them. We can also observe the changes in the semiconductor band spectrum even above the fundamental band edge, which are attributed to the non-coupled or free electrons and holes generated in the semiconductor. The exciton radius is directly proportional to the dielectric constant ε of the medium. Hence, materials with larger dielectric constants would have larger exciton radius. Moreover, since effective mass is directly proportional to the band-gap, as the band-gap of the material increase, it also increases its ground state exciton energy. The mass dependence of the exciton bound states is extremely important in our experimental analysis.

In case of *GaAs* with electrons and hole effective masses at $0.065m_0$ and $0.45m_0$ respectively, and its static dielectric constant at *13.42*, the exciton Bohr radius a_0 and ground state energy E_0 are calculated as *12.5 nm* and *4.6 meV* respectively. This demonstrates that in *GaAs* with lattice constant at *0.565 nm*, the exciton extends over quite a few atoms of the lattice, and its radius is comparable with the dimensions of a

typical nanostructure. It possesses the properties of a particle; it is mobile and able to move around the lattice.

All states of an electron-hole pair (or exciton) are excited states. As a matter of fact, a crystal said to be in the ground state corresponds to the valence band completely filled by electrons. Accordingly, there are no electrons in conduction band and no holes in valence band in a ground state of the crystal. Any state of the crystal with an electron in conduction band and a hole in valence band would be an excited state. In other words, an existence of an exciton represents the excited state. Therefore, just like an excited state, an exciton would also have a finite lifetime.

There are two limiting types of excitons :

1. *The Wannier excitons*
2. *The Frenkel excitons*

The *Frenkel* excitons are the strongly and tightly bound state of an electron-hole pair, while *Wannier* excitons are the weakly bound state of an electron-hole pair. The Bohr exciton radius a_0 of Wannier exciton is much larger than its lattice constant "*a"* as shown in Fig. 2.5. Almost all the excitons encountered in semiconductors and nanostructures are *Wannier* excitons. As the spatial extent of a *Wannier* exciton is much larger than a lattice constant, their wave-function is also affected by the spatial geometry of the material. The *Wannier* exciton has three degrees of freedom, a center of mass motion, an electron-hole relative motion, and a spin configuration. The latter two are internal degrees of freedom. The important fact that we are concerned about is the wave function of an

electron-hole relative motion which are sensitive to the geometry of the semiconductor structures, and determine its optical properties [42].

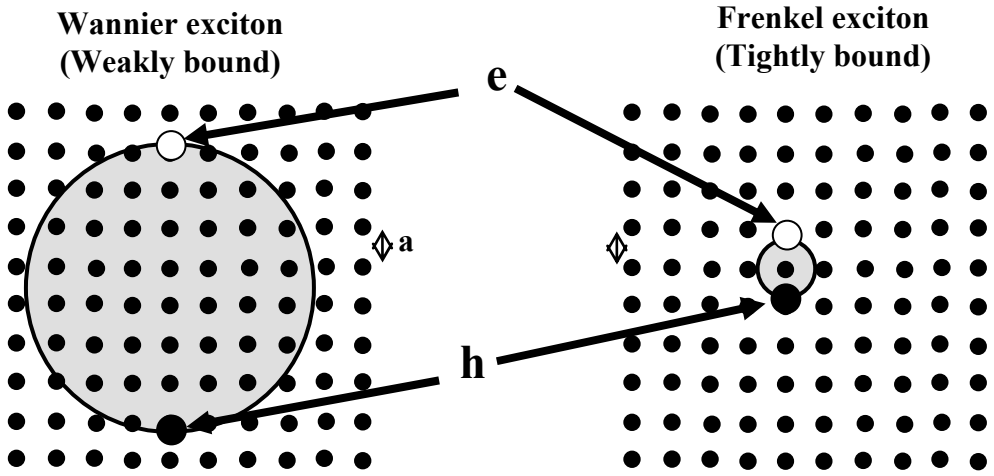

Fig. 2.5 *Wannier* and *Frenkel* type of excitons

One more important point about the excitons that is relevant in this work, is the dimensionality of the exciton system, which depends on the ratio of the exciton Bohr radius a_0 and the geometric confinement length L. In case, when $L<a_0$, the exciton becomes *quasi-1D* for *1-D* confinement. Roughly, for a quantum wire of radius R, quasi-1D excitons would exist, when $R<0.1a_0$.

2.4 Phenomenon of Interference

When we consider a region where two or more optical waves are present simultaneously, the total effect we observe would be due to the superposition of their individual wavefunctions. The total intensity of two waves with complex amplitudes A_1 and A_2 can be given as

$$I = |A|^2 = |A_1 + A_2|^2 = |A_1|^2 + |A_2|^2 + A_1^* A_2 + A_1 A_2^*$$

Consider two waves $A_1 = \sqrt{I_1} e^{j\varphi_1}$ and $A_2 = \sqrt{I_2} e^{j\varphi_2}$ traveling in the same direction with intensities I_1 and I_2 and phases φ_1 and φ_2. If we consider A as the superposition of the two waves at a point in space, then the intensity of the total wave would be

$$I = I_1 + I_2 + 2\sqrt{I_1 I_2} Cos(\Delta\varphi) \tag{2.14}$$

where Δφ is the phase difference between the two waves i.e. $\Delta\varphi = \varphi_2 - \varphi_1$.

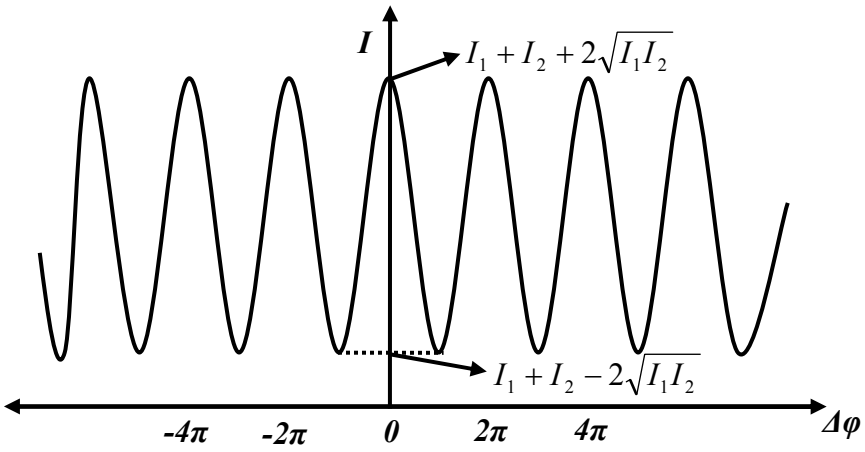

Fig 2.6 Superposition of two waves with phase difference Δφ

Equation 2.14 is generally called as an interference equation. Hence, the total intensity of the composite wave, as shown in Fig. 2.6, not only depends on the individual wave amplitudes (or intensities), but also depend on their phase difference. Hence, according to the interference equation, when two waves of equal amplitudes (or intensities) superimpose to form an interference pattern, the intensity of the observed interference fringes varies between certain minima and maxima, depending on the phase difference of the individual waves and their individual intensities.

If the waves are traveling in the same direction (say *z*), and one of the waves is lagging by a distance *d* with respect to other, then their phase difference would be *(2πd/λ)*. If the path difference is an integer multiple of the wavelength of light, constructive interference is observed. On the other hand, if it is an odd multiple of half the wavelength, a destructive interference occurs. Accordingly, for two waves of equal intensities traveling in the same direction, the interference equation could be written as [43]

$$I = 2I_0\left[1 + Cos\left(\frac{2\pi}{\lambda}d\right)\right]$$

where I_0 is the individual beam intensity.

The interferometer works on the principle of amplitude splitting. The incoming wave is split into two waves using a beam-splitter, travels unequal distances and gets reflected or re-directed by a set of mirrors. The waves then recombine via the same (or different) beam-splitter to form an interference pattern. Four important types of interferometers are the Michelson interferometer, the Mach-Zehnder interferometer, Sagnac interferometer and Fabry-Perot etalon. The first three are shown in Fig. 2.7.

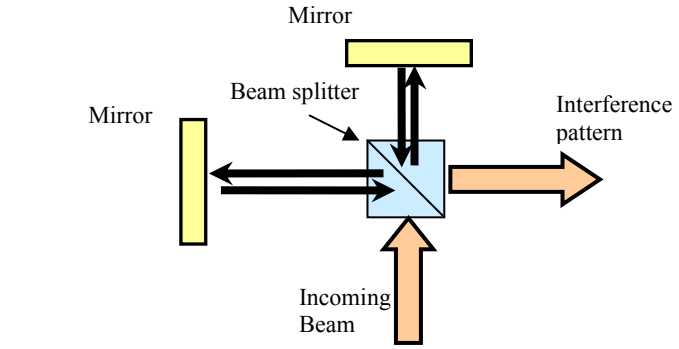

a) Michelson Interferometer

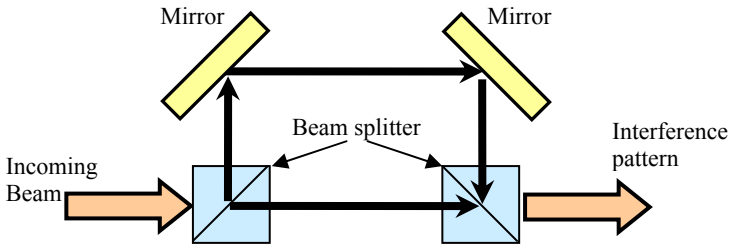

b) Mach-Zehnder interferometer

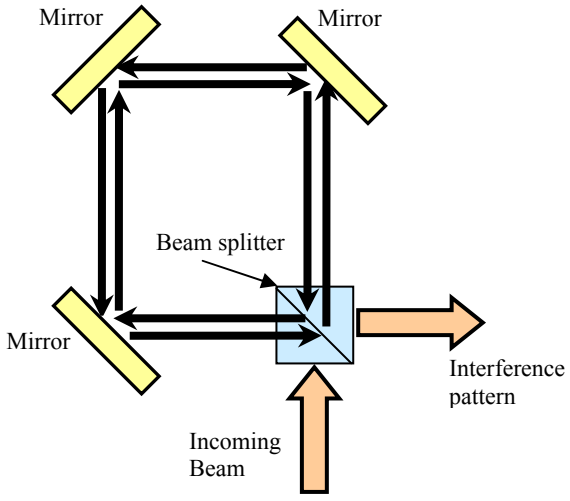

c) Sagnac Interferometer

Fig 2.7 Michelson, Mach-Zehnder and Sagnac interferometers. Waves travel via different paths and path lengths to form an interference pattern.

The Michelson interferometer, which we have used in our experiments, consists of a single beam-splitter, which divides the incoming beam into two beams of equal intensities. Both the beams are then reflected back along the same path by different mirrors, and recombined by the same beam splitter to form an interference pattern.

The electrochemically self-assembled quantum wire samples are then placed in one of the beam paths. If there is a small change in the optical behavior of the sample, it would be converted to a change in the interference pattern.

The intensity *I* is proportional to the phase difference between two waves, which could be rewritten as [43]

$$\Delta\varphi = \left(\frac{2\pi}{\lambda}\right)d = \left(\frac{2\pi}{\lambda_0}\right)nd \tag{2.15}$$

Accordingly, the interferometer can be used to indicate and measure variations of the distance *d*, refractive index *n*, or the wavelength λ_0 (or frequency) of the wave. We can see that for a monochromatic beam of wavelength $1.3\ \mu m$ and path length of $13\ cm$, a change $\Delta n = 10ppm$ in refractive index, would create a phase difference of a full 2π. Hence, extremely small changes in the optical behavior of the device under test could be identified and measured using an interferometer.

2.5 Fabrication of the electrochemically self-assembled semiconductor quantum wire array

The quantum wires that we have used in our experiments and theoretical investigations are fabricated using a simple electrochemical technique. In the process of quantum wire fabrication, a nano-porous alumina film is electrochemically self-assembled by anodizing the aluminum film. A two dimensional array of quantum wires are then formed by electro-depositing the material of interest within the pores of the porous alumina film.

As described in the last section, anodic alumina films with a uniform distribution of arrays of nano-pores are widely used for self-assembly of the semiconductor wires (or dots) of fairly uniform diameter. [22]-[24]. A relatively easy and low cost fabrication process of anodic alumina can produce very regular and highly anisotropic porous structures, with pore diameters varying from *5-200 nm*. The pore densities are in the range of $10^9 - 10^{12}$ /cm^2. These pores are uniformly distributed, formed in the direction of growth, and hence are very well suited for growing well aligned arrays of quantum wires and dots. But as the size of the pores is reduced, the pores might become more or less disordered, and this effect is attributed to certain constraints in the structural property of porous alumina [44].

The fabrication of nano-wires using the porous alumina method consist of three basic steps,

a) Electro-polishing,

b) Anodization, and

c) Electro-deposition.

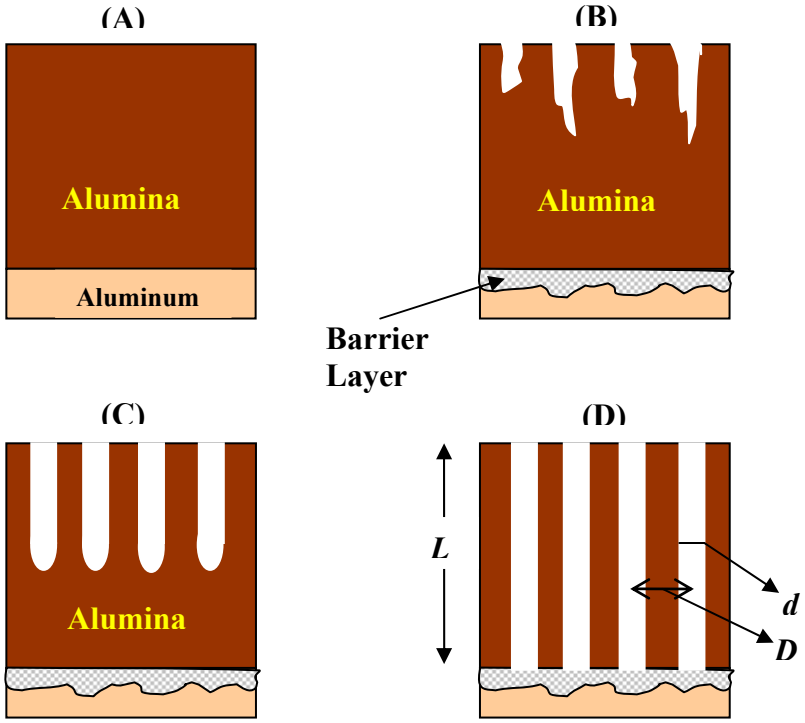

Fig. 2.8 Different stages in the fabrication process of porous Alumina. (A) Growth of Aluminum Oxide, (B) Fine featured pores being developed, (C) Enhanced pore growth, (D) Ultimate pore structure. *D* is the inter-pore separation, *d* denotes pore diameter, and *L* is the depth of the pores [45].

Electro-polishing of the aluminum foils is performed to reduce inherent surface roughness to about tens of nanometers and produce a clean, flat surface. Foils are then electrolyzed using a strong acid solution ($pH<4$) to obtain a porous alumina film on the surface. During this process of anodization, simultaneous deposition and dissolution of aluminum oxide takes place. Aluminum oxide is formed due to the exposure of aluminum foil to air. However, the dissolution of this Aluminum oxide due to the electrolysis in

presence of strong acid also takes place simultaneously. The effect of these two processes running together simultaneously results in the formation of porous alumina. The type and concentration of the acids used during this process, the amplitude of *DC* current passed through alumina as well as the anodization time determines the diameter *"d"* and depth *"L"* of the pores formed in the alumina template, as well as the inter-pore separation *"D"*[45] as shown in Fig. 2.8.

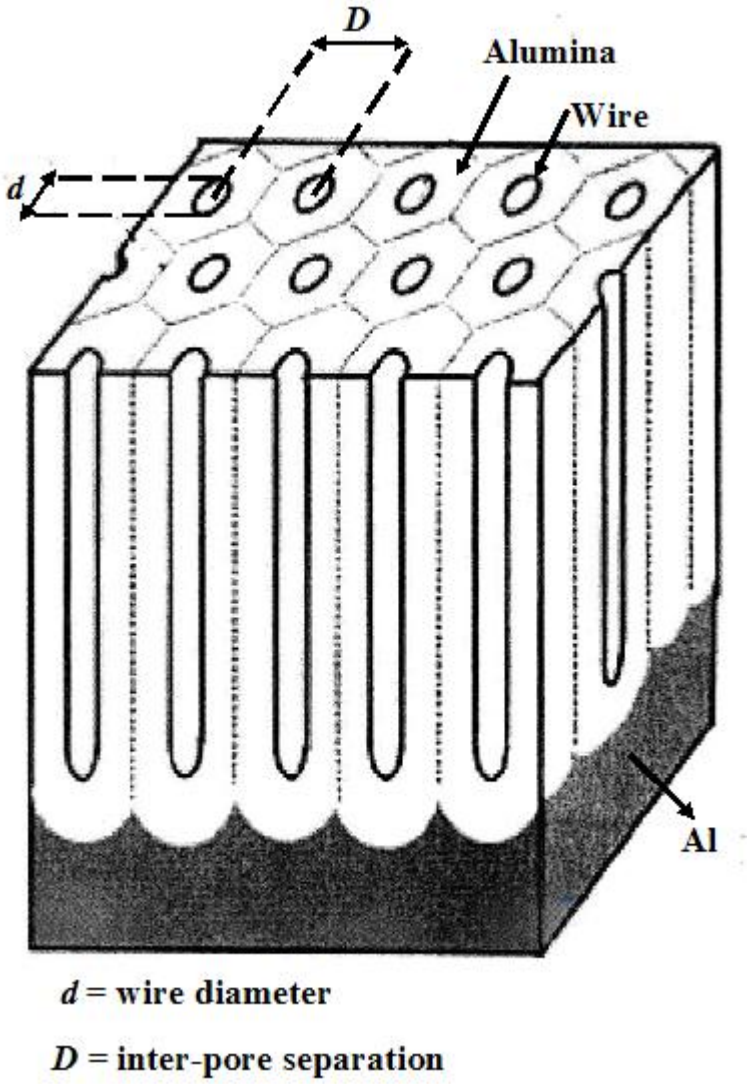

Fig. 2.9 Ideal structure of anodic porous aluminum oxide [46]

As the anodization voltage is turned ON, the anodization current is responsible for pore formation as well as barrier layer growth. After a *5-10* minutes of anodization process, the anodic film is removed using strong acids to obtain a porous alumina film along with the barrier layer at the interface of aluminum and pores. Uniformity of the pores is improved using a multi-step anodization process, rather than a single-step anodization [47]. The final porous alumina structure looks as shown in Fig. 2.9. A uniformly ordered array of pores formed in alumina is shown in Fig 2.10, which is the scanning electron micrograph of the porous alumina template [45].

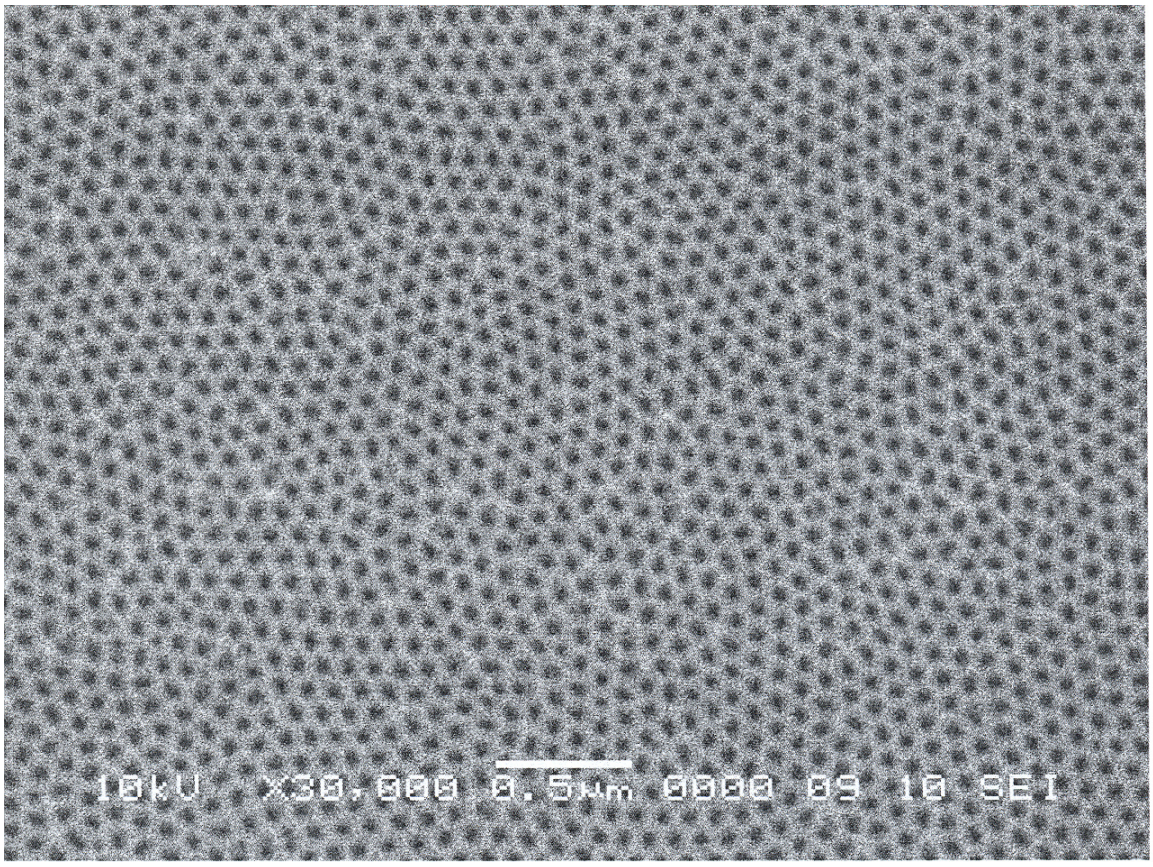

Fig. 2.10 SEM image of the porous alumina template

During the last step of electro-deposition, the pores are filled up with the materials of interest to form quantum wires or dots. The process could be either *AC* or *DC* type. The length of the wires depends on the type of electrolyte, its concentration as well as the electro-deposition time. In case of *DC* electro-deposition, barrier layer along with the aluminum at the bottom is chemically removed to create the alumina template with through pores. Wires formed using this process are easier to make an electrical contact with the external circuit and hence are potentially very useful in the fabrication of electrical and optical devices.

CHAPTER 3

Theoretical Modeling

Charge carriers can be generated in a semiconductor material by a number of ways, like doping, electronic injection or optical excitation. Intra-band transitions (transitions within the band) are primarily responsible for the electronic properties of the semiconductor material. On the other hand, inter-band transitions are connected with the optical properties of the material. However, a strict separation is completely impossible.

In this chapter, we primarily discuss the theoretical treatment to compute the optical properties of the quantum wires under stationary optical excitation. The purpose of this theoretical treatment is to study the optical changes in the quantum wires when they are excited by stationary *UV* light. In this chapter, we first describe the optical phenomenon at atomic level and explain the optical effects in free carrier system in quantum wires. Later, we include the Coulomb effects and study the optical phenomenon under low or virtually zero-excitation condition. Finally, the treatment is extended to include the effect of stationary or very long optical (*IR/UV*) excitation pulses on the optical properties of the quantum wires. The optical constants are solved as these theoretical equations are solved numerically using Mathematica.

3.1 Atomic Optical Susceptibility

Let's first consider some elementary treatment of the optical transitions of an atom.

For an atom with a single electron, the stationary Schrödinger equation is written as

$$H_0\psi_n(r) = \hbar\varepsilon_n\psi_n(r)$$

where $\psi_n(r)$ is the energy eigen-function while $\hbar\varepsilon_n$ are the corresponding eigen-values.

When the atom is excited with the optical field, it creates the dipole moment of the atom and hence introduces the time dependent changes of the wave-function. Hence,

$$i\hbar\frac{\partial\psi(r,t)}{\partial t}H_0 = [H_0 + H_1(t)]\psi(r,t)$$

Here $H_1(t)$ is the time-dependent perturbation due to an optical field i.e. dipole interaction with light.

$$H_1(t) = -exE(t) = -dE(t) \tag{3.1}$$

Here, the electric field is assumed to be polarized in x direction, and hence causes the displacement of an electron (cloud) in x direction from its equilibrium. Note that, in the above equation, d is the dipole operator.

The time-dependent solution for the above Schrödinger equation would be

$$\psi(r,t) = \sum_m a_m(t)\psi_m(r)e^{-i\delta_m t}$$

Inserting H_1 in time-dependent Schrödinger equation and then multiplying both sides by $\psi_n^*(t)$ we get,

$$i\hbar\sum_m\left[\left(\frac{\partial a_m(t)}{\partial t} - i\varepsilon_m a_m\right)e^{-\varepsilon_m t}\int\partial^3 r\psi_n^*\psi_m\right]$$
$$= \sum_m a_m(t)e^{-i\varepsilon_m t}\int\partial^3 r\psi_n^* H_o\psi_m - E(t)\int\partial^3 r\psi_n^* d\psi_m$$

This leads us to an equation to calculate coefficients a_n as

$$\frac{\partial a_n}{\partial t} = -E(t)\sum_m e^{-i\varepsilon_{mn}t}\langle n|d|m\rangle a_m$$

where

$$\varepsilon_{mn} = \varepsilon_m - \varepsilon_n$$

is the frequency difference or the transition frequency, and

$$\langle n|d|m\rangle = \int \partial^3 r \psi_n^* d\psi_m \equiv d_{nm} \tag{3.2}$$

is the dipole matrix element.

The value for a_n has been solved in Ref. [48] and [49] as

$$a_n(t) = -\frac{d_{nl}}{\hbar}\int \frac{\partial\omega}{2\pi} E(\omega)\frac{e^{-i(\omega+\varepsilon_{\ln})t}}{\omega+\varepsilon_{\ln}+i\gamma}$$

In the above calculations, the optical field has been used in its Fourier Transform expression as

$$E(t) = \lim_{q\to 0}\int \frac{\partial\omega}{2\pi} E(\omega)e^{-i\omega t}e^{qt} \tag{3.3}$$

In the above expression, q is the wave number of the optical field. It is also addressed as photon momentum and is calculated as $q = (2\pi / \lambda)$. In the dipole approximation, as wavelength $\lambda >> a_0$, the lattice constant of the crystal $q << k_c$, k_v, which is the momentum of the electron in initial and final state. The electron momentum is approximately given as $k = 2\pi/a_0$. Hence, the momentum of the photon, q can be

neglected in dipole approximation. This momentum q is used as an infinitesimal damping parameter such that, as $E(t) \rightarrow 0$ *as* $t \rightarrow \infty$.

If we consider only the linear response theory, i.e., only linear terms in the field are taken into account, the total wave function would be

$$\psi(r,t) = e^{-i\omega t}\left[\psi_l(r) - \sum_{m\neq l}\frac{d_{nl}}{\hbar}\psi_l(r)\int\frac{\partial\omega}{2\pi}E(\omega)\frac{e^{-i\omega t}}{\omega+\varepsilon_{lm}+i\gamma}\right] \qquad (3.4)$$
$$+ Higher - Order - Terms$$

As polarization is the macroscopic sum of the dipole moments induced by the field $E(t)$, it is also expressed as the expectation value of the dipole operator,

$$P(t) = n_0\int\partial^3 r\,\psi_n^*(r,t)d\psi_m(r,t)$$

where n_0 is the density of the non-interacting atoms in the system.

From the above two equations and considering only the lower order terms, polarization P is calculated as

$$P(t) = n_0\sum_m\frac{|d_{lm}|^2}{\hbar}\int\frac{\partial\omega}{2\pi}\left[E(\omega)\frac{e^{-i\omega t}}{\omega+\varepsilon_{lm}+i\gamma} + E^*(\omega)\frac{e^{i\omega t}}{\omega+\varepsilon_{lm}-i\gamma}\right]$$

As $E(t)$ is real, $E^*(-\omega) = E(\omega)$, and we can also substitute $\omega \rightarrow -\omega$. Hence the above expression simplifies to

$$P(t) = n_0\sum_m\frac{|d_{lm}|^2}{\hbar}\int\frac{\partial\omega}{2\pi}E(\omega)e^{-i\omega t}\left[\frac{1}{\omega+\varepsilon_{lm}+i\gamma} - \frac{1}{\omega-\varepsilon_{lm}+i\gamma}\right] \qquad (3.5)$$

But, as

$$P(t) = \int\frac{\partial\omega}{2\pi}P(\omega)e^{-i\omega t} \qquad (3.6)$$

and

$$P(\omega) = \chi(\omega)E(\omega) \tag{3.7}$$

the optical susceptibility χ for an atom is calculated as,

$$\chi(\omega) = \frac{n_0}{\hbar}\sum_m |d_{lm}|^2 \left[\frac{1}{\omega + \varepsilon_{lm} + i\gamma} - \frac{1}{\omega - \varepsilon_{lm} + i\gamma}\right] \tag{3.8}$$

According to Dirac's identity equation in Ref. [50]

$$\frac{1}{x \mp \Delta} = P\frac{1}{x} \pm i\pi\delta(x) \tag{3.9}$$

where, $\Delta \to 0$, P is the principle value of the integral under which this relation is used, while δ is the *Dirac's delta* function.

Also, as we are dealing with complex permittivity, i.e.,

$$\varepsilon = \varepsilon' + j\varepsilon'' = \varepsilon_0(1 + \chi' + j\chi'')$$

The imaginary part of the dielectric permittivity, using which we calculate absorption coefficient according to Eq. (2.11), is

$$\frac{4\pi^2 n_0}{\hbar}\sum |d_{nl}{}^2| \left[\delta(\omega - \varepsilon_{n,l}) - \delta(\omega - \varepsilon_{l,n})\right]$$

In the above equation, as $|l\rangle$ is the initial occupied state and $\langle n|$ is the final state, first δ-term represents light absorption. The optical transition takes place from the occupied lower state $|l\rangle$ to higher energy state $\langle n|$, if the photon energy $\hbar\omega$ is greater than the energy the difference $\hbar\varepsilon_{nl}$ between the two states, i.e.,

$$\hbar\omega > \hbar(\varepsilon_n - \varepsilon_l)$$

This energy difference between the states is referred as the band gap energy E_g. Hence, a photon with energy $\hbar\omega$ excites a valence band electron to a conduction band and creates a

hole in the valence band. Naturally, as these electrons and holes are respectively generated in conduction and valence band, they interact on account of the Coulomb potential and hence influence the optical properties of the crystal.

3.2 Free Carrier Transitions in a semiconductor crystal

Now let's move discussion from atoms towards a semiconductor crystal. As stated earlier, electron-hole pairs are generated in the semiconductor when excited by light of a photon energy $\hbar\omega$ greater than the semiconductor band-gap. These carriers have opposite charges and interact on account of their mutually attractive Coulomb potential. For the sake of simplicity and to understand the phenomenon to the basics, the Coulomb interactions between the photogenerated electrons and holes are not considered in this section and they are treated as (quasi) free particles.

3.2.1 Optical Dipole Matrix

Generally electrons in semiconductor are not in pure states, but in mixed states [51]. Pure states are described by the wave function, while the density matrix describes mixed states. Using general completeness relation,

$$\sum |\lambda, k\rangle\langle\lambda, k| = 1,$$

The Hamiltonian of the electrons in a crystal in the unperturbed state could be written as

$$H_0 = \sum_{\lambda,k} \varepsilon_{\lambda,k} |\lambda\rangle\langle\lambda|$$

where λ denotes the sub-band number and k is the wave vector. As described previously, the dipole interaction with the light is given as

$$H_1 = -erE(t)$$

where "*er = d"* is the projection of the dipole moment in the direction of the electromagnetic field. Using the completeness relation again, the dipole interaction H_1 can be expressed in the form

$$H_1 = -eE(t) \sum_{\lambda',\lambda,k',k} r_{\lambda',\lambda}(k',k) |\lambda' k'\rangle\langle\lambda k| \tag{3.10}$$

where

$$r_{\lambda',\lambda}(k,k') = \langle\lambda' k'|r|\lambda k\rangle$$
$$= \int \partial^3 r \psi^*_{\lambda'}(k') r \psi_\lambda(k)$$

Here $er_{\lambda'\lambda}(k',k)$ is the dipole matrix element. Let's limit our discussion here, purely to the inter-band transitions, i.e. $\lambda' \neq \lambda$. The above equation could be expressed in terms of the Poisson Bracket commutation relation [52] as

$$r_{\lambda',\lambda}(k',k) = \frac{1}{E_{\lambda'}(k') - E_\lambda(k)} \langle\lambda' k'|[r, H_0]|\lambda k\rangle$$

$$= \frac{1}{m_0(\varepsilon_{\lambda,k} - \varepsilon_{\lambda',k'})} \langle\lambda' k'|p|\lambda k\rangle \tag{3.11}$$

where p is a momentum operator.

Using *k.p* theory, the electronic wave function $\psi_\lambda(k,r)$ in the lattice can be written in terms of periodic Block function $U_\lambda(0,r)$, which is periodic in real space as,

$$\psi_{\lambda}(k,r) = e^{ik.r}\frac{U_{\lambda}(0,r)}{L^{3/2}} \tag{3.12}$$

The above integral could be considered as the sum of the unit cell integrals spread over the whole crystal, all of which yield the same result. Note that the wave function is assumed to be normalized for the volume L^3. Due to the periodicity of the lattice wave functions and their orthogonality, the optical dipole matrix element is calculated as

$$er_{\lambda',\lambda}(k',k) = \frac{ie}{m_0\left(\varepsilon_{\lambda,k} - \varepsilon_{\lambda',k'}\right)}\delta_{k,k'}p_{\lambda',\lambda}(0) \tag{3.13}$$

The δ function in the above equation indicates that dipole matrix element couples identical *k*-states in different bands (which is a selection rule for optical transitions) and the momentum is conserved. Hence, dipole approximation is equivalent to ignoring the photon momentum in comparison to a typical electron momentum in Brillion zone. Thus, the changes in wave vector $\vec{k}$ are neglected during photo-transitions and they are actually shown as vertical transitions in the *E-k* diagram. Vertical transitions are possible only in direct band gap materials, in which minimum of the conduction band and maximum of the valence band are situated at the same point of the $\vec{k}$ space.

The final expression for the optical dipole matrix element is written as

$$\begin{aligned} er_{\lambda',\lambda}(k',k) &= d_{\lambda',\lambda}(k',k) \\ &= \delta_{k',k}d_{\lambda',\lambda}(0)\frac{\varepsilon_{\lambda,0} - \varepsilon_{\lambda',0}}{\varepsilon_{\lambda,k} - \varepsilon_{\lambda',k'}} \end{aligned} \tag{3.14}$$

where

$$d_{\lambda',\lambda}(0) = \frac{iep_{\lambda',\lambda}(0)}{\varepsilon_{\lambda,k} - \varepsilon_{\lambda',k'}} \tag{3.15}$$

Except for the δ function, the *k* dependence of the dipole matrix element can often be neglected in the spectral region around the semiconductor band edge. The *k* -dependence is important only if the variation over the whole first Brillion zone is needed, as in Kramer-Kronig transitions or computations of refractive index.

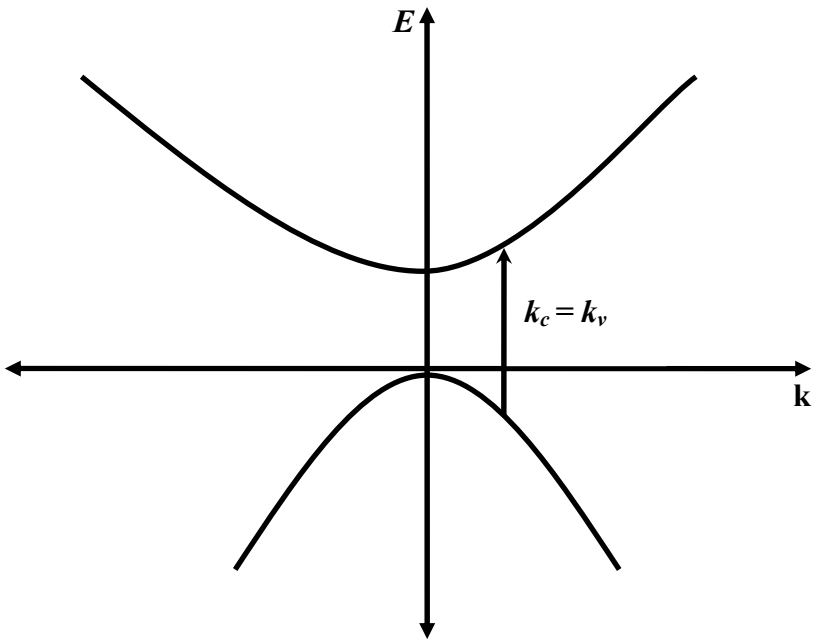

Fig. 3.1 *E-k* diagram (momentum conservation)

3.2.2 Optical Inter-band Transitions in a semiconductor crystal

Note that the calculations in this section are simplified by considering only the free carrier transitions, or in other words, neglecting the Coulomb interactions. The procedure could be more simplified by restricting our treatment to the conduction band *c* and valence band *v* only. Let's call this as a two-band-approximation model. This kind of two

band model is a reasonable first order approximation to calculate the optical response of a real material, if all other possible transitions are sufficiently detuned with regards to the frequency region of interest.

As discussed in the last section, Hamiltonian due to optical perturbations is given as

$$H_1 = -E(t)\sum_{\lambda'\neq\lambda,k} d_{\lambda',\lambda}\left|\lambda' k\right\rangle\left\langle \lambda k\right|$$

In the above equation, only those optical dipole matrix elements that couple identical k-states in conduction and valence band are considered. It also states that different k-states are not mixed if we ignore the Coulomb interactions between the carriers. Accordingly, two band approximation of the interaction Hamiltonian is

$$H_1 = -E(t)\left[d_{cv}\left|ck\right\rangle\left\langle vk\right| + d_{cv}^{*}\left|vk\right\rangle\left\langle ck\right|\right] \tag{3.16}$$

where $d_{cv}^{*} = d_{vc}$ is used.

The time development of the inter-band matrix element in the interaction representation has been calculated in Ref.[53], [54]. The time development of the off-diagonal elements of the density matrix is given as

$$\frac{\partial}{\partial t}\rho_{cv}^{\text{int}}(k,t) = \frac{i}{\hbar} d_{cv} E(t) e^{i(\varepsilon_{c,k}-\varepsilon_{v,k})t}\left[\rho_{vv}(k,t) - \rho_{cc}(k,t)\right] \tag{3.17}$$

Note that, the interaction representation [51] in equation(3.17) above, is used to express any time dependent quantity *x(t)* in terms of its initial value, as

$$x^{\text{int}}(t) = e^{\frac{i}{\hbar}H_0 t} x(0) e^{-\frac{i}{\hbar}H_0 t}$$

where H_0 is the time independent Hamiltonian. The above equation shows that the off diagonal elements ρ_{cv} of the density matrix for the momentum state k couple to the

diagonal elements ρ_{cc} and ρ_{vv} of the same k state. The coupling between the elements with different k-values would appear if the Coulomb interactions are taken into the account.

Also note here that,

$$x_{c,v} = \langle c | x | v \rangle$$

where $\langle c |$ and $| v \rangle$ are the bra-ket representations of the carrier eigen-function.

The diagonal elements of the density matrix $\rho_{\lambda\lambda}$ give the probability to find an electron in the state $| \lambda k \rangle$. In other words, ρ_{cc} is the population distribution of electrons in the conduction band. The time development of the diagonal elements of the density matrix is calculated in [53] as

$$\frac{\partial}{\partial t}\rho_{cc}^{\text{int}}(k,t) = \frac{i}{\hbar}E(t)\left[d_{cv}e^{i(\varepsilon_{c,k}-\varepsilon_{v,k})t}\rho_{vc}^{\text{int}}(k,t) - c.c.\right], \tag{3.18}$$

$$\frac{\partial}{\partial t}\rho_{vv}^{\text{int}}(k,t) = \frac{i}{\hbar}E(t)\left[d_{cv}^{*}e^{i(\varepsilon_{v,k}-\varepsilon_{c,k})t}\rho_{cv}^{\text{int}}(k,t) - c.c.\right],$$

$$= \frac{\partial}{\partial t}\rho_{cc}(k,t) \tag{3.19}$$

In the above equations, $\rho_{cv} = \rho_{vc}^{*}$ has been used. Also, $\rho_{\lambda\lambda}^{\text{int}} = \rho_{\lambda\lambda}$

The above time development equations (3.17)-(3.19) for the density matrix elements describe the inter-band kinetics of the free carrier system. Many body effects due to interaction between excited carriers haven't been incorporated in these equations yet.

Here we have to take into account, two limiting cases of the non interacting systems.

1. *Coherent Optical Inter-band Transitions* : These transitions are realized, at least approximately, in the experiments in which ultra-short pulses are used. Here, the carriers follow the laser field coherently, i.e. without significant de-phasing. Optical Stark effect, photon echo, the observation of quantum beats; ultra-fast adiabatic following are some of the examples of coherent optical processes.

2. *A quasi-equilibrium situation* : A quasi-equilibrium is typically reached when stationary excitation, or at least the excitation with optical pulses which are long in comparison to carrier scattering time, are used in the experiment. Under these conditions, the excited carriers have sufficient time to reach thermal equilibrium distribution within their bands. Note here that quasi-equilibrium means that the carriers are at thermal equilibrium among themselves within their bands, but the total crystal is out of thermodynamic equilibrium. In case of total equilibrium, there would be no carriers in the conduction band of the semiconductor.

Generally, carrier scattering times are of the order of sub-picoseconds in bulk semiconductors, that too at lower temperatures. Hence for our experiment, where we excite the nano-wire array with *UV* pulses longer than few microseconds, carrier scattering time is definitely shorter than the *UV* pulse periods. This type of excitation appears to be a stationary optical excitation, and hence *quasi-equilibrium* is assumed to have been reached in the system.

3.2.3 Quasi-Equilibrium regime in quantum wires

The dynamics of the distribution of electrons and holes within their bands, together with the treatment of all processes which generate or annihilate particles within one band, constitute the intra-band kinetics. To explore this, we derive and solve quantum Boltzman equations $f_{e,k}(r,t)$ and $f_{h,k}(r,t)$. For typical plasma densities, it has been shown in [55]-[57] that the relaxation times are of the order of sub-picoseconds. Femto-second hole burning experiments in [57] have shown that the relaxation time must be about *0.1* pico-second in an inverted laser diode. Within this short time period of the inter-band carrier relaxation time due to the inter-band scattering, the optically created electrons and holes establish a local quasi-equilibrium within their bands. For all the processes which take place on a time scale larger than this relaxation time, we can assume that the electron and hole distribution is already in a local *quasi-equilibrium*. The term *quasi* is used to distinguish the partial thermal equilibrium within one band from the total equilibrium of the unperturbed semiconductor with practically no *e-h* excitations.

The assumption of quasi thermal distribution of carriers (electrons in conduction band and holes in valence band) significantly simplifies the further calculations. As diagonal elements of the density matrix don't have to be calculated, (their being the population distribution of the carriers within their respective bands, given by the *Fermi* distribution), it provides a shortcut to the analysis of the optical response. The diagonal elements of the density matrix calculated according to the *Fermi* distribution would be

$$\rho_{\lambda\lambda}^{o} = \frac{1}{1+e^{\frac{E_{\lambda,k}-E_{F,\lambda}}{K_B T}}} = f_{\lambda,k} \tag{3.20}$$

where, chemical potential $E_{F\lambda}$ (or Fermi energy) is determined by the condition that the sum $\sum_k f_{\lambda,k}$ would yield the total number of carriers N_λ in the band λ. In the above expression, K_B is the Boltzman constant, while $1/K_BT$ is called the inverse thermal energy.

Under total equilibrium and when $K_BT << E_g$, the valence band is completely filled and the conduction band is completely empty i.e. $N_v = N$ and $N_c = 0$ where N is the number of atoms. Hence, we don't have to solve Eq. (3.18), (3.19) to calculate the diagonal elements of the density matrix. Now consider the first equation (3.17) for the off-diagonal elements of the density matrix. Using the optical field equation (3.3) in the form of its Fourier transform and the Fermi distribution equation (3.20) above, time development equation (3.17) for the off diagonal elements, when integrated over time t is rewritten as

$$\rho_{cv}^{\text{int}}(k,t) = \int \frac{\partial\omega}{2\pi} \frac{d_{cv} E(\omega) e^{-i(\varepsilon_{c,k} - \varepsilon_{v,k})t}}{\hbar(\varepsilon_{c,k} - \varepsilon_{v,k} - \omega - iq)} (f_{v,k} - f_{c,k})$$

Infinitesimal damping parameter q in the exponential in the above equation is deleted being a negligible term.

The density matrix formalism of the optical polarization (which essentially is the sum of the dipole moments over all diagonal elements) is written as

$$P(t) = trace\left[\rho^{\text{int}}(t) d^{\text{int}}(t)\right]$$

Hence,

$$P(t) = \frac{1}{L^3} \sum_k \int \frac{\partial\omega}{2\pi} \frac{|d_{cv}|^2 (f_{v,k} - f_{c,k})}{\hbar(\varepsilon_{c,k} - \varepsilon_{v,k} - \omega - iq)} E(\omega) e^{-i\omega t} + c.c$$

But we know that

$$P(\omega) = \chi(\omega)E(\omega)$$

and

$$P(t) = \int \frac{\partial\omega}{2\pi} P(\omega)e^{-i\omega t}$$

Hence, Optical Susceptibility χ as a function of frequency can be calculated as

$$\chi(\omega) = -\sum_k \int \frac{|d_{cv}|^2}{L^3}\left(f_{v,k} - f_{c,k}\right)\left[\frac{1}{\hbar(\varepsilon_{v,k} - \varepsilon_{c,k} + \omega + iq)} - \frac{1}{\hbar(\varepsilon_{c,k} - \varepsilon_{v,k} + \omega + iq)}\right] \qquad (3.21)$$

Above equation gives the free carrier optical susceptibility, as we haven't yet considered the Coulomb interactions in our treatment.

In the above equation, we can see that χ(ω) has the poles at $\omega = \pm\left(\varepsilon_{c,k} - \varepsilon_{v,k}\right) - iq$, which are the resonant and non resonant parts respectively. As discussed previously in the section for atomic optical susceptibility, the term $\left(\varepsilon_{c,k} - \varepsilon_{v,k}\right)$describes light absorption. On the other hand, the term $\left(\varepsilon_{v,k} - \varepsilon_{c,k}\right)$ describes the amplification of the light field, i.e. optical gain or the laser action. As we do not create the conditions for laser action in our experiment, this term is neglected. Hence optical susceptibility χ(ω) can be calculated as

$$\chi(\omega) = -\sum_k \int \frac{|d_{cv}|^2}{L^3}\left(f_{v,k} - f_{c,k}\right)\left[\frac{1}{\hbar(\varepsilon_{v,k} - \varepsilon_{c,k} + \omega + iq)}\right]$$

Using *Dirac's* identity equation in (see Eq. (3.9)), the expression for optical susceptibility is simplified to

$$\chi(\omega) = -\sum_k \int \frac{|d_{cv}|^2}{L^3}\left(f_{v,k} - f_{c,k}\right)\left[\frac{1}{\hbar(\varepsilon_{v,k} - \varepsilon_{c,k} + \omega)} - i\pi\delta(\varepsilon_{v,k} - \varepsilon_{c,k} + \omega)\right] \qquad (3.22)$$

Optical transition takes place when photon energy $\hbar\omega$ equals $\hbar(\varepsilon_{v,k} - \varepsilon_{c,k})$.

The energy difference in the above equation can be written as

$$\hbar(\varepsilon_{c,k} - \varepsilon_{v,k}) = \frac{\hbar^2 k^2}{2m_c} - \frac{\hbar^2 k^2}{2m_v} + E_g$$

$$= \frac{\hbar^2 k^2}{2m_r} + E_g$$

where m_r is the reduced electron-hole mass given as

$$m_r = \frac{m_e m_r}{m_e + m_r} \tag{3.23}$$

and E_g is the band gap of the semiconductor material.

Since valence band curve is negative, we get negative mass for the electrons there. In order to avoid dealing with negative masses, holes are considered as the quasi particles in the valence band with positive effective mass, i.e. $m_h = -m_v$. Also, Fermi distribution of electrons in conduction band would be $f_{e,k} = f_{c,k}$ and that of holes in valence band would be $f_{h,k} = 1 - f_{v,k}$. In this *electron-hole* notation, the free carrier optical susceptibility expression is simplified to

$$\chi(\omega) = -\sum_k \int \frac{|d_{cv}|^2}{L^3}(1 - f_{e,k} - f_{h,k}) \left[\frac{1}{\omega - \left(\frac{\hbar^2 k^2}{2m_r} + E_g \right)} - i\pi\delta(\omega - \left(\frac{\hbar^2 k^2}{2m_r} + E_g \right)) \right] \tag{3.24}$$

The above equation along with equations (2.8)-(2.11) directly gives us the refractive index and the absorption coefficient of the material. If the summation over k in the above expression is converted to an integral using *1D* density of states, it yields free carrier

optical susceptibility expression exclusively for *1D* regime, i.e. quantum wires that we have considered.

3.3 Inter-band transitions with Coulomb effects: Low excitation regime

In the previous sections, we discussed free carrier susceptibility as Coulomb effects were not considered. Now, we will extend our calculations to accommodate the many body effects as well. The many body Coulomb effects are very important in semiconductors, as they describe the carrier-carrier interactions within the same band, i.e. intra-band interactions. But the optical properties, as we have discussed previously, are mostly related to inter-band transitions. The many body treatment of the *e-h* system in an excited semiconductor crystal affect its spectral properties, i.e. the energy shifts and broadening due to many body interactions. These optical properties, which basically are the renormalizations of the states, are linked with many body interactions depending on the kind of free carriers in the semiconductor. Hence, we eventually have to consider the Coulomb interactions for the accuracy in our treatment.

Let's first consider only the low excitation regime in this section. In that case, the electron and hole density in the semiconductor crystal is very small.

As described previously, polarization is the microscopic sum of all the dipole moments induced by an external field in the material. If we write it as the expected value of the electron dipole "*er"* and integrate over the entire crystal, polarization is calculated as

$$P(t) = \sum \int \partial^3 r \left\langle \psi^t(r,t) er \psi(r,t) \right\rangle$$

Here "ψ^t" represents a Hermitian conjugate of the original function "ψ". If we consider a spatially homogeneous system, then the wave-function could be written in terms of Bloch functions $\psi_\lambda(k,t)$ as

$$\psi(r,t) = \sum_{\lambda,k} a_{\lambda,k}(t) \psi_\lambda(k,t)$$

Following the very same treatment used in equation (3.10)-(3.15), the expression for the polarization in a spatially homogeneous system comes out to be

$$P(t) = \sum_{\lambda,\lambda',k} \left\langle a^t_{\lambda,k}(t) a_{\lambda',k}(t) \right\rangle d_{\lambda\lambda'}$$

$$= \sum_{\lambda,\lambda',k} P_{\lambda\lambda',k}(t) d_{\lambda\lambda'}$$

where $P_{\lambda\lambda'k}(t)$ is a polarization pair function. For a two band model, if λ, λ' are chosen to be valence and conduction band, the polarization pair function is written as

$$P_{vc,k}(t) = \left\langle a^t_{v,k}(t) a_{c,k}(t) \right\rangle$$

Polarization pair function describes the off-diagonal elements of the reduced density matrix. The inter-band density matrix elements would disappear in an equilibrium system without permanent dipole moment. But the optical excitation causes the inter-band transitions and hence the finite values of the inter-band polarization P_{vc}.

3.3.1 Hamiltonian

Let's now define a Hamiltonian *H* of the electrons in conduction and valence bands that take into account the interaction terms due to light field, the Coulomb interaction terms, as well as kinetic energy terms of the non-interacting fermions. As described in equation (3.1), interaction Hamiltonian H_I is the interaction between optical field and semiconductor electrons and can be given as

$$H_1 = \langle -er.E(r,t) \rangle$$

$$= \int \partial^3 r \langle \psi^t(r)[-er].E(r,t)\psi(r) \rangle$$

As we are using an *IR/UV* optical field which has monochromatic space dependence, this excitation field could be modeled as

$$E(r,t) = \frac{\left[e^{iq.r} + e^{-iq.r}\right]}{2} E(t)$$

Hence, the interaction Hamiltonian H_I could be written in terms of Block functions $\psi_\lambda(k,r)$ as the appropriate set for expanding the field operators as

$$H_1 = \sum_k E(t)\left(a^t_{c,k} a_{v,k} d_{cv} + a^t_{v,k} a_{c,k} d_{vc}\right) \tag{3.26}$$

In the above equation, we have considered only two bands and also the dipole approximation, i.e. $q \rightarrow 0$. We can easily interpret from the interaction Hamiltonian term that the optical excitation causes transition of electrons from the valence and conduction band.

Other than the interaction with the external light field, we also have to consider the kinetic and Coulomb contribution from electrons. This Hamiltonian has been derived and used in Ref. [53],[58]-[62] as

$$H_{el} = \sum_{\lambda,k} E_{\lambda,k} a^{t}_{\lambda,k} a_{\lambda,k} + \frac{1}{2} \sum_{\lambda,\lambda',k,k',q\neq 0} V_q a^{t}_{\lambda,k+q} a^{t}_{\lambda',k'-q} a_{\lambda',k'} a_{\lambda,k} \tag{3.27}$$

where V_q is the interaction coulomb potential, while second quantization operators $a^{t}_{\lambda,k}$ and $a_{\lambda,k}$ respectively describe the creation and annihilation of an electron in the band λ and state *k*. Note that, the energies $E_{\lambda,k}$ are defined for a single electron in a lattice. The first summation term includes the kinetic energy of the non-interacting carriers in one band, while the second summation includes the Coulomb contributions in terms of second quantization formalism. We have assumed that Coulomb interaction conserves number of carriers in each band. Hence, it can be observed that when a hole is annihilated in band λ at state *k*, an electron is created in the same band at state ($k + q$). Similarly, a hole is annihilated in band λ' at state *k*, an electron is created in the same band λ' at state ($k- q$). Here again, I must mention the dipole approximation, i.e. $q \rightarrow 0$, so that $q = 0$ in kinetic energy terms. Note that all those coulomb terms which do not conserve the number of electrons in each band, have not been considered in the above equation. These terms describe inter-band scattering which is energetically very unfavorable.

For the two band model, the Hamiltonian H_{el} which considers the kinetic and coulomb contribution from electrons is given as

$$\begin{aligned} H_{el} &= \sum_{k} \left[E_{c,k} a^{t}_{c,k} a_{c,k} + E_{v,k} a^{t}_{v,k} a_{v,k} \right] \\ &+ \frac{1}{2} \sum_{k,k',q\neq 0} V_q \left[a^{t}_{c,k+q} a^{t}_{c,k'-q} a_{c,k'} a_{c,k} + a^{t}_{v,k+q} a^{t}_{v,k'-q} a_{v,k'} a_{v,k} + 2 a^{t}_{c,k+q} a^{t}_{v,k'-q} a_{v,k'} a_{c,k} \right] \end{aligned} \tag{3.28}$$

In equation (3.28), terms in the first summation describe the kinetic energy of non-interacting electrons and holes. The second summation describes the Coulomb interactions of the electrons and holes. The first term inside the bracket describes the *electron-electron* Coulomb interaction, the seconds one represents *hole-hole* interaction, while the last term in the bracket is for *electron-hole* interaction. The first two terms in the bracket give rise to the electron and hole quasi-particle self energies, while the last term in the bracket for *electron-hole* interaction produces the exciton bound state. The single particle energies used in the above equation for conduction and valence band can respectively be given as

$$E_{c,k} = \hbar\varepsilon_{c,k} = E_g + \frac{\hbar^2 k^2}{2m_c}$$

and

$$E_{v,k} = \hbar\varepsilon_{v,k} = \frac{\hbar^2 k^2}{2m_v}$$

Thus, using equation (3.26) and (3.28) total Hamiltonian of the electrons in valence and conduction bands is given by

$$H = H_{el} + H_1 \tag{3.29}$$

where H_1 represents the interaction terms due to light field, H_{el} has the Coulomb interaction terms, as well as kinetic energy terms of the non-interacting fermions.

3.3.2 Inter-band Polarization function

Using the very same procedure with which we calculated Eq. (3.17)-(3.19), we get

$$\hbar\left[i\frac{\partial}{\partial t} - \left(e_{c,k} - e_{v,k}\right)\right] P_{vc,k}(t) = \left[n_{c,k}(t) - n_{v,k}(t)\right]\left[d_{cv}E(t) + \sum_{q\neq k} V_{|k-q|}P_{vc,q}\right]$$

In the above equation, a number operator (second quantization formalism) has been used, i.e. $n_{\lambda,k} = \left\langle a^{t}_{\lambda,k} a_{\lambda,k}\right\rangle$, where *n* is the total number of carriers in band λ. A random phase approximation has been used to obtain the product of densities and inter-band polarizations.

The free particle energy changes on account of the Coulomb interaction of the carriers [55],[59],[63],[64]. Hence, renormalized energies are used in the above equation, which are calculated as

$$\hbar e_{\lambda,k} = \hbar e_{\lambda,k} + (Energy - Correction - Factor)$$

$$= \frac{\hbar^2 k^2}{2m} - \sum_{q\neq k'} V_{|k-q|} n_{\lambda,q} \qquad (3.30)$$

The summation term in the above equation accounts for the shift of single particle energies due to many body (or Coulomb) interactions. This term is also called the exchange self energy term.

As we have used stationary *UV/IR* pulses (stationary as compared to very rapid scattering processes) in our experiment, the system is believed to have attained a *quasi-equilibrium* state. The carrier distribution in this state could be easily approximated by the Fermi-Dirac distributions. Therefore, $n_{c,k} \rightarrow f_{c,k}$ and $n_{v,k} \rightarrow f_{v,k}$

Hence, the above equation for inter-band polarization simplifies to

$$i\hbar\frac{\partial}{\partial t}P_{vc,k}(t) = e_{c,k}(t) - e_{v,k}(t) + \left(f_{c,k}(t) - f_{v,k}(t)\right)\left[d_{cv}E(t) + \sum_{q\neq k} V_{|k-q|}P_{vc,q}\right] \qquad (3.31)$$

If we put $V = 0$ in the above equation, we get the same equation for polarization that we had calculated previously for free carriers.

3.4 The situation of an unexcited quantum wire: The linear optical properties

In our pump-probe experiment, as we illuminate the system with *IR* light of *1308 nm*, to which the *CdS/ZnSe/CdSe/ZnO* quantum wire samples are completely transparent, this could be treated as the case of unexcited semiconductor. Hence, as no carriers are being generated, $f_{c,k} = 0$ *and* $f_{v,k} = 1$. Using this distribution for an unexcited semiconductor, the Fourier transform of inter-band polarization equation (3.31) becomes

$$\left[\hbar(\omega + i\delta) - \left(E_g + \frac{\hbar^2 k^2}{2m_r}\right)\right]P_{vc,k}(\omega) = -\left[d_{cv}E(w) + \sum_{q\neq k} V_{|k-q|}P_{vc,q}(\omega)\right] \qquad (3.32)$$

See equation (3.23) for reduced mass approximation here and the energy terms in the above equation. Note that Fourier transform of $i(\partial/\partial t)$ is $(\omega + i\delta)$, where δ is a positive infinitesimal number.

To solve the above equation, we have to expand P_{vc} into the solution of corresponding homogeneous equation, which actually is called the Wannier equation, given as

$$-\left[\frac{\hbar^2 k^2}{2m_r} + V(r)\right]\psi_v(r) = E_v\psi_v(r) \qquad (3.33)$$

Wannier equation is of the form of two-particle Schrödinger equation for the relative motion of an electron and a hole interacting via the attractive coulomb potential *V(r)*. As in hydrogen atom case, E_v is negative for bound states ($E_v < 0$), while it is positive for ionization continuum states ($E_v > 0$). Note here, that polarization pair equation as well as Wannier equation assumes the coulomb potential to vary little within the unit cell. This assumption would be acceptable only when *e-h* pair Bohr radius a_0 is considerably larger than a lattice constant as in [65].

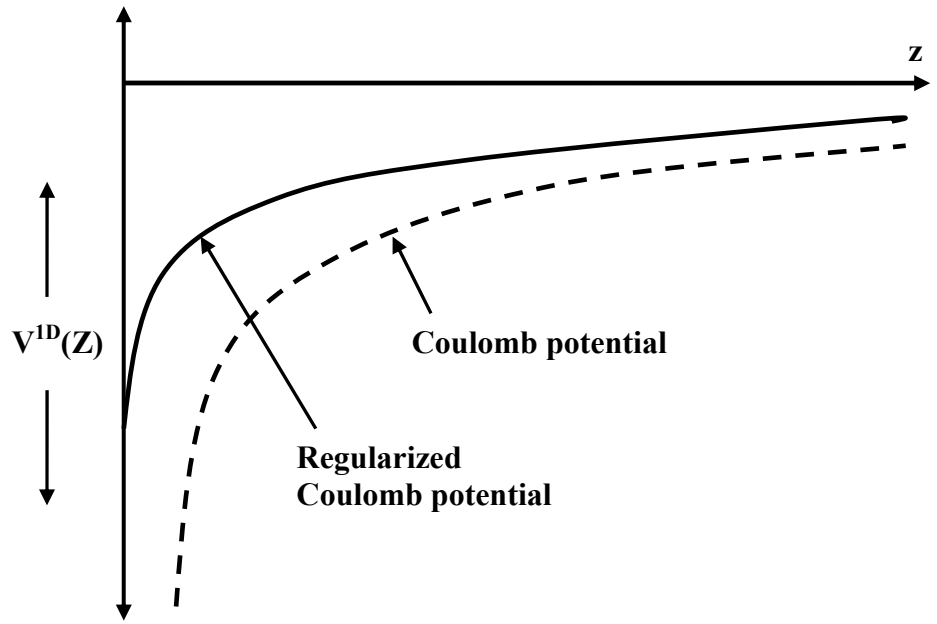

Fig. 3.2 *Quasi-1D* Coulomb Potential [65],[66]

The lattice constant for *CdS* is *5.8 Å* which is considerably smaller than its excitonic Bohr radius of about *28 Å* ($a_{exciton} = a_H \varepsilon_r / \mu$ where excitonic radius in hydrogen a_H is *0.527*

Å). For a quantum wire, the coulomb potential has to be replaced by the envelope averaged potential V_{1D} derived in [65]-[66] developed in the approximation of a cylindrical quantum wire as

$$V^{1D} = \frac{e^2}{\varepsilon_0} \frac{1}{|z| + \gamma R} \tag{3.34}$$

where ε_0 is the background dielectric constant, R is the radius of quantum wire with infinite lateral confinement, z is a relative coordinate of the *e-h* pair and γ is a fitting parameter. This coulomb potential has a cusp type cut-off at $\gamma R \geq 0$. This cut-off has been introduced to avoid the difficulty of divergence and to make the problem analytically solvable. Various cut-offs have been used Ref. [66]-[69], but the one in the equation (3.24) above is the most effective in discussing the optical properties of semiconductor wire structure [60],[70].

We can observe a one-to-one correspondence here with the hydrogen atom, if the proton is replaced by a valence band hole. This Wannier equation is solved in various Quantum Mechanics textbooks like Ref. [48] and [71]. Accordingly, the equation for radial part of the wave function in Wannier equation for a quantum wire is calculated as

$$\left(\frac{\partial^2}{\partial \varsigma^2} + \frac{\lambda}{\varsigma} - \frac{1}{4} \right) f(\varsigma) = 0 \tag{3.35}$$

where

$$\varsigma = \alpha\left(|z| + \gamma R\right)$$

and $$\lambda = \frac{e^2}{\hbar \varepsilon_0} \sqrt{-\frac{m_r}{2E_v}}$$

while α is a scaling constant. Parameter λ is going to be real for bound state and imaginary for ionization continuum. During the course of this derivation, some important terms have also been calculated, which would be required in our further calculations. Hence, exciton Bohr radius is calculated as

$$a_0 = \frac{\hbar^2 \varepsilon}{e^2 m_r} \tag{3.36}$$

while exciton Rydberg energy i.e. energy unit E_0 would be

$$E_0 = \frac{\hbar^2}{2 m_r a_0^2} \tag{3.37}$$

The Wannier equation or the radial part of it has to be solved for bound states which are generally called as Wannier excitons, as well as for ionization continuum states. Variational methods have been used to calculate exciton binding energies and wave functions in Ref.[72]. The effects of excitons on the optical spectra of quantum wires, assuming complete confinement in one direction has been investigated in Ref. [73]-[74]. Excitonic absorption has also been calculated analytically by a fractional dimensional space method in [75], which considers only one sub-band pair. The treatment in Ref. [70] and [76], which we have considered in this work to calculate inter-band polarization (optical properties) of an unexcited semiconductor, considers both the bound (excitonic) states, as well ionization continuum states, while taking into account the effect of mixing many sub-bands. We can also use this method for quantum wires with varying widths. A different, but principally similar approach has been followed in Ref. [77]-[78] to calculate high resolution spectra for both bound and continuum states. However, all these treatments confirm that single sub-band approximation works only for narrow quantum

wires less than about *75 nm*, but they are less accurate beyond *75-100 nm* wide wires. Hence, for narrow quantum wires for widths about *10-50nm*, single sub-band approximation can be considered effectively without any appreciable errors.

3.4.1 Bound states (or excitons where $E_{bound} < E_g$)

The bound state solutions are generally called Wannier excitons. Note here that there are two limiting types of excitons: the Wannier excitons and the Frenkel excitons. We have considered only Wannier excitons, which are the weakly bound states of an electron and a hole. As the spatial extent of the Wannier exciton is much larger than a lattice constant as in our case, its wave-function is more sensitively affected by a spatial geometry than that of the Frenkel excitons.

For a quantum wire, the Wannier equation above is written in the form of a Whittaker equation, as

$$\left(\frac{\partial^2}{\partial \varsigma^2} + \frac{\lambda}{\varsigma} - \frac{1}{4} + \frac{\frac{1}{4} - \mu^2}{\varsigma^2} \right) W_{\lambda,\mu}(\varsigma) = 0 \tag{3.38}$$

where $\mu = \pm 1/2$.

The energy eigenvalues i.e. the *1D* exciton bound state energies for the above equation, are given as

$$E_\lambda = -\frac{E_0}{\lambda^2}$$

where E_0 is the exciton Rydberg energy explained in equation (3.37).

The *1-D* exciton wave-functions for the dipole allowed transitions (i.e. only those wave-functions which couple to the light field) have been calculated in Ref. [53], [65] and [70] as,

$$\psi_\lambda\left(|z|\right) = N_\lambda \tilde{z} e^{-\tilde{z}/2}\Gamma(1+\lambda)\left[F(1-\lambda,2;\tilde{z}) - G(1-\lambda,2;\tilde{z})\right]$$

$$= N_\lambda W_{\lambda,1/2}\left[\frac{2\left(|z|+\gamma R\right)}{\lambda a_0}\right] \tag{3.39}$$

where N_λ is a normalization constant, $W_{\lambda,\mu}$ are the Whittaker functions as given in [79]-[80], Γ is a gamma function, F and G are the fundamental solutions of the confluent hyperbolic equation and

$$\tilde{z} = \frac{2\left(|z|+\gamma R\right)}{\lambda a_0}$$

as given in Ref. [65].

The approximate ground state eigenvalue for the thin wires (applicable for quantum wires that we have used) is determined using the equation

$$\frac{1}{2} + \lambda_0 \ln\left[\frac{2\gamma R}{\lambda_0 a_0}\right] = 0$$

Accordingly, corresponding ground state binding energy is calculated as

$$\left|E_{\lambda 0}\right| = \frac{E_0}{\lambda_0}$$

Note here that, as $\lambda_0 << 1$ for ground state, and even smaller for thin wires, the ground state energy is very large as compared to the exciton Rydberg energy E_0 for an infinite confinement potential. For more realistic confinement potentials in quantum wires, $E_{\lambda 0}$ may be as small as $5E_0$. For higher excited states, the eigenvalues λ_n approaches n, while

Whittaker eigenfunctions take the form of Laguerre polynomials. These higher wave-functions vanish at the origin.

3.4.2 Continuum (ionized) states where $E_v \geq 0$

The states in the ionization continuum with $E_v \geq 0$, (i.e. unbound states) has a continuous energy spectrum. These continuous states, which contribute to the inter-band optical transitions, have the energy

$$E_v = E_k = \frac{\hbar^2 k^2}{2m_r}$$

while λ (See equation 3.35) is calculated as $-i/a_0 k$. Accordingly, the Wannier equation for a quantum wire for the ionization continuum states is given as

$$\left(\frac{\partial^2}{\partial \varsigma^2} - \left(\frac{1}{4} - i\frac{|\lambda|}{\varsigma}\right)\right) f(\varsigma) = 0$$

where

$$\lambda = \frac{e^2}{\hbar \varepsilon_0}\sqrt{-\frac{m_r}{2E_v}}$$

The two independent solutions for the above equation are the Whittaker functions as calculated in Ref. [69], [76] as

$$W^{(j)}_{-i|\lambda|,1/2}(\tilde{x}) = \tilde{x}e^{-\tilde{x}/2}\Gamma\left[1 \pm i|\lambda|\right]\left[F\left(1+i|\lambda|,2;\tilde{x}\right) \pm G\left(1+i|\lambda|,2;\tilde{x}\right)\right] \qquad (3.40)$$

where j=1,2 and $\tilde{x} = 2ik\gamma R$, while F and G are the confluent hyper-geometric functions. Only one of the above Whittaker functions, $W^{(1)}(\tilde{x})$, is optically allowed. Using the

typical normalization procedures, the optically allowed normalized wave-function for the unbound (ionization continuum) state is calculated [65] as

$$\psi_k^{(1)}(\tilde{x}) = \sqrt{\frac{e^{\pi|\lambda|}}{2\pi}} \left[\frac{D_0^{(2)} W^{(1)}(\tilde{x}) - D_0^{(1)} W^{(2)}(\tilde{x})}{\sqrt{\left|D_0^{(1)}\right|^2 + \left|D_0^{(2)}\right|^2}} \right] \tag{3.41}$$

where

$$D_0^{(j)} = \frac{\partial W^{(j)}(\tilde{x})}{d\tilde{x}} \tag{3.42}$$

is calculated at $\tilde{x} = 2ik\gamma R$.

3.4.3 Optical spectra of quantum wires

From the previous sections, we now can calculate the exciton and continuum wave-functions, as well as the energy eigenvalues. Hence, we can solve the inhomogeneous equation (3.31) for the inter-band polarization and obtain the optical spectrum of a semiconductor quantum wire, in an unexcited (unpumped) condition. As the *CdS / ZnSe / ZnO / CdSe* quantum wires that we have used in our experiments are direct band-gap semiconductors, we will restrict our discussion to the optically allowed transitions for direct band-gap semiconductors only. However, the indirect band-gap materials possess much smaller, but finite, transition probability due to the involvement of phonons.

In order to solve equation (3.31), we can expand the polarization function in terms of the Wannier equation solutions

$$P_{vc}(z,\omega) = \sum_{\nu} b_{\nu}\psi_{\nu}(z)$$

Inserting above equation into equation (2.31), we can solve the polarization function as

$$P(\omega) = -2L\sum_{\nu}\left|d_{cv}\right|^2\left|\psi_{\nu}(z=0)\right|^2 E(\omega)\left[\frac{1}{\hbar(\omega+j\delta)-E_g-E_{\nu}} - \frac{1}{\hbar(\omega+j\delta)+E_g+E_{\nu}}\right] \quad (3.43)$$

We already know that $P(\omega) = \chi(\omega)E(\omega)$. Also, as we had discussed previously in the section for free carrier susceptibility, the non-resonant part in the above equation (second fraction in the bracket) does not contribute to absorption and hence neglected. Accordingly, the susceptibility of a quantum wire under unexcited conditions can be calculated as

$$\chi(\omega) = -2L\sum_{\nu}\left|d_{cv}\right|^2\left|\psi_{\nu}(z=0)\right|^2\left[\frac{1}{\hbar(\omega+i\delta)-E_g-E_{\nu}}\right] \quad (3.44)$$

Note here that Coulomb potential has a cut-off at $z = \gamma R$. Using the eigenfunctions for a quantum wire for bound as well as ionization continuum states from equation (3.39) and (3.41) that were described in last two subsections, the susceptibility equation of a quantum wire under unexcited condition is written as

$$\chi(\omega) = -\frac{2L}{E_0}\left|d_{cv}\right|^2[A+B] \quad (3.45)$$

where

A = *Bound State Contribution*

$$= \sum_{\lambda}\left|N_{\lambda}W^2_{\lambda,1/2}\left(\frac{2\gamma R}{\lambda a_0}\right)\right|^2 \frac{E_0}{\hbar(\omega+i\delta)-E_g-E_{\lambda}}$$

and

B = Continuum State Contribution

$$= \frac{2}{a_0}\int_0^{\infty}\left[\partial x \frac{e^{\pi x}}{2\pi}\frac{\left|D_0^{(2)}W^{(1)} - D_0^{(1)}W^{(2)}\right|^2}{\left|D_0^{(1)}\right|^2 + \left|D_0^{(2)}\right|^2}\frac{E_0}{\hbar(\omega + i\delta) - E_g - E_0 x^2}\right]$$

Here $x = a_0 k$ is used as the integration variable in the contribution for the continuum states. Above equation, along with equations (2.8) and (2.11), directly give us the refractive index and the absorption coefficient of the quantum wire under unexcited condition. It has been reported in Ref. [63] and [65] that an absorption spectrum consists of sharp lines due to bound states and a broad absorption band due to ionization continuum.

3.5 High Optical Excitation Condition: Quasi-Equilibrium Regime

In our experiment to investigate the optical properties of the laser excited semiconductor quantum wires, we have used a pump-probe excitation scheme in an optical homodyne setup. The *IR* probe laser pulse prepares the system to be observed using a large area photo-detector, while a pump is used to test it after a variable time period. The *CdS / ZnSe / CdSe / ZnO* quantum wires are transparent to *IR* probe signal at *1308 nm* wavelength. The sample is excited by *365-nm* wavelength *UV* pump beam modulated at *1 KHz* frequency. As the single *UV* pulse appears to be a stationary excitation, or precisely, as the *UV* pulse width is much longer than the carrier scattering time (few picoseconds), the generated carriers reach a thermal *quasi-equilibrium* within their bands. Hence, in this

section, we describe the optical properties when *quasi-equilibrium* electron-hole plasma exists in the quantum wire. This section is an extension to our treatment in previous sections, where we performed the free carrier and low excitation regime calculations.

As the electrons and holes generated due to a long UV have already relaxed to thermal (*quasi*) equilibrium, their distribution can be given by the Fermi distribution as

$$f_{i,k} = \frac{1}{1 + e^{\left(\frac{\hbar^2 k^2}{2m_i} - E_{Fi}\right)/K_B T}}$$

where $i = e, h$ for electrons and holes, $K_B T$ is the thermal energy and E_{Fi} is the quasi-Fermi energy which is determined using the concentration of carriers.

The summation over k space for the electron and hole distribution gives the equation for the total number of electrons and holes at one time instant. Hence,

$$n_i = \frac{2}{L}\sum_k f_{i,k}$$

If we know the number of carriers at an instant in time, we can easily calculate the Fermi energy at that instant. We also, do not have to consider the intra-band scattering processes, as they do not change the total number of electrons and holes. We can also assume charge neutrality so that $N_e = N_h$.

Due to the presence of electron-hole plasma (in quasi-equilibrium state) the bare Coulomb potential is screened. In this regime of stationary field excitation, the screening of the particle-particle interaction is fully developed, and can be described by its equilibrium form. Hence, in bulk (and *2-D*) semiconductors, the bare Coulomb potential has to be replaced by a screened potential in the renormalized single particle energy

equations. But, the screening of Coulomb potential by confined plasma had been discovered to be of little importance in case of quantum wires [66]. Hence, we are using the same envelope averaged *1D* coulomb potential V^{1D} in equation (3.34) in all our calculations. The absorption spectra calculated using screened coulomb potential has been found to not differ substantially from the calculations otherwise [81].

For a constant light field, the stationary equation for the inter-band polarization component using Fourier transform of equation (3.31) is written as

$$\hbar\left(\omega - e_{e,k} - e_{h,k} + i\delta\right)P_k(t) = -\left(1 - f_{e,k} - f_{h,k}\right)\left[d_{cv}E + \sum_{k'} V_{s|k-k'|}P_{k'} \right]$$

where $V_{s|k-k'|}$ stands for Fourier transform of screened coulomb potential explained in equation (2.34), $e_{i,k}$ are renormalized single particle energies (which uses the screened coulomb potential in the calculation of exchange self energy in equation (3.30)). Note that Fourier transform of $i(\partial/\partial t)$ is $(\omega + i\delta)$, where δ is a positive infinitesimal number.

The rate equation for electrons and holes can also be calculated using the renormalized Rabi frequency $\omega_{R,k}$ as

$$\frac{\partial n_k}{\partial t} = -2\,\mathrm{Im}\left(\omega_{R,k}P_k^*\right)$$

where

$$\hbar\omega_{R,k} = d_{cv}E + \sum_{q\neq k} V_{s|k-q|}P_q$$

The polarization equation above can be simplified as

$$P_k(t) = \left[-d_{cv}\frac{\left(1 - f_{e,k} - f_{h,k}\right)}{\hbar\left(\omega - e_{e,k} - e_{h,k} - i\delta\right)} \right]\left[1 + \frac{1}{d_{cv,k}}\sum_{k'} V_{s|k-k'|}\chi_{k'} \right]E(t) \qquad (3.46)$$

As the polarization equation above is linear in the field (it becomes non-linear only via the plasma density which is a function of light intensity), we can introduce a susceptibility function as

$$P_k = \chi_k E$$

Hence, we can write the susceptibility equation for an optically excited quantum wire as

$$\chi_k = \chi_k^0 \left[1 + \frac{1}{d_{cv}} \sum_{k'} V_{s|k-k'|} \chi_{k'} \right] \tag{3.47}$$

where

$$\chi_k^0 = -d_{cv,k} \frac{\left(1 - f_{e,k} - f_{h,k}\right)}{\hbar\left(\omega - e_{e,k} - e_{h,k} - i\delta\right)} \tag{3.48}$$

χ_k^0 is a free carrier susceptibility function calculated in previous section, only that we have used the re-normalized single particle energies in this equation (3.48). Note that the infinitesimal damping term $\delta \rightarrow 0$. The re-normalized single particle energies are calculated as

$$\hbar e_{\lambda,k} = \frac{\hbar^2 k^2}{2m} - \sum_{k \neq k'} V_{|k-k'|} n_{\lambda,k}$$

Therefore, the susceptibility equation above includes the band gap renormalization effects due to electron-hole plasma.

Unlike extremely low-density situations where carrier-phonon and carrier-impurity scattering are the main sources of dissipation, at high-density situations carrier-carrier scattering dominates the de-phasing. We believe that our experiments do not belong into the extremely low-density regime; neither do they fall into the category of high density

situation. In our present discussion, we haven't addressed the mechanism of damping and de-phasing in detail, and they are assumed to be not very relevant. But they are taken into account, as infinitesimal damping factor δ in the susceptibility expression has been replaced by a finite damping γ (de-phasing) of the inter-band polarization to get more realistic optical spectra.

The term in the bracket of the susceptibility equation (3.47) is called the *vertex function* as in [63],[65] and [83]. It is denoted as $\Gamma_{k..}$

If we write the susceptibility equation as,

$$\chi_k = \chi_k^0 \Gamma_k$$

Then, the *vertex function* becomes,

$$\Gamma_k = 1 + \frac{1}{d_{cv,k}} \sum_{k'} V_{s|k-k'|} \chi_{k'}$$

$$= 1 + \frac{1}{d_{cv,k}} \sum_{k'} V_{s|k-k'|} \chi_{k'}^0 \Gamma_{k'} \tag{3.49}$$

The dipole matrix in the above equation can be simplified in effective mass approximation as in [53] and [82] as

$$d_{cv.k} = d_k = \frac{1}{\sqrt{4 m_r E_g}} \left(\frac{e\hbar}{1 + \frac{\hbar^2 k^2}{2 m_r E_g}} \right) \tag{3.50}$$

The solution of the vertex equation above would solve our purpose here. This vertex function is solved using a numerical method to obtain an accurate solution using an Accelerated Fixed Point (AFP) method [84]. In the high density regime, where the carrier

density is greater than the Mott density and exciton bound states cease to exist (i.e. exciton peaks disappear in the absorption spectra), an approximate but simpler Pade method described in Ref. [55], [63], and [85] has been used. The experimental estimated value for the Mott carrier density is $n > 3x10^6$ as given in [82].

3.5.1 Accelerated Fixed Point (AFP) method

If we expand the vertex function Γ_k in equation (2.49) in the form

$$\Gamma_k = 1 + \left[a_1\Gamma_1 + a_2\Gamma_2 + \cdots\cdots\cdots + a_k\Gamma_k + \cdots\cdots\cdots\right]$$

$$(1 - a_k)\Gamma_k = 1 + \left[a_1\Gamma_1 + a_2\Gamma_2 + \cdots\cdots\cdots + a_{k-1}\Gamma_{k-1} + a_{k+1}\Gamma_{k+1}\cdots + \cdots\cdots\cdots\right]$$

and finally

$$\Gamma_k = \frac{1 + \left[a_1\Gamma_1 + a_2\Gamma_2 + \cdots\cdots\cdots + a_{k-1}\Gamma_{k-1} + a_{k+1}\Gamma_{k+1}\cdots + \cdots\cdots\cdots\right]}{(1 - a_k)} \qquad (3.51)$$

Hence, we can solve the above function iteratively, by accelerating it using a damped extrapolation scheme and updated values of Γ_k as they are available [84]. The integral is approximated by using a discrete sum with about *100* terms as

$$\sum_{k'} \to \int \frac{\partial k'}{2\pi} \to \sum_{k'} \frac{\Delta k_i^{'}}{2\pi}$$

The points could be taken equidistantly, but better accuracy is obtained if the k_i are taken as the points of support of a Gaussian quadrature.

The Coulomb potential term in the vertex function in equation (3.49) becomes singular for ($k = k'$)at low densities. This singularity has to be removed before the AFP iterations are performed.

Finally, complex susceptibility is calculated as

$$\chi(\omega) = \frac{1}{L}\sum_{k} d_{cv}^{*}\chi_{k} \tag{3.52}$$

Hence, complex dielectric function $\varepsilon(\omega)$ can be calculated using the relation $\varepsilon = (1+\chi)$. Using equations (2.8) and (2.11), we can calculate the absorption coefficient $\alpha(\omega)$ and ordinary refraction index $n(\omega)$.

3.5.2 Pade approximation method

Number of carriers generated in semiconductor quantum wire depends upon the light intensity. We have used a *365-nm* light source with a maximum *100 mW* intensity, a Nichia *LED*, as a source of *UV* excitation. While the *LED* is being operated at higher intensity, more light will be absorbed by the quantum wires and more carriers would be generated. In this high density limit, the attractive potential between the electrons and holes becomes weak. Here, plasma screening and phase-space occupation reduce the strength of the Coulomb potential. In that case, we can approximately solve equation (3.49) using Pade approximation method [63]. A power expansion of vertex function in equation (2.49) could be written in terms of interaction parameter λ as

$$\Gamma_{k} = \sum_{n} q_{n}\lambda^{n}$$

The interaction parameter λ is assumed to be very small. The first coefficient q_1 is calculated as

$$q_1 = \frac{1}{d_{cv}} \sum_{k'} V_{s,|k-k'|} \chi^0_{k'}$$

Vertex function in equation (3.49) could also be expressed in terms of the ratio of two polynomials as

$$P^{N,M}(k,\omega) = \frac{\sum_{n=0}^{N} r_n \lambda_n}{\sum_{m=0}^{M} s_m \lambda_m}$$

where $P^{NM}(k,\omega)$ is the *(N,M) Pade approximation*. r_n and s_n can be evaluated by comparing the above two expansions. The simplest form of *(0-1)* type *Pade* approximated vertex is calculated in [63] as

$$\Gamma_k = P_k^{(0,1)} = \frac{1}{1-q_{1k}}$$

$$= \frac{1}{1 - \frac{1}{d_{cv}} \sum_{k'} V_{s,|k-k'|} \chi^0_{k'}} \tag{3.53}$$

Accordingly, the optical susceptibility can be calculated as

$$\chi(\omega) = \frac{1}{L} \sum_k \frac{d^*_{cv} \chi^0_k}{1-q_{1k}} = \frac{1}{L} \sum_k \frac{d^*_{cv} \chi^0_k}{1 - \frac{1}{d_{cv}} \sum_{k'} V_{s,|k-k'|} \chi^0_{k'}}$$

Hence, complex dielectric function $\varepsilon(\omega)$ can be calculated using the relation $\varepsilon = \varepsilon_0(1+\chi)$ and, using equations (2.8) and (2.11), we can calculate the absorption coefficient $\alpha(\omega)$ and refraction index $n(\omega)$.

3.6 Numerical calculations using Mathematica

We have developed a program in Mathematica (see Appendix A) to numerically solve the theoretical models described in previous sections and obtain various optical parameters like susceptibility (χ), complex permittivity ($\varepsilon = \varepsilon' + j\varepsilon''$), absorption coefficient (α), refractive index (n), excitonic Bohr radius (a_0), etc. As we have chosen quantum wire arrays of four different materials deposited in porous Alumina, namely *CdS, CdSe, ZnO and ZnSe*, of three different diameters (*50 nm, 25 nm and 10 nm*), the program is written for each one of them. We first developed a dummy program for the quantum wires of materials with known optical parameters (*GaAs*) and then modified it to accommodate other materials. As the experiments are carried out at low *UV* intensities (of the order of few *mWatts* per cm^2, small number of carriers are photogenerated inside the quantum wire materials. Hence, Pade method as described in the last section for high density approximation is not valid here. Therefore, we consider only AFP method for the numerical solutions.

In the calculations, like all the other parameters, the intrinsic carrier density inside the quantum wires is extremely important for the accurate solutions. However, it is very difficult to experimentally determine its accurate value in the quantum wires deposited in

porous alumina structures due to practical constraints. As of now, the intrinsic carrier concentration has not been reported for these nanostructures. Therefore, we have to make certain practical assumptions, within applicable limits, to proceed further with our calculations. In our Mathematica programs, we have used published values of intrinsic carrier concentrations for the bulk materials. A small variation in the carrier concentration, brings about a large change in the *quasi-Fermi* levels for electrons and holes, which effectively alter the final values of the optical parameters. To avoid these errors appearing in our calculations, we have used a fitting parameter in the model values of the *quasi-Fermi* levels. The fitting parameters are adjusted such that, at the excitation wavelength of *1308 nm,* the permittivity values calculated for the quantum wires made of certain semiconductor material match the published bulk values for those materials, in a limit when length L and radius R of the quantum wires are very large. We have used the bulk model where L and R are extended to *10 microns* each, as these lengths are considerably larger than the laser wavelength.

As explained earlier in this chapter, the electrons and holes generated due to stationary *UV* excitation that we used in our experiments are relaxed to their *quasi* thermal equilibrium. This means, the carriers are at thermal equilibrium among themselves in their respective bands, but the total crystal is out of thermodynamic equilibrium. Under this assumption, the carrier distribution is given by *Fermi* distribution $f_{i,k}$.

$$f_{i,k} = \frac{1}{1 + Exp[\frac{1}{K_B T}\left(\frac{\hbar^2 k^2}{2m_i} - E_{Fi}\right)]}$$

where $i = e, h$ stands for the carriers, while E_{Fi} represents their *quasi-Fermi* levels. In case of thermal equilibrium of the carriers, represented by *Fermi-Dirac* distribution, equal number of carriers exists and *Fermi* level remains identical for both the types of carriers. On the other hand, for non-thermal generation of carriers such as photo-generation or injection, more carriers exist than are present at temperature T as dictated by the normal *Fermi-Dirac* distribution. Therefore, in case of photo-generated carriers, their distribution does not obey the *Fermi-Dirac* distribution. In this case, the position of the Fermi levels cannot simultaneously describe the number of free electrons and holes. Instead *Fermi* levels split into two quasi Fermi levels E_{Fc} and E_{Fv} for the conduction and valence band electrons, respectively. In such condition, the Fermi distribution function is modified to

$$f_{c,k} = \frac{1}{1 + Exp[\frac{E_k - E_{Fc}}{K_B T}]} \tag{3.54-A}$$

and

$$f_{v,k} = \frac{1}{1 + Exp[\frac{E_{Fv} - E_k}{K_B T}]} \tag{3.54-B}$$

where, E_{Fc} and E_{Fv} represent the *quasi-Fermi* levels. Here, we have to be careful about the sign conventions. Since the valence band curve is negative, we get negative mass for the electrons (holes) there. We must mention here again, that the holes are considered as the quasi particles in the valence band with positive effective mass, i.e. $m_h = - m_v$.

Also, $f_h = 1 - f_v$.

We know that summations over *k*-space for electron and hole distributions give the equation for total number of electrons and holes, as

$$n_i = \frac{2}{L}\sum_k f_{i,k} \tag{3.55}$$

where L is the length of the quantum wire. If *Boltzman* approximation is used for room temperature distribution, *quasi-Fermi* levels are calculated using equations (3.54) and (3.55) as

$$E_{F,e} = E_g + latconf + K_B T.\ln\left(\frac{n_e L}{2\sum_k e^{-\frac{\hbar^2 k^2}{2m_e K_B T}}}\right)$$

and

$$E_{F,h} = -K_B T.\ln\left(\frac{n_h L}{2\sum_k e^{\frac{\hbar^2 k^2}{2m_h K_B T}}}\right)$$

Here, *latconf* is the lateral confinement factor for the quantum wire, explained later in this section. For our calculations, we have considered a *1-D* quantum wire of radius *R* such that $R << L$, where L is the length of the wire. The quantum wires are considered to be *1 micron* in length. We have used envelope averaged, non-singular *1D* interaction coulomb potential given in equation (3.34). Under this condition, the electron wave-function is written as [86]

$$\psi_{lj,k} = \frac{e^{ikz}}{\sqrt{L}} C_j^l J_l\left(x_j^l \frac{r}{R}\right) e^{il\varphi}$$

where $r = (r,\varphi,z)$ are the cylindrical co-ordinates, C_j^l is the normalization factor, and x_j^l is the j_{th} zero of l_{th} order Bessel function J_l.

The envelope wave-function corresponding to the lowest confinement energy level is then calculated as [53]

$$\psi_{0,0} = \frac{J_0(\alpha_0 r / R)}{\sqrt{\pi} R J_1(\alpha_0)}$$

Hence, the lowest confinement energy level *latconf* is given as

$$latconf = \frac{\alpha_0^2 \hbar^2}{2mR^2} \tag{3.56}$$

where $\alpha_0 = 2.405$ is the first zero of zeroth order spherical Bessel function $J_0(x) = 0$.

Accordingly, in Mathematica, conduction band energy is calculated as

$$\varepsilon_e(k) = E_g + latconf + \frac{\hbar^2 k^2}{2m_e} + \Delta\varepsilon_e(k) \tag{3.57}$$

where $\Delta\varepsilon_e(k)$ is the energy correction factor defined in equation (2.30). Similarly, the valence band energy (for holes) is calculated as

$$\varepsilon_h(k) = \frac{\hbar^2 k^2}{2m_h} - \Delta\varepsilon_h(k) \tag{3.58}$$

Free carrier susceptibility is then calculated using equation (3.48).

Vertex function in equation (3.49) is calculated using dipole matrix element in equation (3.50) and the *Fourier Transform* equation of screened Coulomb potential. The equation for the *Fourier Transform* of screened Coulomb potential as explained in [61] and [81] is written as,

$$F\left(V^{1D}\right)=V_q=\frac{e^2}{L\varepsilon}Exp\left(\frac{\hbar^2k^2}{4m\Omega}\right)K_0\left(\frac{\hbar^2k^2}{4m\times latconf}\right) \tag{3.59}$$

where K_0 is the zero[th] order *modified Bessel Function*. This Coulomb potential has logarithmic divergence for small values of *k*, which is typical for *1-D* system, while it decreases for large values of *k* as the corresponding *2-D* potential.

We have used an Accelerated Fixed Point method [84], explained in the previous section, to solve the *k-dependent Vertex function* in equation in (3.49). To obtain good convergence and accurate solutions, the integrals involved in all the calculations have been approximated using a discrete sum of *100* points spread equidistantly over the lattice space of $2\pi/a_0$, as explained in section 3.5.1. If "a_0" is considered as the lattice constant of the material used, *100 k-points* are distributed equidistantly over the lattice space such that

$$-\frac{\pi}{a_0}\le k\le\frac{\pi}{a_0}$$

As, it could be observed in equations (3.49) and (3.51), the value of the *k-dependent vertex function* at each of these *100 k-points* spread equidistantly over the whole lattice also depends on the other *vertex functions* at the remaining *99 k-points* over the lattice space. This recursive *vertex function* is solved iteratively using numerical techniques. As $\chi_k=\chi_k^0\Gamma_k$, if we consider that the numerical value of optical susceptibility χ_k would be closer to its free carrier counterpart χ_k^0, then $\Gamma_k=1$. Hence, we begin the iterative solution with the initial value of $\Gamma_k=1$ for all *100 k-points*. During the first iteration, equation (3.51) is first solved for Γ_k at $k=-(\pi/a_0)$, and this updated value is used in

the calculation of $\Gamma_{k+\Delta k}$ where $\Delta k = \frac{1}{100}\left(\frac{2\pi}{k}\right)$. Accordingly, during the first iteration cycle, all the Γ_k values over the lattice space are calculated by using updated values at all the previous *k-points*. The convergence criterion is set such that $\left[\Gamma_k(n) - \Gamma_k(n-1)\right] / \Gamma_k(n) \leq 10^{-6}$. We ran the Mathematica programs for about *11-13* such iterations to reach a good convergence.

Alternatively, the program could be simplified by using the Γ_k values from the previous iteration for all the *100 k-points*. Accordingly, Γ_k values for all the *100 k-points* in the first iteration are calculated with an initial assumption of $\Gamma_k = 1$ for all *100 k-points*. Hence, Γ_k values (of equation (3.51)) are updated in every iteration using the corresponding Γ_k values in the previous iteration. This approach is rather slower with regards to convergence; however required processing time in Mathematica is improved. It also has an added advantage that the program is much simpler as compared to the previous approach. In this approach, about *16-19* iterations are required to reach a convergence within permissible limits.

Finally, equation (3.52) is used to calculate the susceptibility value for the quantum wires at *1308 nm* of excitation wavelength. This susceptibility value is then utilized to calculate other optical parameters for the quantum wire under consideration, as explained in section 2.2.

To obtain the optical parameters of a single quantum wire, the information about several material parameters is required. Some of those important material parameters for all four

semiconductor materials, namely *CdS, CdSe, ZnO and ZnSe*, which are deposited in the nano-pores of porous alumina templates, are given in Table 1.

		CdS	*ZnSe*	*CdSe*	*ZnO*
Band-gap (*eV*)	E_g	**2.5** [87],[88], [105]	**2.69** [87]-[88],[105]	**1.74** [87],[94],[95],[101], [102],[104]	**3.35** [87],[93]-[95],[104]
Lattice Constant (*Å*)	a_0	**5.83** [87],[88]	**5.6686** [88]	**6.084**	**5.2069** [87]
Carrier mass	m_e / m_0	**0.2** [88]	**0.16** [88]	**0.13** [88],[105]	**0.24** [105]
	m_h / m_0	**0.45** [88]	**0.6** [88]	**0.43** [88],[105]	**0.78** [105]
Static dielectric constant	ε_0	**8.9** [87],[97]-[101]	**9.12** [87],[89]-[92]	**9.29** [87],[94],[95],[101]-[103]	**8.1** [87],[96], [104]

Table 1 Material parameters for quantum wire semiconductor materials

In Mathematica, during the process of calculating the optical parameters of the quantum wires under consideration, few important points are to be taken care of. A constant value

of infinitesimal damping factor δ (for de-phasing) is used, its value is assumed extremely small such that $\hbar\delta = 0.2meV$.

As we mentioned earlier, intrinsic carrier concentrations in the self-assembled quantum wires are not reported anywhere as of now. Being wide bandgap semiconductors, the un-doped quantum wires under consideration are expected to have extremely small amount of intrinsic carrier concentration. The self-assembled quantum wires, although fabricated by selectively electro-depositing un-doped semiconductor materials in porous alumina, are un-intentionally doped due to the presence of trap (interface) states at the alumina-semiconductor interface. The concentration of interface states in the electrochemically self-assembled quantum wires is approximately calculated as ~10^{13} /cm^2 [106]. If we assume that each trap is singly charged, for a wire with diameter *d*, and length *L*, the total carrier concentration is calculated as follows

$$Carrier - Concentration = 10^{13} \times \frac{wire - surface - area}{wire - volume}$$

$$= 10^{13} \times \frac{\pi \times d \times L}{\pi \times (d^2/4) \times L} \qquad (3.60)$$

Accordingly, the un-excited carrier concentration is calculated as 8×10^{18}, 1.6×10^{19}, 4×10^{19} /cm^3 for 50-, 25- and 10-nm diameter wires respectively. Note here that the presence of interface states makes the value of the carrier concentration as a function of wire diameter and is completely independent of the semiconductor material. We can observe that the carrier concentration increases with the reduction in wire diameter. However for practical reasons where all the trap states are not responsible for carrier generation, the values of the carrier concentration used in Mathematica program are in

the range of 10^{15}-10^{16} /cm^3. As these are the approximate values, a fitting parameter is added to the carrier *quasi-fermi* levels in the Mathematica program, which are the functions of carrier concentration. The *quasi-fermi* levels are adjusted such that the final permittivity values (at *1308 nm*) approach the published bulk values for these materials, in the limit when length *L* and radius *R* of the quantum wires are of the order of *10 microns*. Table 2 gives bulk values of the permittivity for *CdS, CdSe, ZnO and ZnSe* at an excitation wavelength of *1308 nm* (*0.95 eV*).

	CdS	**ZnSe**	**CdSe**	**ZnO**
Dielectric constant $\varepsilon/\varepsilon_0$	5.4	6.0355	6.2601	3.7334
References	[87], [97]-[101]	[87]-[92]	[87],[103]	[87],[96]

Table 2 Static dielectric constant of the quantum wire semiconductor materials at *0.95 eV* at (*1308 nm*) and *300* ^0K in bulk

Instead of using a random value of the fitting parameters, we have used Rydberg energy dependent fitting parameters. Rydberg energy unit E_0, which is a unique value for every semiconductor material, is calculated using equation (3.37) as

$$E_0 = \frac{\hbar^2}{2ma_0^2} = \frac{e^4 m}{2\hbar^2 \varepsilon^2}$$

where a_0 is the exciton Bohr radius, m is the reduced mass ($m = \frac{m_e m_h}{m_e + m_h}$), and ε is the dielectric constant of the quantum wire material. The value of the fitting parameter that we have used in the Mathematica program varies between $0.5\ E_0$ to $3.5\ E_0$. The Rydberg energy unit E_0 for various semiconductor materials that we have used varies between *10 meV to 40 meV*.

Table 3 – Table 6 show the optical parameters calculated for *CdS, ZnSe, ZnO and CdSe* quantum wires respectively. Each table gives these optical parameters calculated for bulk, as well as for wires with *50-, 25- and 10-nm* diameters. The parameters include lateral confinement energy Ω in *meV*, complex susceptibility χ, complex permittivity ε, as well as absorption coefficient α and refractive index n. We have also mentioned the values for the Bohr excitonic radius and Rydberg energy for each material, as well as the fitting parameter used (in the carrier *quasi-fermi* energy values) in each Mathematica program.

Quantum wire Material: CdS

Excitonic Bohr radius : *3.82991 nm*

Rydberg energy unit (E_0) : *20.6134 meV*

Fitting parameter in E_F : *2.247* E_0

Parameters	***symbol***	***bulk***	***50 nm***	***25 nm***	***10 nm***
latconf (meV)	***Ω***		**2.55273**	**10.2109**	**63.8183**
Complex Susceptibility	***χ′***	**0.350239**	**0.349311**	**0.346547**	**0.328106**
	j χ”	**0.000271381**	**0.00027021**	**0.000266735**	**0.000244024**
Complex permittivity	***ε′***	**5.401234042**	**5.389569828**	**5.354838769**	**5.12310009**
	j ε″	**0.00341027**	**0.003395554**	**0.003351889**	**0.003066493**
Loss tangent	$\delta \times 10^{-3}$	**0.631**	**0.630**	**0.626**	**0.616**
Refractive index	***n***	**2.324055632**	**2.321544822**	**2.314052469**	**2.263426905**
Absorption coefficient (1/cm)	***α***	**70.48791**	**70.25961**	**69.58071**	**65.081**

Table 3 Optical parameters calculated for CdS using Mathematica

Quantum wire Material: ZnSe

Excitonic Bohr radius : *3.40967 nm*

Rydberg energy unit (E_0) : *23.7263 meV*

Fitting parameter in E_F : *3.078* E_0

Parameters	***symbol***	***Bulk***	***50 nm***	***25 nm***	***10 nm***
latconf (meV)	***Ω***		**2.79819**	**11.1927**	**69.9547**
Complex Susceptibility	***χ′***	**0.40054**	**0.399495**	**0.396386**	**0.375619**
	j χ”	**0.0002383**	**0.000237294**	**0.000234307**	**0.000214756**
Complex permittivity	***ε′***	**6.03332796**	**6.020206432**	**5.98113021**	**5.720172431**
	j ε″	**0.002994566**	**0.00298192**	**0.002944387**	**0.002698705**
Loss tangent	$\delta \times 10^{-3}$	**0.496**	**0.495**	**0.492**	**0.472**
Refractive index	***n***	**2.456283439**	**2.453610972**	**2.445635004**	**2.391688263**
Absorption coefficient (1/cm)	***α***	**58.56361**	**58.37981**	**57.8331**	**54.2031**

Table 4 Optical parameters calculated for ZnSe using Mathematica

Quantum wire Material: ZnO

Excitonic Bohr radius : *2.34116 nm*

Rydberg energy unit (E_0) : *37.9679 meV*

Fitting parameter in E_F : *2.388* E_0

Parameters	***symbol***	***bulk***	***50 nm***	***25 nm***	***10 nm***
latconf (meV)	***Ω***		1.92588	7.70351	48.1469
Complex Susceptibility	***χ′***	0.217258	0.216956	0.216058	0.209916
	j χ”	0.000177523	0.00017713	0.000175957	0.00016803
Complex permittivity	***ε′***	3.730147177	3.726365031	3.715059233	3.637877249
	j ε″	0.002230819	0.002225879	0.002211136	0.002111524
Loss tangent	$\delta \times 10^{-3}$	0.598	0.597	0.595	0.580
Refractive index	***n***	1.93135898	1.930379591	1.927448978	1.90732209
Absorption coefficient (1/cm)	***α***	55.48471	55.38991	55.10671	53.17951

Table 5 Optical parameters calculated for ZnO using Mathematica

Quantum wire Material: CdSe

Excitonic Bohr radius : *4.88584 nm*

Rydberg energy unit (E_0) : *15.8627 meV*

Fitting parameter in E_F : *0.6864* E_0

Parameters	*symbol*	*bulk*	*50 nm*	*25 nm*	*10 nm*
latconf (meV)	***Ω***		**3.50434**	**14.0174**	**87.6085**
Complex Susceptibility	***χ′***	**0.418672**	**0.416146**	**0.408706**	**0.362036**
	j χ”	**0.000398698**	**0.000394605**	**0.000382658**	**0.000311472**
Complex permittivity	***ε′***	**6.261191275**	**6.229445099**	**6.135948167**	**5.549478957**
	j ε″	**0.00501019**	**0.004958747**	**0.004808619**	**0.003914073**
Loss tangent	$\delta \times 10^{-3}$	**0.800**	**0.796**	**0.784**	**0.705**
Refractive index	***n***	**2.502237454**	**2.495885832**	**2.477084801**	**2.355733357**
Absorption coefficient (1/cm)	***α***	**96.18291**	**95.43761**	**93.25061**	**79.81321**

Table 6 Optical parameters calculated for CdSe using Mathematica

The plot in Fig. 3.3 shows the confinement energy (in *meV*) as a function of quantum wire diameter. Using Mathematica, we calculated these values for quantum wires with six different diameters, including *100 nm, 50 nm, 25 nm, 15 nm, 10 nm and 5 nm*. This data has been calculated for the wires of all four materials that we have been using, namely *CdS, ZnSe, ZnO and CdSe.*

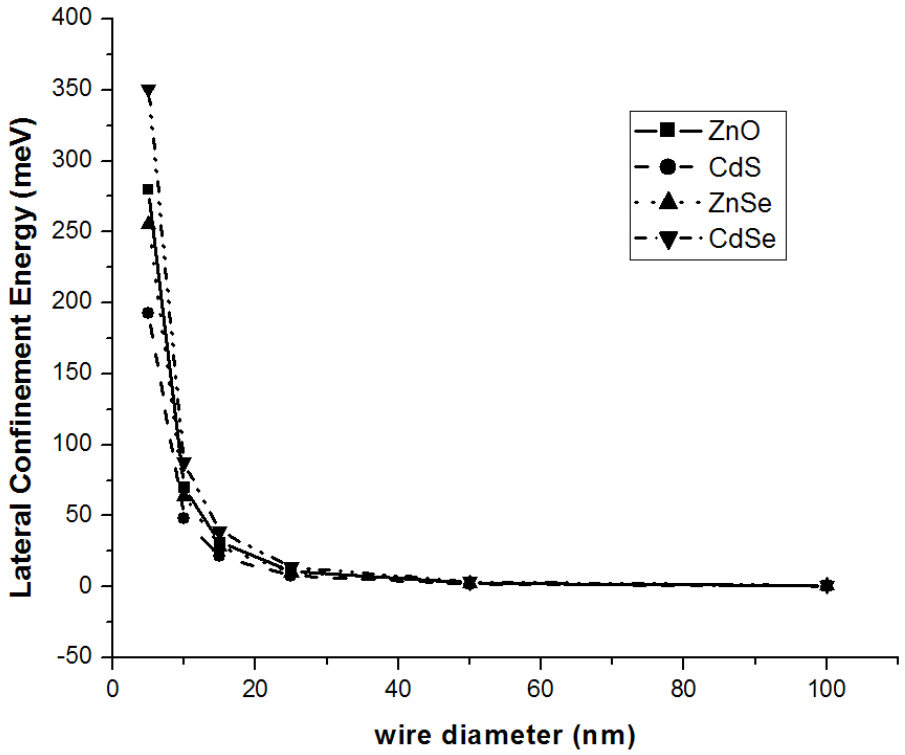

Fig 3.3 Lateral confinement energy (in *meV*) for quantum wires of different materials and diameters, including *100/50/25/15/10/5 nm*.

We can observe that lateral confinement energy *Ω* (*meV*) increases very slowly with decreasing diameters in quantum wires with large diameters. It remains very small, and almost constant (or rises with an extremely small slope) as the diameter reaches *25-20 nm*

starting from bulk value. We can observe a very steep rise in the confinement energy, as the diameter decreases further, from about *20 meV* to *200 meV* and more.

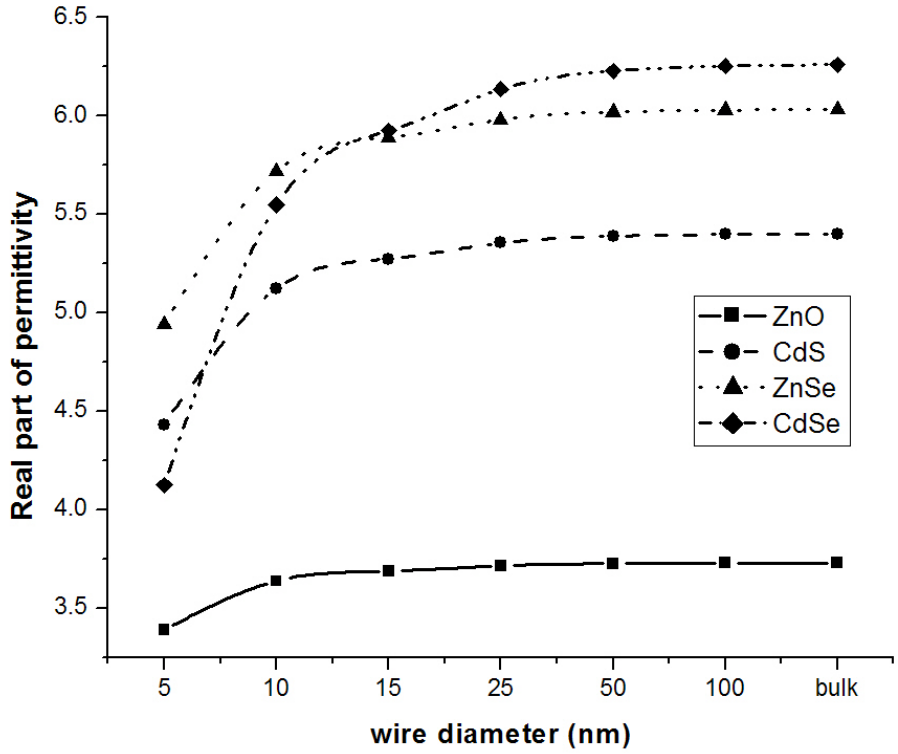

Fig. 3.4 Variation of unexcited quantum wire permittivity with diameters

Fig. 3.4 shows the variation of permittivity in all four types of unexcited quantum wires, as a function of their diameters. Unlike the plots for lateral confinement energy Ω, the permittivity of quantum wire reduces sharply at the lower diameters. It first reduces extremely slowly as the diameter is reduced from bulk to about *25 nm* diameter, and then follows a steep slope down, as diameter reduces further. A peculiar thing to be noted

here is that the permittivity reduction in *CdSe* starts earlier as compared to other materials. Also, the slope is steeper in case of *CdSe*.

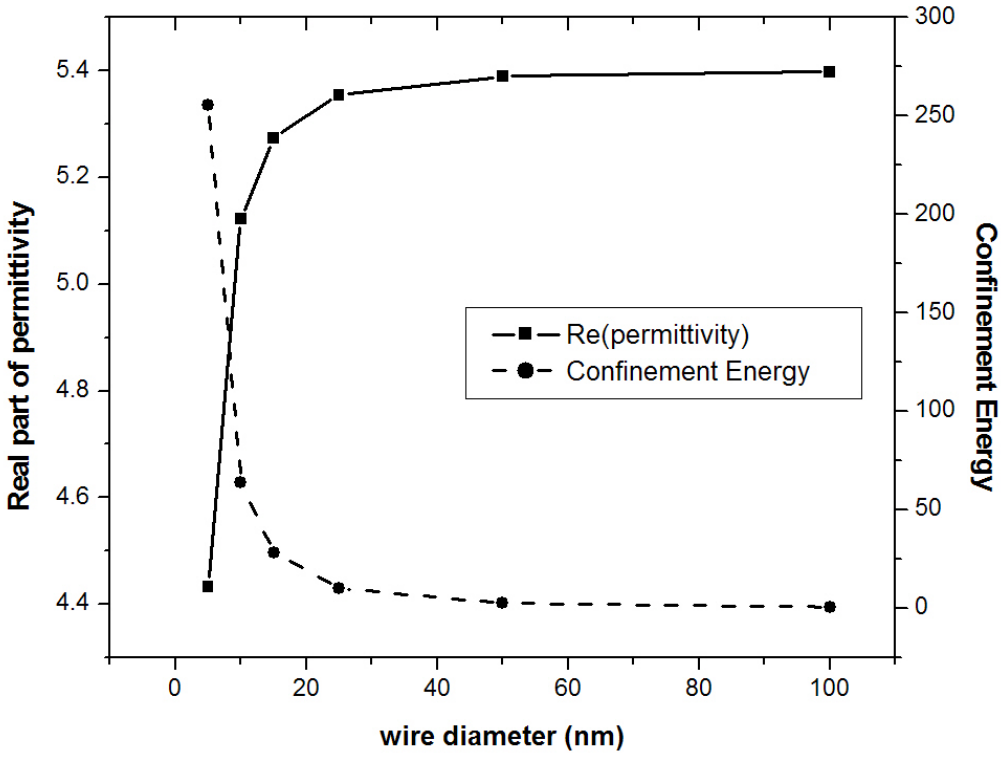

Fig. 3.5 Real part of permittivity vs Confinement energy variations with diameter for unexcited CdS wires

Fig. 3.5 displays the comparative variation in real part of permittivity and confinement energy Ω with diameter in the unexcited CdS quantum wires. This is a very important graph for our further analysis, while we study the experimental performance of the quantum wires. As the diameter of the quantum wire reduces, the change in lateral confinement is of the order of *200-300* times the initial bulk value. On the other hand, this large change in the confinement energy due to the variations in the diameter of the

quantum wire causes large changes (reduction) in their respective permittivity values. Theoretically, a change in the wire diameters, and hence the confinement of the energies is a major source of permittivity variations in the quantum wires, but more effects are to be taken into account when they are excited by *UV* radiation. We observe extremely small variations in the permittivity of the quantum wires during our experiments, when they are exposed to *UV* radiation. These small variations are attributed to various factors including the diameter of the quantum wires, their filling factor in the porous alumina, as well as the trap states distributed in the alumina. These effects will be discussed in detail in Ch. 6 and Ch. 7.

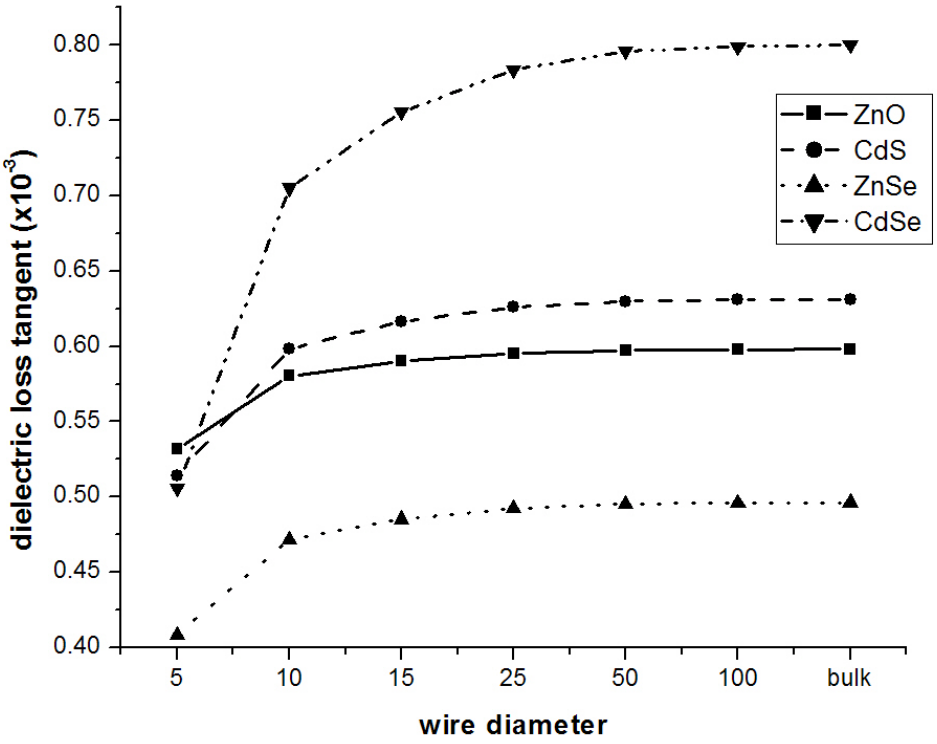

Fig. 3.6 Variations in dielectric loss tangent with the quantum wire diameters

Fig. 3.6 is the plot of dielectric loss tangent of the unexcited quantum wires of four different materials with the variations in their diameters. For a semiconductor material with complex dielectric constant ($\varepsilon = \varepsilon' + j\varepsilon''$), loss tangent δ is defined as ($\tan(\delta) \approx \delta = \varepsilon'' / \varepsilon'$). The dielectric loss tangent is the measure of the losses in the semiconductor material, as it represents the material that dissipates power of a high frequency electric field. The larger the value of the loss tangent, more lossy the material is.

As the wire diameter reduces, we can see that the value of the loss tangent also reduces. Our data suggests that both the real and imaginary parts of the permittivity reduce with wire diameters. But as loss tangent delta is the ratio of imaginary to real part of the permittivity ($\delta = \varepsilon'' / \varepsilon'$), the imaginary part reduces faster than the real part. This means that the losses in the quantum wire reduce with its diameter. In other words, absorption coefficient of the quantum wires, or the number of photo-generated carriers would reduce with the wire diameter. Dielectric loss tangent is found to be reduced to about *60-80%* in *5 nm* diameter wire, when compared with the bulk values.

Similar plots for the variations in absorption coefficients and refractive indices of the unexcited quantum wires are displayed in Fig. 3.7. We can see that *CdSe* with smallest band-gap (*1.74 eV*) and largest lattice constant (*6.084 Å*) of the four materials happens to have the largest value of dynamic refractive index and the absorption coefficient. On the other hand, *ZnO* with largest band-gap (*3.35 eV*) and smallest lattice constant (*5.2069 Å*) of the four materials have the smallest value of dynamic refractive index and the absorption coefficient. However, ZnO also has the smallest value of static dielectric permittivity (*8.1*), while CdSe has the largest (*9.29*).

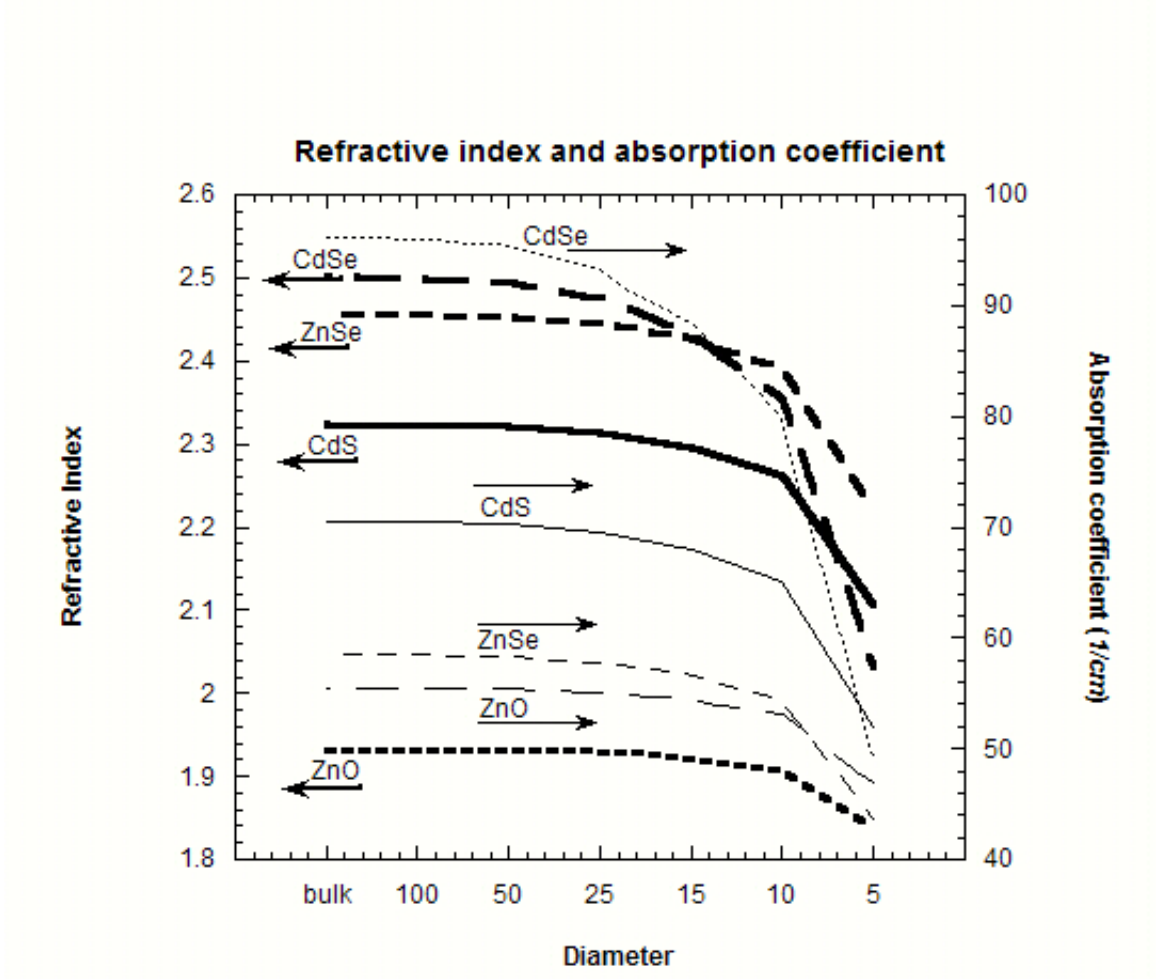

Fig. 3.7 Variations in the refractive index (n) and absorption coefficient (α) of the quantum wires with their diameters.

CHAPTER 4

Electromagnetic Wave Simulations

4.1 High Frequency Structure Simulation (HFSS)

We use Ansoft Corporation's High Frequency Structure Simulator (*HFSS*) for the electromagnetic wave simulations. *HFSS* is the industry-standard software for the electromagnetic simulations of high-frequency and high-speed components. It is a full wave electromagnetic simulator for arbitrary *3D* volumetric passive device modeling and utilizes a *3D* full-wave Finite Element Method (*FEM*) to compute the electromagnetic wave behavior of structures. With *HFSS*, we can extract network parameters (*S, Y, Z*), visualize *3-Dimensional* electromagnetic fields (near and far-field), generate broadband *SPICE* models, and optimize the design performance of the device under investigation. Using *HFSS*, we can accurately characterize and effectively evaluate wave properties, including transmission path losses, reflection loss due to impedance mismatches, parasitic coupling, and radiations. *HFSS* also allows us to draw the device structure, specify the material characteristics for each object, and identify the excitation ports and any special surface characteristics. It then generates the necessary field solutions for the specified excitations. The block diagram of the *HFSS* simulator is given in Fig. 4.1. In section 4.1, we discuss the major building blocks of *HFSS* that we have used.

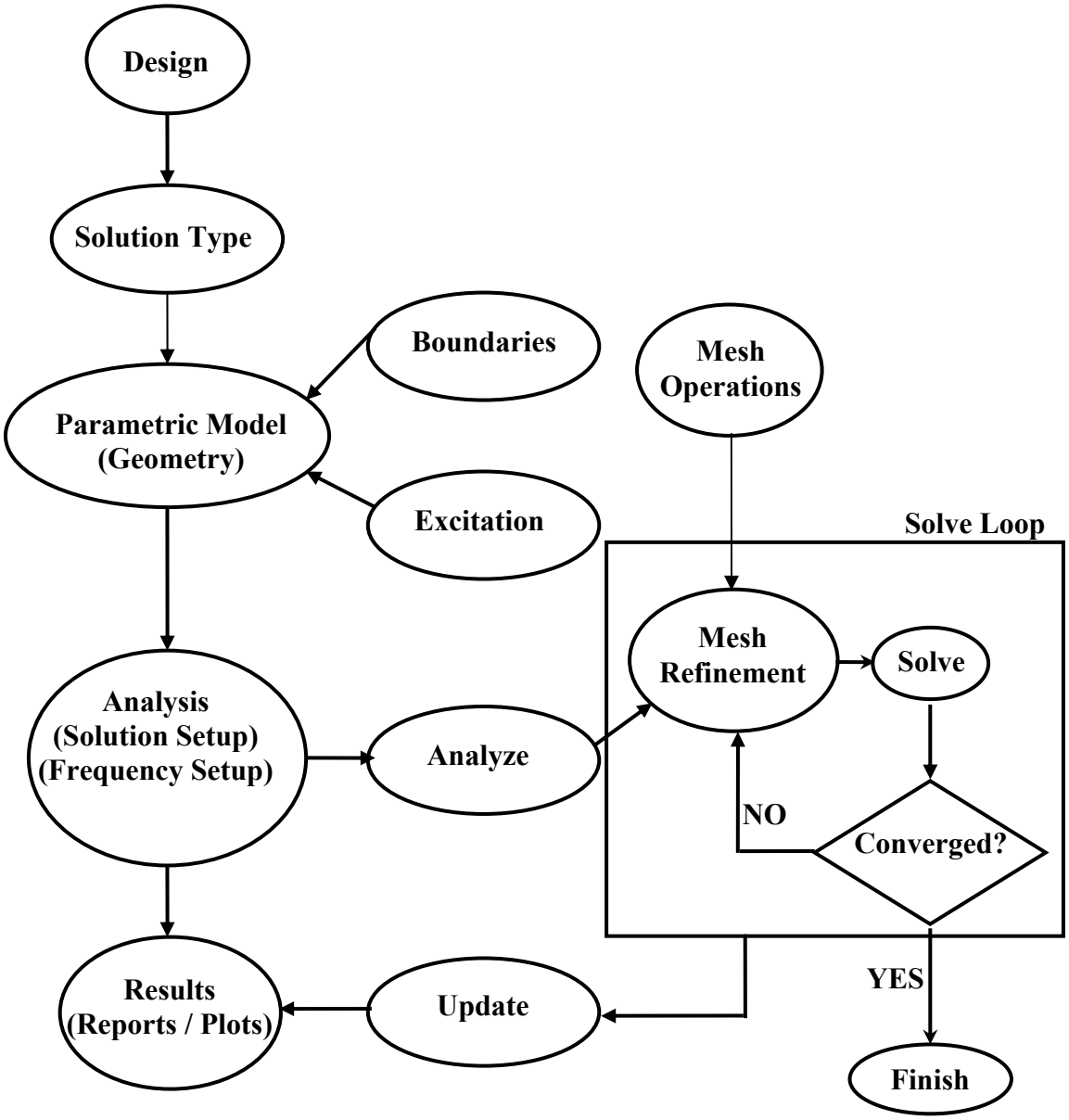

Fig. 4.1 Block diagram for the HFSS Simulator

4.2 Major building blocks of *HFSS*

Although *HFSS* can perform a wide variety of operations, in this section we discuss only those capabilities that we have utilized in this work. The Electromagnetic Wave Simulator, *HFSS*, is divided into the following important constituents. They also are the consecutive steps of a typical simulation process in *HFSS*.

4.2.1 Solution type

The solution type defines the type of results that we need, the way we define the excitations, and the convergence criterion. There are three different types of solution types, namely, driven-modal, driven-terminal, and eigen-mode. Driven-terminal type of solutions are used to calculate the terminal based S-*parameters* of passive, high frequency structures and the results are in terms of voltage and current wave components. Eigen-mode solver is used to calculate the resonances of the structure, i.e. the resonant frequencies and the associated fields of the structure. We have used driven-modal type of solutions in our analysis.

We use a monochromatic source of light in our experiments, and only one mode of the laser is excited. Hence, we use mode based solutions as it gives us the option to choose the number of modes present in the solution. This option allows us to calculate the mode-based *S-parameters* of passive, high frequency structures such as waveguides, micro-strips and transmission lines. The *S-parameters* generated are expressed in terms of incident and reflected components of the waveguide mode.

4.2.2 Boundary Conditions

The boundary conditions in *HFSS* enable the user to control the characteristics of planes, faces, or interfaces between the objects. These boundary conditions allow us to define the field behavior across the discontinuous boundaries of the structure under investigation. Since they force the field behavior according to our assumption towards the right solutions, we must be confident that they are completely appropriate for our simulations. Any improper use of boundary conditions might lead us to the inconsistent or inaccurate results. On the other hand, when boundary conditions are used properly, they help us reduce the model complexity. Assigning the boundary condition is extremely important.

When a geometric structure is defined for the simulations, unlike practical situations where the device under test is bounded by infinite space, *HFSS* automatically surrounds it by a *background* or *outer* boundary. This type of a boundary is also called as *Perfect-E* type, where the (background) material is a perfect conductor, and the boundary condition forces the field to be perpendicular to the surface of the conductor.

In case of *Perfect-H* boundary, the simulator forces the field to be tangential to the boundary surface.

A *finite-conductivity* boundary enables the user to define the surface of the geometric model as a lossy (*Imperfect-E*) conductor. A similar boundary is a *Lumped-RLC* type, which is a parallel combination of resistor, inductor and a capacitor.

A *radiation* or an *absorbing* boundary makes the model surface electrically open, i.e. the waves can radiate out and toward the radiation boundary. The system absorbs the wave to the radiation boundary, and effectively converts the model to be placed in infinite space.

When radiation boundaries are defined in the models, the *S-parameters* take into account the radiation losses.

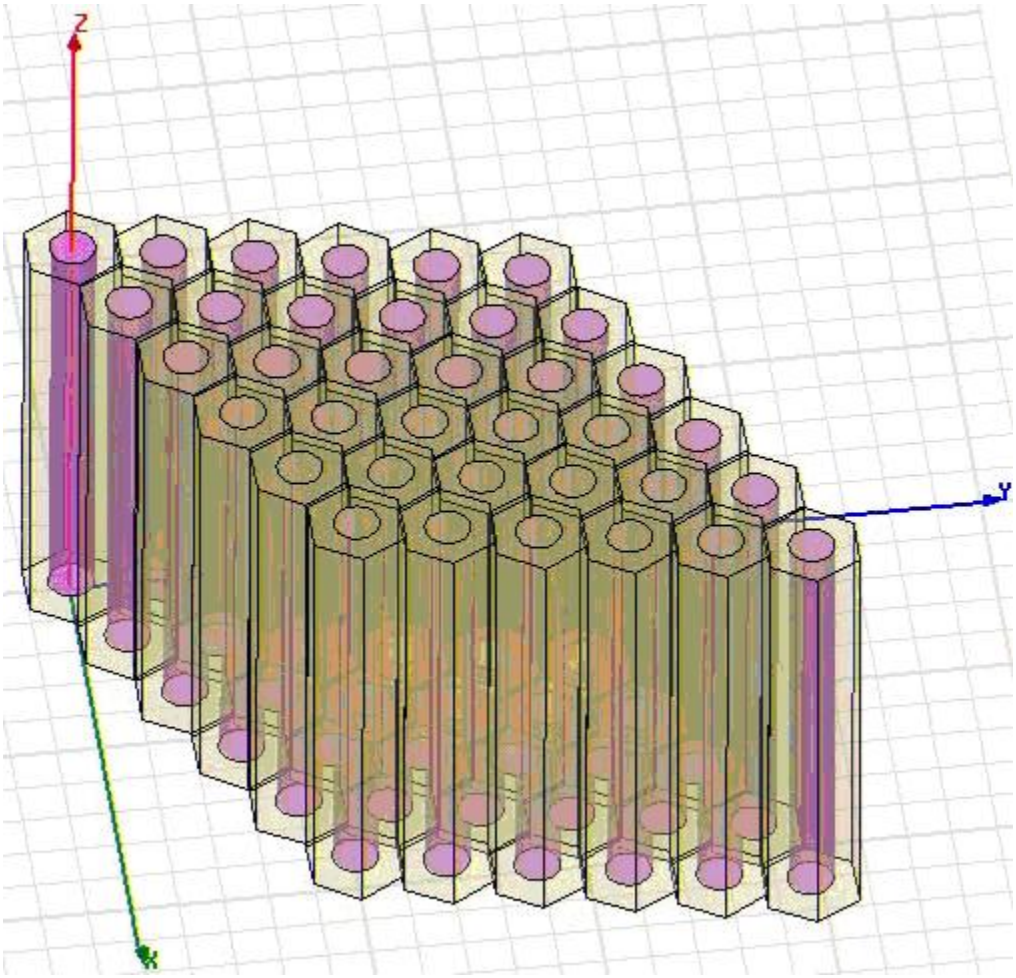

Fig. 4.2 A quantum wire array device: A periodic geometric structure

The most important and more relevant type for our purpose is the *Master-Slave* boundary conditions, which reduce the complexity of the structures with repetitious geometric

behavior. In our experiments, we use a quantum wire array device in which a cylindrical wire embedded in a hexagonally shaped alumina cell periodically repeats itself as shown in Fig. 4.2, and hence is a perfect fit for such boundaries.

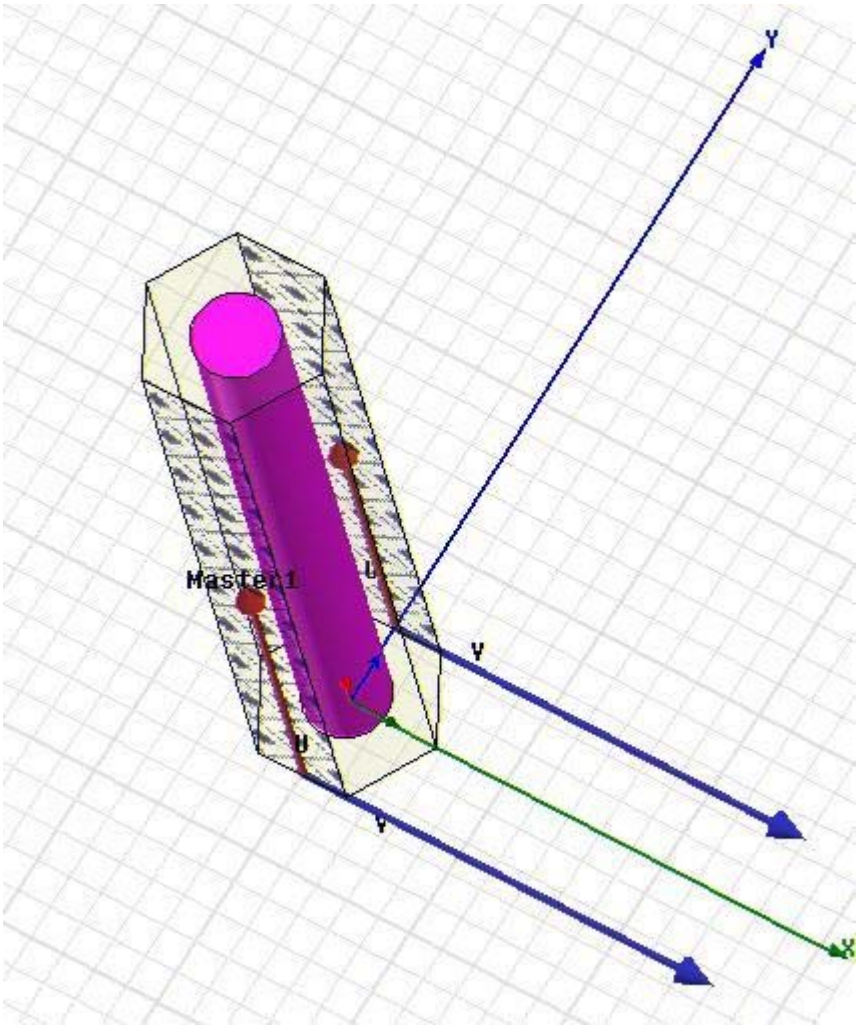

Fig 4.3 Master and Slave surfaces of a hexagonal unit cell

An electric field on a *Slave* surface is defined such that it follows electric field on the *Master* surface within a phase difference. When the surfaces of the geometric model under investigation are defined as *Masters* and their respective *Slaves* are also assigned,

the boundary condition forces the electric field at each point on the *Slave* surface to follow its corresponding *Master* surface.

There are certain constraints on a surface to be assigned a *Maste*r or a *Slave*. They must be plane surfaces. Curved surfaces cannot be assigned as a *Mater* or a *Slave*. Their geometries must also exactly match each other.

Fig. 4.3 describes the *Master-Slave* boundary conditions as they are applied to a hexagonal unit cell, where a cylindrical quantum wire is embedded in hexagonal alumina. There are two pairs of *Master-Slave* surfaces in a hexagonal unit cell. Two adjacent surfaces are first assigned to be *Master* surfaces, and the surfaces opposite to them are then assigned as the corresponding *Slave* for each *Master*. All the boundary surfaces are rectangular in shape, and their electric fields have the same magnitude and direction. Moreover, we do not introduce any phase delay between the *Master* and *Slave* boundaries so that the electric field distribution *Slave* surface exactly follows that on the *Master* surface. When one more unit cell is introduced into the system, *HFSS* places its opposite surface (*Slave* surface) such that it overlaps the *Master* surface of the first unit-cell. If there was only one pair of *Master-slave* boundaries (assigned to opposite faces) in a hexagonal unit cell, it would create a row of wires placed next to each other. But as there are two pairs of *Master-slave* boundaries, the repetition procedure leads us to create a 2-dimensional array of quantum wires. The model looks like the structure in Fig. 4.2, except that Fig. 4.2 shows only a limited number of unit cells. In the actual simulation, we have repeated the hexagonal unit cells so as to generate the structure of about 10×10

micron^2 in size. The details of a unit cell and the whole geometric structure are described in section 4.3 later.

4.2.3 Excitation

The excitation ports could also be categorized as a separate boundary condition itself, where the excitation (boundary) surface permits the energy to flow into and out of the device under investigation. A *2-dimensional* object or the face of a *3-dimensional* structure is generally assigned as an excitation port. The excitation-field-patterns at each port are to be calculated before *3D* electromagnetic fields inside the structure are determined.

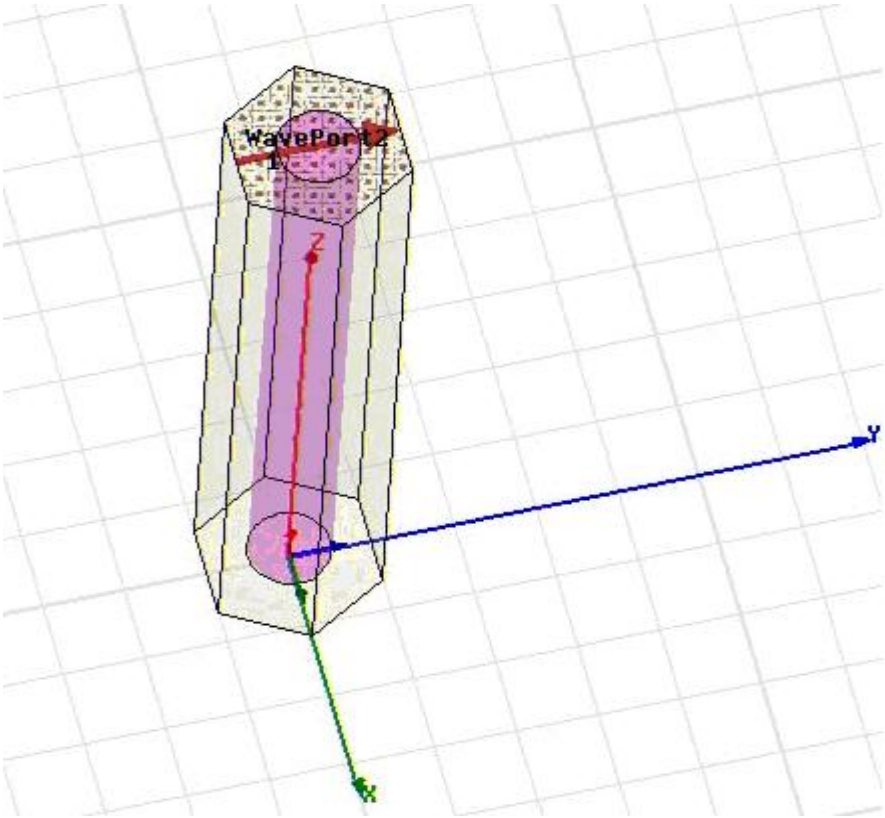

Fig. 4.4 Wave-port type of excitation

Wave-ports are defined on a surface to indicate the area where the energy enters and exits the *background*, or a default *outer* boundary. If *Lumped-ports* are used in the simulation, it is possible to model the internal ports within the structure. We have considered *Wave-port* type of excitation. That is the excitation surface is connected to a semi-infinitely long waveguide that has the same cross section and material properties as the port. Fig. 4.4 shows one of the two excitation ports that we have used for a hexagonal unit cell. The other port is located at the bottom of the cell. Each port is excited individually and each mode incident on the ports contains *1 mW* of time averaged power. However, we have used only one port for actual excitation, while the other remains the dummy port to allow the energy out of the structure. The *Wave-ports* calculate characteristic impedance, complex propagation constant, as well as the generalized *S-parameters*. As monochromatic light is used for wire excitation, we allow only a single mode to exist in the quantum wire structure, and hence all the simulations are performed for a single mode excitation.

4.2.4 Analysis, Solution Setup, Solve loop and Results

In order to perform an analysis in *HFSS*, a solution setup has to be added. The results are calculated at a pre-assigned solution frequency. As we use *IR* laser source at wavelength $\lambda = 1308\ nm$ (*frequency = 229.3578 THz*), it chosen as the solution frequency.

Unlike the processes of choosing the solution type, setting up the boundary conditions, the excitations and building the geometric model, the process of solution generation and

formation of the mesh is a highly automated one. There are several stages the simulator goes through before generating the final solutions, which include the generation of initial mesh and the solution, adaptive refinement loop and frequency sweep.

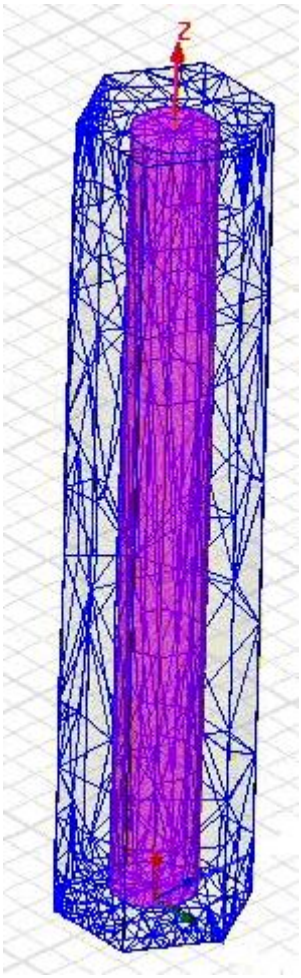

Fig. 4.5 Adaptive mesh generation

We choose an adaptive meshing criterion, so that the mesh is automatically tuned to generate a very accurate and efficient mesh in the structure. It generates more robust

meshing for complex geometries. The adaptive meshing is based on the excitation field. Hence the solution frequency of *228.3578 THz* is used to automatically refine the mesh to the electrical performance of the device. The initial mesh is set using a *Lambda-refinement* process, in which most element lengths are approximately one-third the wavelength for dielectrics. A wavelength is already set when we define the Single *Solution-Frequency* value.

Adaptive meshing makes it extremely easy to generate the most accurate and efficient mesh possible. Fig. 4.5 displays the mesh generated in the hexagonal unit cell using the adaptive meshing criterion. Without this option, the process of generating the correct mesh would be extremely tedious and prone to errors. The adaptive meshing algorithm searches for the largest gradients in the electric field or error, and sub-divides the mesh in those regions. The mesh grown for every adaptive pass is controlled by the tetrahedron refinement given as a percentage, which ensures that between each pass, the mesh is sufficiently perturbed and there won't be any false convergence. We use *20%* tetrahedron refinement per adaptive pass. After the mesh is refined, a full solution is performed and the process is repeated until convergence. As *S-parameters* are extremely important in our calculations, the convergence criterion is based on the *S-Matrix*. After each adaptive pass, the *S-parameters* in the current mesh are compared with those of the previous mesh. The solution is assumed to have converged, when the answer in two consecutive passes has changed by a value smaller than the pre-defined value of ΔS. This value of ΔS is defined as the maximum change in the magnitude of *S-parameters* between two consecutive passes. As it is a magnitude of a vector quantity, ΔS can between *0* and *2*. If

the convergence is reached, this technically means that the previous mesh is as good as the current mesh. All manufacturing processes have inherent errors associated with them, as well as the laboratory equipments, and the measurement processes. We should not expect the simulator to provide an accuracy which is much more than what we get in the real world. Hence, we have used ΔS value to be 0.02 which we believe represents a sufficiently good accuracy. The mesh for each port is also adaptively refined.

The solutions are then generated at a solution frequency of $229.3578\ THz$ during each adaptive pass. We have set a limit of maximum nine passes to achieve convergence. We have set a minimum limit of three adaptive passes, even though the convergence criterion is already achieved. It is also possible to generate the solutions for a wide frequency band using a frequency sweep criterion. However, we haven't used the option as we need the solutions at a single solution frequency. Final values of *S-parameters* are then retrieved from the results section, to generate the phase delay generated as the wave passes through the quantum wire array.

4.3 Geometric Model of the quantum wire array

As we had explained in previous chapters, a 2-dimensional quantum wire array is formed by selective electro-deposition of the semiconductor material into the pores of a nano-porous alumina template. The pores and hence the quantum wires are uniformly spread across the alumina and the structure possess an extremely regular geometry. Moreover, the wires are of fairly uniform cross-section (diameter) and the inter-pore separation

remains constant over the whole template. As we mentioned in the previous chapters, various parameters decide the diameter and depth of the nano-pores formed in the alumina templates, which include the type and concentration of the anodizing acids, as well as the anodizing voltage. *3%* of oxalic acid, and a *40 V dc* anodizing voltage produces *50 nm* diameter pores, while the anodizing voltage of *25 V dc* produces *25 nm* pores. For *10 nm* diameter pores, *15 %* of sulfuric acid is used at *10V dc* voltage. The wire diameter and inter-pore separation for the electrochemically self-assembled quantum wire array structures fabricated using the above parameters are displayed in Table 7.

Wire diameter (nm)	**Inter-pore separation (nm)**
50	**100**
25	**80**
10	**60**

Table 7 Wire diameter and inter-pore separation

Hence, in HFSS, we have modeled a structure such that the quantum wires of identical diameters and lengths, are embedded in alumina and separated by equal distances. Moreover, the *AFM* and *SEM* images show that each wire is surrounded by six different wires as shown in Fig. 4.6.

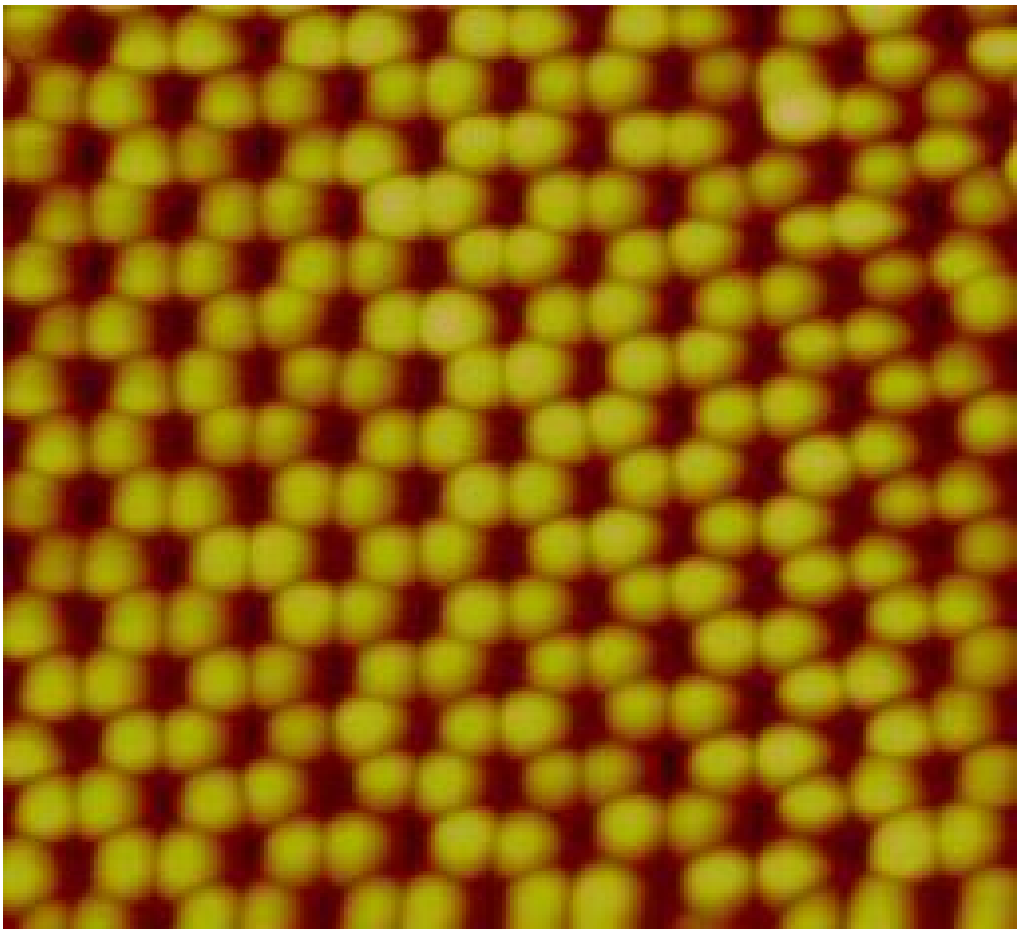

Fig. 4.6 *SEM* image of quantum wires of *50-nm* diameter. The black spots indicate the quantum wires

The actual films that we have used in the experiments are about *6-7 mm* in diameter. We also have to consider the fact that our collimated *IR* laser beam is about *2.2 mm* in diameter. Hence even if we consider the area of 2.2 mm diameter of the quantum wire array, we have "sampled" about 1-5 million nano-wires in our experiments. Modeling this big array is completely impossible, if we plan to consider all the wires in the simulation structure. The complexity of the model would be drastically reduced by using a number of alternatives. First of them would be to consider a smaller area of the film. If

we consider the area of just *10×10 micron*^{2}, we still account for sizable amount of quantum wires to make a valid simulation. Moreover, as *10 micron >> 100nm* (the inter-pore separation) and also much larger than the involved light wavelength of *1.308 microns*, the area taken into account is a good approximation for the simulation. Secondly, rather than considering a *2D*-array in a single simulation, we can model a unit cell and replicate it with required periodicity so as to generate the array structure identical to the actual quantum wire array.

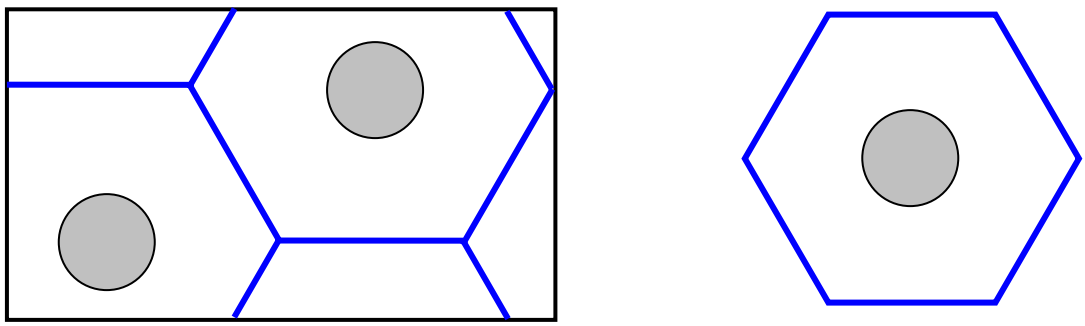

a) Rectangular unit cell **a) Hexagonal unit cell**

Fig. 4.7 Unit cells that would generate a quantum wire array when placed with a specific periodicity

Fig 4.7 shows two of the unit cells, which would generate the desired quantum wire array structure as shown in Fig. 4.6, when reproduced with a particular periodicity. The grey circles represent the quantum wires, while the white hexagon represents the surrounding alumina in which they are embedded. The quantum wire array formed using both the type

of unit cells are shown in Fig 4.8. The rectangular unit cell has a simpler structure, as far as the application of the *Master-Slave* boundary conditions are concerned, as both the pairs of opposite faces are simply required to follow each other in order to generate the desired quantum wire array.

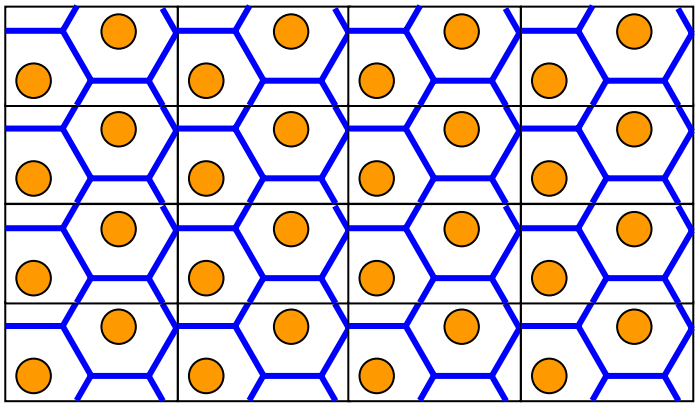

a) Rectangular unit cell geometry

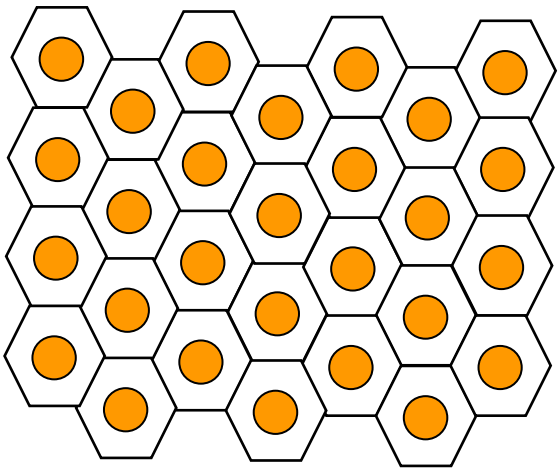

b) Hexagonal unit cell geometry

Fig. 4.8 The quantum wire array formed using rectangular and hexagonal unit cells

However, as the rectangular unit cell contains two (cylindrical) wires, more curvatures are included in the model, hence requires a much denser mesh. Moreover, for quantum wires of *50 nm* diameter, the edge of one of the wires (lower one in the rectangular unit cell) becomes extremely close to the lower boundary of the unit cell, which further makes the mesh denser. This effectively increases the simulation time and slows down the convergence. On the other hand, two pairs of opposite faces are required as *Master-Slave* pairs in case of hexagonal unit cell. One hexagonal unit cell represents one wire. A 2-dimensional array structure is obtained as both *Slave* boundaries follow their respective *Masters*. As fewer curvatures are involved, the processing time reduces, and convergence is faster. Although both the unit cells give very similar results, we have used the hexagonal unit cells in our simulations for faster processing time and more importantly for easier convergence.

4.4 Final Simulations for the quantum wire array

As described in the earlier sections, we have modeled a quantum wire array structure with a periodic placement of the hexagonal unit cell structures, using *Master-Slave* boundary conditions. A $10 \times 10\ micron^2$ area of the quantum wire array is considered for the simulation. A single unit cell consists of a cylindrical quantum wire, embedded in a hexagonal cylinder shaped alumina, as shown in Fig. 4.2-4.4. Each quantum wire is *1 micron* in length. The wires are excited by a single mode *1308 nm* light source using *Wave-port* type of excitation. The *Wave-ports* are located on the hexagonal faces of

alumina unit cell as shown in Fig. 4.4. Simulations are performed for wires of four different types of *III-V* group semiconductor materials, namely *CdS / ZnSe / ZnO / CdSe*. These optical constants for a single wire have already been calculated and presented in Chapter 3. The dielectric constants (permittivity) calculated for the quantum wires of the semiconductor materials are incorporated in the simulations here. The real part of dielectric constants (ε'), along with the loss tangents for all the quantum wire materials are reproduced in Table 8. These two values calculated from the theoretical models described in chapter 3 are incorporated in HFSS to retrieve the phase shift induced by the quantum wire array.

Wire Material	***50 nm***		***25 nm***		***10 nm***	
	Re(Dielectric Constant)	***Loss tangent (× 10^{-3})***	***Re(Dielectric Constant)***	***Loss tangent (× 10^{-3})***	***Re(Dielectric Constant)***	***Loss tangent (× 10^{-3})***
CdS	***5.389569828***	***0.63***	***5.354838769***	***0.626***	***5.12310009***	***0.616***
ZnSe	***6.020206432***	***0.495***	***5.98113021***	***0.492***	***5.720172431***	***0.472***
ZnO	***3.726365031***	***0.597***	***3.715059233***	***0.595***	***3.637877249***	***0.580***
CdSe	***6.229445099***	***0.796***	***6.135948167***	***0.784***	***5.549478957***	***0.705***

Table 8 Real part of permittivity (ε') and dielectric loss tangent values calculated using *Mathematica* for unexcited quantum wires and utilized as an important material parameter in *HFSS.*

We also need an accurate value of the alumina in which the wires are grown. The published values of porous alumina indicate its permittivity to be *3* at $\lambda = 1308\ nm$ [107]. Thompson *et al.* have performed an optical characterization of the porous alumina [108] and they came up with the permittivity values which are slightly on the higher side than those indicated in [107]. The alumina used in the studies performed in [108] is fabricated using the same procedure with which our porous alumina structures were fabricated. Similar results are reported by Kooij *et al.* in [109]. The higher permittivity values in alumina reported in [108] and [109] are attributed to the *28*% nano-porosity caused by extremely small scale voids present inside the solid fraction of the alumina materials [108]. Note here that, this value of permittivity (≈ 3) is for porous alumina. This means that in place of each quantum wire, these models in [107]-[109] have considered air (or vacuum) as the effective filling material. But in *HFSS*, we require bulk permittivity values of alumina, as the quantum wires are surrounded by bulk alumina. Hence, the permittivity for bulk alumina is chosen to be *8.6* as given in [107]. Note here that alumina remains completely transparent to *IR* and *UV* wavelengths of our interest.

The above permittivity values for the quantum wire semiconductor materials as well as for alumina are used as the material parameters while modeling the unit cells in *HFSS*. The simulation is designed to calculate the phase shifts incurred by the light wave as it passes through the quantum wire array. When the array is *excited by UV* at the wavelength *365 nm*, a number of electron hole pairs are generated. This effectively changes the optical behavior of the quantum wire array. In our experiments, we measure the changes in phase shift as the *UV* excitation pulses are applied. However, we do not

indicate the *UV* excitation anywhere in the *HFSS* simulations. The presence of the *UV* pump has been accounted for in the simulations, by changing the permittivity of the quantum wire dielectric material as determined by the experiments. During the experimental procedures, we measure the changes in phase shifts (*in ppm*) induced by the quantum wire samples as the *UV* pump is applied. We note these phase shift changes for six different *UV* intensities, for quantum wires of three different diameters (*50 / 25 / 10 nm*), and for four different types of materials (*CdS / ZnSe / ZnO / CdSe*). Four samples of each type of the array are tested. Then, in the simulator, the permittivity values of the individual quantum wires (of same diameter and fabricated using the very same semiconductor material as that used in the corresponding experiment) are adjusted iteratively, so as to obtain the same changes in phase shifts that we measured experimentally.

	50 nm	***25 nm***	***10 nm***
CdS	***-59.98939609***	***-78.82589711***	***-97.31653501***
ZnSe	***-67.72140152***	***-86.59647189***	***-98.56166773***
ZnO	***-40.26385781***	***-65.28188918***	***-95.601994***
CdSe	***-72.292162***	***-52.213521***	***-94.669026***

Table 9 Phase shift of the probe wave (1308 nm) as it passes through the unpumped quantum wire array, as calculated in *HFSS*

Hence, using *HFSS*, we basically perform the same experiment that we performed on the optical table, but in a simulation environment. To correlate the experimental results with the simulations, phase shifts observed in the experiments due to *UV* excitations are treated as the matching parameters. In this chapter, we only include the data (Table 9) that shows these phase shifts of the *IR* wave due to each type and diameter of quantum wires, as calculated in *HFSS*. The phase shift changes between pumped and unpumped arrays and the relevant discussions are given in the Chapter 6.

CHAPTER 5

Experimental Analysis

We have built a Michelson interferometer in a homodyne setup to investigate the optical response of an electrochemically self-assembled quantum wire array to a stationary excitation using a pump-probe excitation scheme. An interferometer is extremely sensitive to the variations in the optical behavior of the device under test. The interferometer is constructed using a *1308-nm* probe *IR* laser, and a *365-nm UV LED* pump. In this chapter, we explain the theoretical basis for our experimental setup, as well as prove the validity of the experiments.

5.1 Theoretical basis for the experiment

As discussed in Section 2.4 on *Interference*, the phenomenon of interference works on the principle of superposition of two coherent waves. Rewriting equation (2.14), where P is considered the superposition of two waves of amplitudes P_1 and P_2,

$$P = P_1 + P_2 + 2\sqrt{P_1 P_2}\,Cos(\Delta\varphi) \tag{5.1}$$

where $\Delta\varphi$ represents the phase difference between the two waves. The phase difference is, in turn, dependent on the difference in the path lengths of the two waves. The equation for phase difference is written as

$$\Delta\varphi = \left(\frac{2\pi}{\lambda}\right)\Delta d = \left(\frac{2\pi n}{\lambda_0}\right)\Delta d \tag{5.2}$$

Although the above equation shows that the phase difference changes with the difference in path lengths, it simultaneously is also a function of wavelength λ and the refractive index n of the medium the light passes through.

In our experimental setup, we place the device under test (quantum wire array) in one of the branches of the interferometer. When excited by the *UV* light, the optical behavior of the array changes due to the generation of *electron-hole* pairs. Hence, this external perturbation effectively changes the optical properties of the quantum wire array. Irrespective of the cause which actually changed the array behavior, the amplitude and the phase of the probe beam passing through that branch of the interferometer changes. If we consider that P_{20} is the initial wave amplitude, and $\Delta\varphi_0$ is its initial phase (pre *UV* excitation state), final amplitude P_2 and phase difference $\Delta\varphi$ of the wave (post *UV* excitation state) are given as

$$P_2 = P_{20} + \delta P_2(t) \tag{5.3-A}$$

$$\Delta\varphi = \Delta\varphi_0 + \delta\varphi(t) \tag{5.3-B}$$

Although, it is quite difficult to distinctly separate the parameters which directly modify the amplitude and phase of the wave passing through the quantum wire array when optically perturbed, changes in amplitude $\delta P_2(t)$ could be attributed to the change in

absorption coefficient of the array, while change in the phase shift $\delta\varphi(t)$ is attributed to the change in its refractive index.

Using equation (5.1) and (5.3), we get

$$P = P_1 + P_{20} + \delta P_2(t) + 2\sqrt{P_1(P_{20} + \delta P_2(t))}Cos(\Delta\varphi_0 + \delta\varphi(t))$$

The term in the square root is simplified using binomial approximation as $\sqrt{P_1 P_{20}}\left(1 + \frac{1}{2}\frac{\delta P_2(t)}{P_{20}}\right)$.

Furthermore, using the expansion $Cos(A+B) = Cos(A)Cos(B) - Sin(A)Sin(B)$, the *Cosine* term in the above equation is simplified to $Cos(\Delta\varphi_0) - Sin(\Delta\varphi_0)\delta\varphi(t)$, with an assumption that the change in the phase difference $\delta\varphi(t)$ is extremely small. Hence, $Cos[\delta\varphi(t)] \rightarrow 1$, while $Sin[\delta\varphi(t)] \rightarrow \delta\varphi(t)$.

The change in the amplitude of the wave due to perturbation, $\delta P_2(t)$, is related to the change in absorption of the quantum wire array due to *UV* excitation. Absorption by the quantum wire array is directly proportional to the length of the quantum wires. But, as the wire length is just *1 micron*, the term $\delta P_2(t)$ is extremely small. We must also consider the fact that the quantum wires are embedded in the porous alumina templates. This alumina, being a very wide band-gap material, remains completely transparent to the *UV* excitation that we have used. Hence, only the quantum wire semiconductor material, limited to the pores of the alumina structures, is actually responsible for any absorption. But the filling factor of this quantum wire array structure, which is defined as the ratio of the volume of the quantum wire to the volume of the surrounding alumina unit cell as discussed in the previous chapter, remains much smaller than unity. Hence, although the

complete array is excited by *UV* light, only a small portion of that, depending on the filling factor, is responsible for actual absorption.

Hence, the interference equation becomes

$$P = P_1 + P_{20} + \delta P_2(t) + 2\sqrt{P_1 P_{20}} \times [Cos(\Delta\varphi_0) - Sin(\Delta\varphi_0)\delta\varphi(t) + \frac{1}{2}\frac{\delta P_2(t)}{P_{20}}Cos(\Delta\varphi_0) - \frac{Sin(\Delta\varphi_0)}{2P_{20}}\delta P_2(t)\delta\varphi(t)] \quad (5.4)$$

In the above equation, there are two different types of terms. First category belongs purely to the constant or *DC* terms (P_1, P_{20},and $\Delta\varphi_0$), which are independent of any external perturbation, a *UV* excitation in our case. On the other hand, perturbation or time-dependent terms ($\delta P_2(t)$ and $\delta\varphi(t)$) form the second category. These terms wouldn't exist if there were no external perturbation, i.e. if there were no change in optical behavior of the quantum wire array.

If the external perturbation is alternating in nature, all the *DC* terms in the above equation could be filtered out. Moreover, if the 2nd order small terms [containing $\delta P_2(t) \times \delta\varphi(t)$] are neglected, the alternating or perturbation affected terms $P(t)$ are written as

$$P(t) = \delta P_2(t) - 2\sqrt{P_1 P_{20}}Sin(\Delta\varphi_0)\delta\varphi(t) + \sqrt{\frac{P_1}{P_{20}}}Cos(\Delta\varphi_0)\delta P_2(t) \quad (5.5)$$

$P(t)$ is referred as the *ac* component of the interference waveform. Due to the direct dependence of the change in the wave amplitude on the wire length, as well as on the filling factor, the term $\delta P_2(t)$ in equation (5.5) is extremely small. This also effectively makes $P_1 \approx P_{20}$. If we adjust the initial phase difference $\Delta\varphi_0$ between the two interfering waves to be $\pi/2$, $Cos(\Delta\varphi_0) \rightarrow 0$, while $Sin(\Delta\varphi_0) \rightarrow 1$.

Under this condition, the *ac* component of the interference equation reduces to

$$P(t) = \left(-2\sqrt{P_1 P_2}\right)\delta\varphi(t) \tag{5.6}$$

The term in the bracket is the noiseless-optical-gain of the system. Note here that $\delta\varphi(t)$ is proportional to the change in index of refraction of the device under test due to *UV* excitation.

According to *Kramers-Kronig* relation, for any time-invariant linear passive system, the real part of its frequency response function is related to its imaginary part and vice versa. Hence, as explained in chapter 2, as the refractive index of the material changes, due to the photo-generated *e-h* pairs, it also causes a change in the absorption coefficient of the sample. Accordingly, as the sample is excited by a *UV* pulse, that not only changes the path difference of the beams on account of a change in refractive index of the sample, but it also changes the amplitude (intensity) of the beam passing through the sample. But the overall absorption remains very small due to its direct dependence on the extremely short length of the quantum wires, as well as on the very small filling factor of the quantum wires in the array. Therefore, the change in the intensity $\delta P_2(t)$ of the beam passing through the array is expected to be too small to be detected by the receiver. On the other hand, the change in the refractive index is magnified due to the presence of the small optical wavelength term in the equation denominator, which we have discussed in section 5.2. Thus, all our experiments are aimed at measuring the changes in the phase difference of the two waves when excited by stationary *UV* light.

5.2 Effective amplification of the change in the phase-difference

Consider two light waves, traveling through distances L_1 and L_2, are superimposed at a point *B* as shown in Fig. 5.1. Consider an optically active material of length *l*, or a device under test (*DUT*), is placed in one of the beam paths. Suppose that the refractive index of the surrounding medium is n_1, while the refractive index of the device under test is n_{20}.

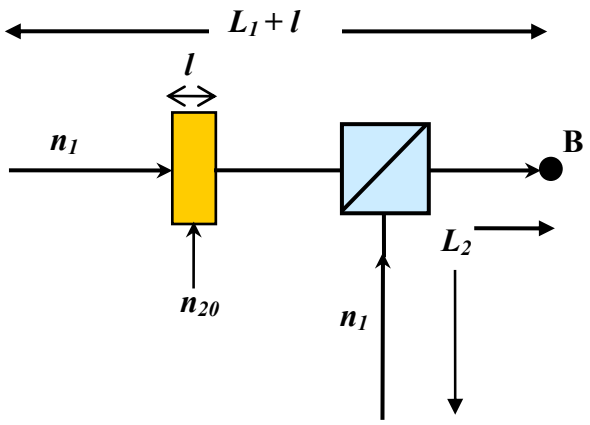

Fig. 5.1 The interference situation

For the situation when no external perturbation is present, using equation (5.2), the total phase difference between the two interfering waves at point *B* is

$$\Delta\varphi_0 = \frac{2\pi}{\lambda}\left[\left(n_1 L_1 + n_{20} l\right) - n_1 L_2\right]$$

$$= \frac{2\pi}{\lambda}\left[n_1\left(L_1 - L_2\right) + n_{20} l\right] \tag{5.7}$$

When the device under test (quantum wire array) is excited by *UV* light, depending on the

intensity of the light used, there would be small changes in its refractive index n_{20}. Suppose that the refractive index changes to n_2 are

$$n_2 = n_{20} + \delta n_2(t) \tag{5.8}$$

A small change $\delta n_2(t)$ in the refractive index leads to a change in the phase difference. Hence the phase difference in the perturbed state is given as

$$\Delta\varphi = \frac{2\pi}{\lambda}\left[n_1(L_1 - L_2) + n_{20}l\right] + \frac{2\pi}{\lambda} \times l \times \delta n_2(t) \tag{5.9}$$

The first term in the above equation (5.9) is the initial phase difference $\Delta\varphi_0$ as shown in equation (5.7), while the second term is attributed to the change in the phase difference $\delta\varphi(t)$ due to the excitation by *UV* light, as given in equation (5.3-B). It is an extremely important term for our calculations and the experiment. Thus,

$$\delta\varphi(t) = \frac{2\pi}{\lambda} \times l \times \delta n_2(t) \tag{5.10}$$

As mentioned previously, the initial phase difference $\Delta\varphi_0$ can be adjusted by properly biasing the interferometer to $\Delta\varphi_0 = \pi / 2$. Hence, using equation (5.6), the *ac* component of the interference equation becomes

$$P(t) = 2\sqrt{P_1 P_{20}}\left(\frac{2\pi}{\lambda}\right) \times l \times \delta n_2(t) \tag{5.11}$$

We can observe in equation (5.11) that the *ac* component of the interference equation, or more precisely, the component of the interference equation which depends on the *UV* excitation of the quantum wire array is directly proportional to initial amplitudes P_1 and P_{20} of the two waves, as well as the length l of the quantum wires and the change in the index of refraction $\delta n_2(t)$.

This *ac* component of the interference equation is the most important term for our experiments, which we intend to measure. But, as the length of the wires is just about *1 micron* (1×10^{-6}), the *ac* component is also expected to be very small. However, it also has an inverse dependence on the wavelength λ of light, where $\lambda = 1308nm$. Hence, a small wavelength in the denominator acts as an amplification factor, which strengthens the possibility that the *ac* component becomes sufficiently large to measure. We plan to experimentally measure the change in phase (path) difference between the two waves, which in turn is proportional to the refractive index of the material. Therefore, as λ is located in the denominator, the extremely small changes in the refractive index of the quantum wire array are amplified when excited by *UV* light, and are sufficiently large to measure.

If we consider the *IR* light at $\lambda = 1308nm$ with individual beam amplitudes of *1 mW*, and quantum wire of length 1 micron, a change of *1 ppm* (parts per million) in the refractive index of the wire produces an *ac* component of the order of $9.6\times10^{-9}W$. We have used a Large-area- photodetector, which has a responsivity *R* of *0.66 A/W* at *1308 nm*, and a Gain *G* of 10^5 *V/A* (at a medium gain setting that we have used), and output voltage of the detector is given as $V_{out} = R\times G\times P$. This should produce a voltage of about *0.63 mV* at the detector output, which is sufficiently large to measure when a proper amplification circuit is used. However, at the (medium) gain setting of 10^5 *V/A*, the detector saturates approximately at a power just less than 1 *mW*. Hence, the interferometer, where the maximum output power can be about four times the individual beam powers, would definitely saturate the detector if the individual beam power is of the order of *1 mW*.

Hence, we introduce a neutral density (ND) filter to reduce the input power, which further suppresses the output voltage produced by the detector. Hence, we expected the output voltages of the order of few tens of *microV* to be detected experimentally, for a *ppm* (parts per million) level change in the refractive index of the device under test. The complete setup is explained in section 5.4 in detail.

5.3 Initial biasing of the interferometer

As mentioned previously, we have built a Michelson interferometer as a homodyne setup, to investigate the optical behavior of the quantum wire array to a stationary *UV* excitation using a pump-probe excitation scheme. As shown in Fig. 5.2, the interferometer works on the principle of amplitude splitting. The incoming wave is split into two waves using a beam-splitter, travels unequal distances and gets reflected by a set of mirrors. The waves then recombine via the same beam-splitter to form an interference pattern. Intensity of the interference pattern varies between certain minima and maxima, which are functions of the individual beam intensities and their path difference as in equation (5.1).

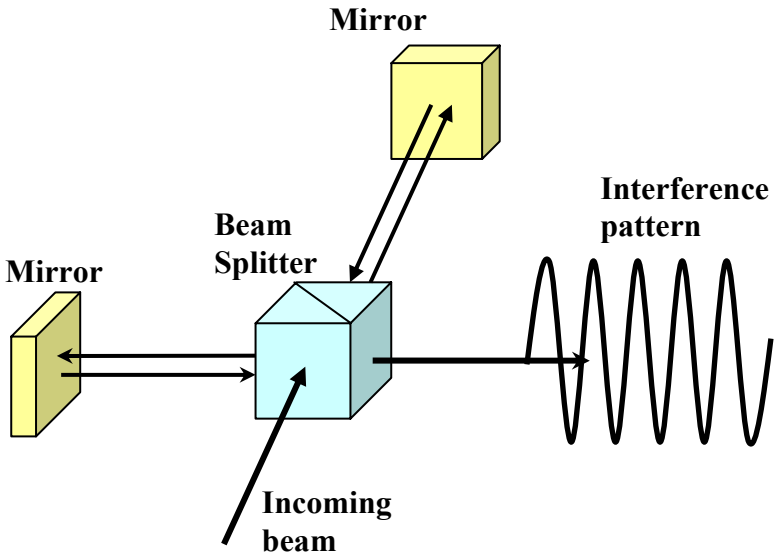

Fig. 5.2 Michelson Interferometer

According to the interference equation (5.1), when two waves of equal amplitudes (or intensities) superimpose to form an interference pattern, the intensity of the observed interference fringes vary from zero to four times the intensity of the individual waves, depending on the path difference of the individual waves. If the path difference is a multiple of the wavelength of light, constructive interference is observed. On the other hand, if the path difference is an odd multiple of half the wavelength, a destructive interference occurs.

One of the mirrors in the interference setup is mounted on a precision steel translation stage, which allows us to control its path length and eventually the interference. As the position of the mirror changes, the difference in wave path lengths also changes the intensity of the interference.

It is very important that, before the quantum wire array is excited by *UV* light, the path difference between the two beams is adjusted such that the system is biased halfway between the maxima and minima of the interference signal detected by the photodetector, as shown in Fig. 5.3.

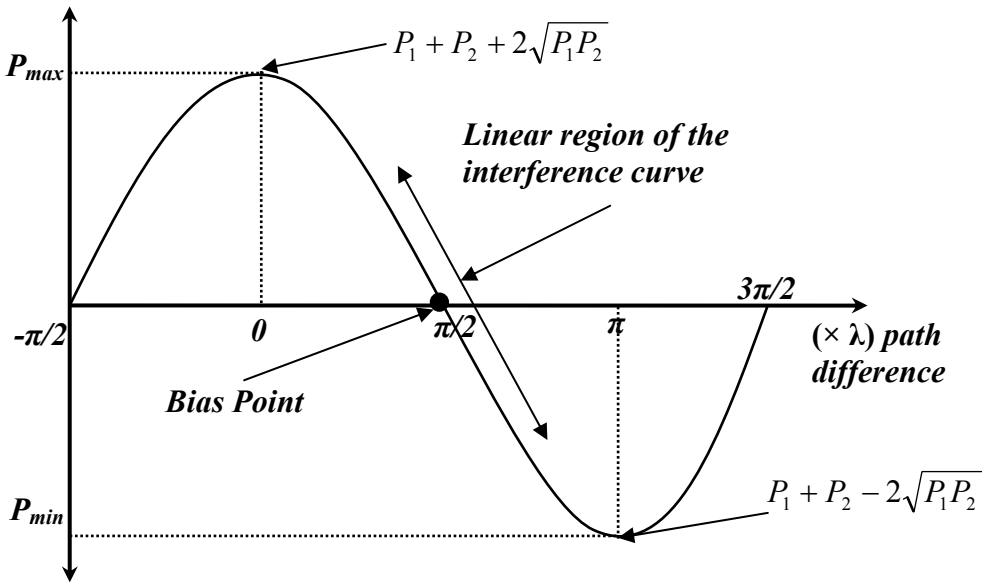

Fig. 5.3 Bias point on the interference curve

Hence, the bias point corresponds to the path-difference equal to the odd multiple of half the wavelength. The interferometer is biased at this particular point for two reasons.

1) This region between the minima and maxima of the interference curve has a maximum slope. Therefore the interferometer is most sensitive to the changes in phase difference when biased half way between the minima and maxima. As we move towards the extremes of the interference curve, its slope reduces, so does the sensitivity of the interferometer.

2) The interference curve is linear around this point. Hence, we expect the bias point to remain within this (linear) region of constant slope of the interference curve, while the system is excited with UV pump pulses. Therefore, any small changes in the phase difference are linearly amplified into the corresponding voltage signals.

To maintain an authentic control over the bias point, one of the mirrors is mounted on a steel precision stage with *20*-nm accurate adjustment. The entire interferometer is mounted on a vibration-isolated breadboard.

5.4 Experimental Setup

As we mentioned previously, an interferometer is extremely sensitive to any small changes in the path-difference between the two beams, which is reflected in terms of the intensity of the interference pattern observed at a point in space. When a device under test is introduced in one of its beam paths, the interferometer could be used to track any changes in its optical behavior. We build the experimental setup to investigate the optical behavior of the quantum wire array sample. The array is formed by selectively depositing the semiconductor material into porous alumina films. The light utilized to excite the quantum wires belong to a frequency band such that it interacts with the wire material, while the surrounding alumina remains transparent to it. We have used *UV* light pump at *365 nm* to excite the array. The interferometer is constructed using a *1308 nm* probe laser beam, to which the alumina as well as the semiconductor wire material is transparent. We

have manipulated a pump-probe excitation scheme in Michelson's interferometric setup, as shown in Fig. 5.4.

We worked on two alternate experimental setups before choosing the Michelson interferometer, namely a Fabry-Perot setup and Mach-Zender interferometer. A Fabry-Perot interferometer is a classic multiple pass (resonant) setup, where the beam passes through the cavity many times. Hence, if the sample is kept in the cavity of the Fabry-Perot etalon, we can obtain better sensitivity and any small changes in the absorption or refractive index could be easily detected at the photo detector. But in this setup, we encountered difficulty on account of certain confocal mirror sensitivity and stability issues. We also worked on an all-fiber-coupled Mach-Zender interferometer in a homodyne setup. This was a very compact setup due to its polarization maintaining fiber-coupled branches, but we had to abandon this novel concept on account of its fiber-air-fiber coupling instability due to polarization launch issues.

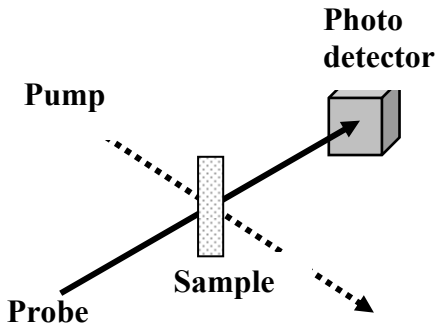

Fig. 5.4 Pump-probe excitation scheme

We have implemented a pump-probe excitation scheme in a Michelson interferometer. As shown in Fig. 5.4, a *probe* laser prepares the system to detect the optical response for the device under test (*DUT*). In our case, as the probe is a part of an interferometer, it picks up extremely minuscule changes in the optical behavior of the *DUT*. The *pump* laser is used to induce the optical changes in the device. These changes are detected by the photodetector in terms of the variation caused in the *probe* signal. We use *IR* laser as a *probe*, while *UV* light is used as a *pump* signal.

Fig. 5.5 shows the complete optical setup that we constructed for our experiments. We have used a *New-Focus* tunable IR laser (*1260-1370 nm*) at *1308 nm* as a probe signal for the quantum wire array. The *IR* laser is fed into the system via a *collimator lens* by *OZ-Optics* (*model HPUCO-23-1300/1550-P-11AS*), which takes the rapidly diverging beam from the fiber exit of the tunable laser, and straightens (collimates) it. The diameter of the collimated beam is approximately *2.2 mm*. The quantum wire array is located in one of the branches of the Michelson interferometer. Hence, the sample is continuously probed by the *IR* laser. The output of the interferometer is focused on the *New Focus Large-Area-IR-Photo-receiver* (*New Focus model 2033*). It has a *5 mm* diameter germanium *PN* photodetector. It operates in a wavelength range of *800-1750 nm,* while it is able to detect powers as low as few *nanoW* to a maximum of *3-4 mW*. As we mentioned previously, it has a responsivity of *0.66 A/W* at *1310 nm* and we operate it at a medium Gain setting of 10^5 *V/A*.

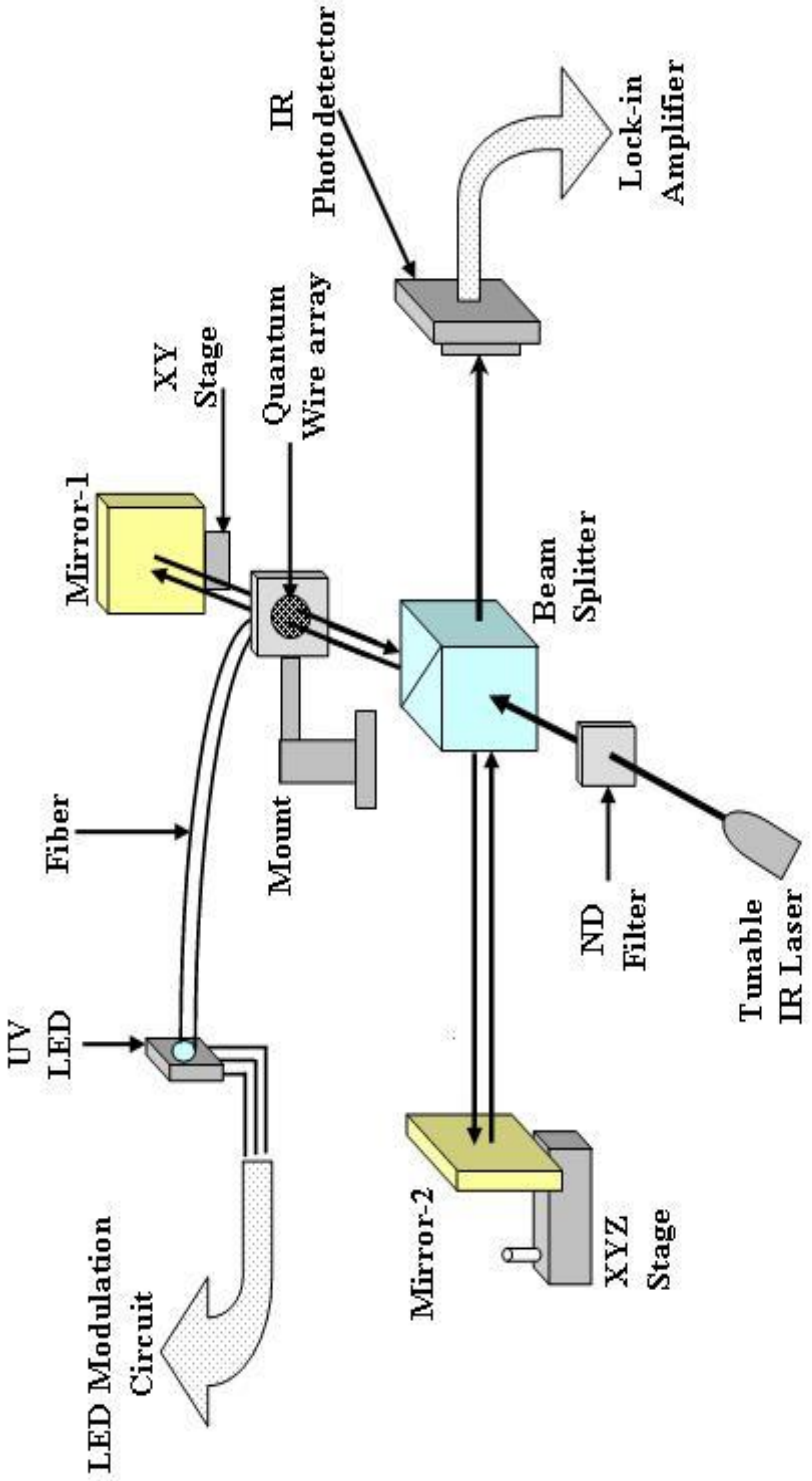

Fig. 5.5 Experimental setup

Fig. 5.5 Experimental Setup

To avoid the surrounding light getting into the detector and generating erroneous output voltages, the *IR* laser is fed through an aperture mounted on the detector. The aperture has a *3 mm* diameter. As the probe is a *CW IR* laser, the intensity of the light seen by the detector remains constant, producing a *DC* voltage at its output. *A 1.0 OD* (*10% transmission*) neutral density (*ND*) filter is installed between the collimator and the beam-splitter. This avoids the photodetector from saturating, while is it operated at medium gain setting.

As the system is very sensitive to the vibrations, it has been installed on a floating optical breadboard. It is a desktop vibration isolation system by *Melles Griot* (*model 07 OTT 001/011*). We use a *TMC* breadboard on which to install the lasers and other optics. Although the setup is quite stable, the output seen by the photodetector can slowly drift on account of certain unavoidable disturbances reaching the system. These disturbances include various noise signals such as building vibrations, acoustic vibrations, air currents sources, etc. This *noise* causes a slow oscillating drift in the intensity of light detected by the photo detector. Therefore, the photo detector output consists of the steady *DC* voltage due to the *IR probe* laser and the noise induced drift signal which vary extremely slowly with time.

We use a non-polarizing cube-beam-splitter by *Newport* (*model 05BC16NP .10*), and two *New- Focus mirrors* (*model 5103*). Both the mirrors are mounted on *Newport Ultra-align X-Y translation stages* (*model 561D*) to simplify the alignment procedures. A nanometer precision translation stage is added to one of the mirrors, which enable us to move it in

the direction of beam propagation. This gives us the ability to precisely change the path difference of the two beams, and eventually control the interference.

A thin film of electrochemically assembled semiconductor (*CdS / ZnSe / ZnO / CdSe*) quantum wire array constitutes the device under test. Photon energy at *1308 nm* corresponds *0.95 eV*, while the band-gap of quantum wire materials *CdS / ZnSe / ZnO / CdSe* is *2.5 / 2.69 / 3.35 / 1.74 eV* respectively. Therefore, all these materials are essentially transparent to the *probe* beam (*IR* at *1308 nm*). Hence, when this sample is placed in the path of one of the beams, absolutely no change in the power is observed on the photo detector. Moreover, the sample doesn't appear to distort the wave front of the beam, and the interference pattern is completely maintained.

A *365-nm UV* light is used as a *pump* in the experiment. We use a *UV LED* by *Nichia Corporation* (*model NCCU033-T*) to feed the *UV* light into the system. Fig. 5.6 shows the dimensions of the Nichia LED. Note that all the dimensions are in mm. The actual *LED* is just about $1 \times 1\ mm^2$ in size. The rank *M* (medium) type of *LED* that we use requires a forward voltage of *3.8-4.2 V* and emits *UV* light centered at *365 nm* wavelength at room temperature. The optical power of the emitted light varies between *110-130 mW* depending on the forward voltage. The light emits out of the *LED* dice in a 60^o angular cone. This *LED* generates considerable amount of heat (up to *2-3 W*), even when it is operated within its normal specified limits. The increase in the temperature of the *LED* per unit electric power is affected by the thermal resistance of the circuit board. To facilitate better heat dissipation, the *LED* is mounted on a metal heat sink using a high thermal conductivity epoxy adhesive.

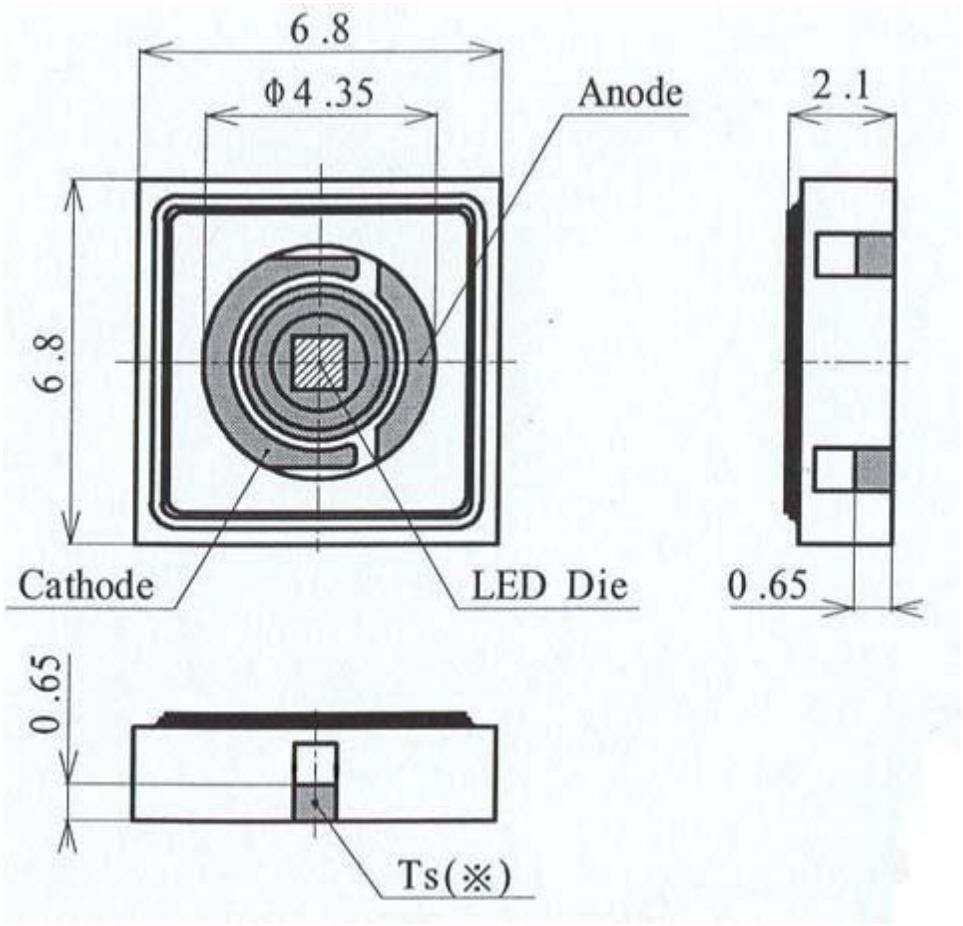

Fig. 5.6 *UV LED* (All dimensions are in *mm*)

The *UV* light at *365 nm* corresponds to *3.4 eV*. As this photon energy is larger than the band gap of (all) the semiconductor material(s) that we use, a number of electron-hole pairs are generated. This effectively changes the optical behavior of the quantum wire array, which is detected by the *IR probe* laser. To explicitly distinguish the effect of *UV* light *pump* on the optical behavior of the array, the *UV* light is modulated at *1 KHz* frequency. The *DC* component of the signal due to a stationary *probe* excitation, as well

as all the noise- created-drift components are expected to remain steady on a time scale of at least several tens of milliseconds. Hence, any *1 KHz ac* (*1 ms* time period) component in the voltage detected by the photo detector identifies the effect of UV excitation on the quantum wire array.

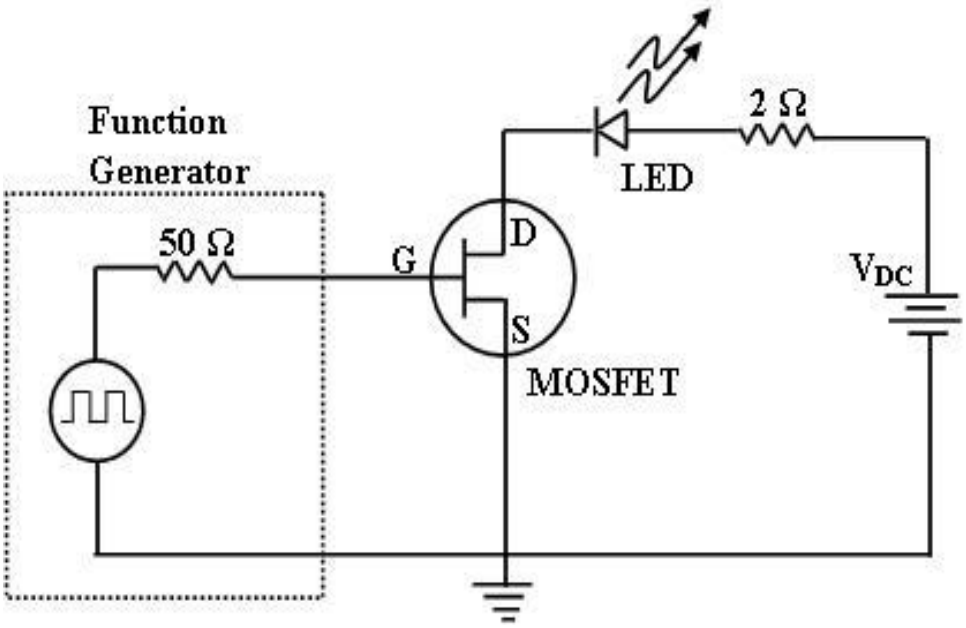

Fig 5.7 *LED* modulation circuit

Fig. 5.7 shows the circuit designed to modulate the *UV* light at *1 KHz* frequency.

The *LED* is powered by connecting it in the drain branch of a power *MOSFET*. We use *Smartdiscretes Power-MOSFET* by *Semiconductor Components Industries* (*model MLP1N06CL*). Its switching times are quite fast, and the turn ON/OFF time of the order of *1-5 μs*, are much smaller than the time period of the modulated *UV* pulse. Power *MOSFET* is switched on by giving Gate-to-Source voltage (V_{GS}) of *5V*. When the Drain-

to-Source voltage (V_{DS}) falls, the forward voltage applied across the *Nichia LED* also increases. Hence, the *LED* turns ON and starts emitting *UV* light as V_{diode} (V_{GS}) is raised above the *LED* threshold voltage of *3.8V*. When a drop across *2Ω* resistance is taken into account, the total V_{diode} is required to be raised beyond *~4.1 V* for the *LED* to emit *UV* light. A small increase beyond the *LED* threshold voltage causes a significant increase in the intensity of the emitted light.

In order to modulate the *UV* light at *1 KHz* frequency, the *Gate-to-Source voltage* V_{GS} is powered by connecting it to a *50Ω* function generator. The output of the function generator is set to generate a *1 KHz* square wave of *5V* amplitude and a *2.5V* offset. Accordingly, the *LED* turns ON for half a millisecond and is OFF for the next half. A maximum power output of about *120 mW* is possible when forward voltage V_{diode} is raised approximately to *4.3V*. To stay within the safety limits of the *LED* and for its longer lifetime (steady state operating life time is about *500* hours), the power output of the *LED* is not raised beyond *60 mW*. This corresponds to a *Drain-to-Source current* (or forward current I_{diode}) of *120 mA*.

Although the *LED* generates *60 mW* of *UV* light, it is extremely difficult to tap all of it into the system. The extremely small size of the *LED* and the space constraints on the floating optical breadboard makes it very difficult to mount the *LED* near the quantum wire array which is inserted in one of the branches of the interferometer. Moreover, the emission angle (60^{o} cone) of the light coming out of the *LED dice*, the distance of the dice from the glass window of the *LED* structure, as well as its mount (on an electrical breadboard, which consist of a Power *MOSFET* and a heat sink) complicates the focusing

issue. It is also advised to keep the *LED* away from the actual working space in order to avoid any accidental exposure to the *UV* light. Therefore, we use a *2-mm* diameter unjacketed optical grade plastic fiber strand to tap the *UV* light into the system. In order to couple most of the *UV* light into the fiber, its one end is kept as close as possible (or touched) to the glass window of the *LED*. The other end of the fiber is then mounted very close to the sample, thereby increasing the power density of the excitation pulse at the device under test.

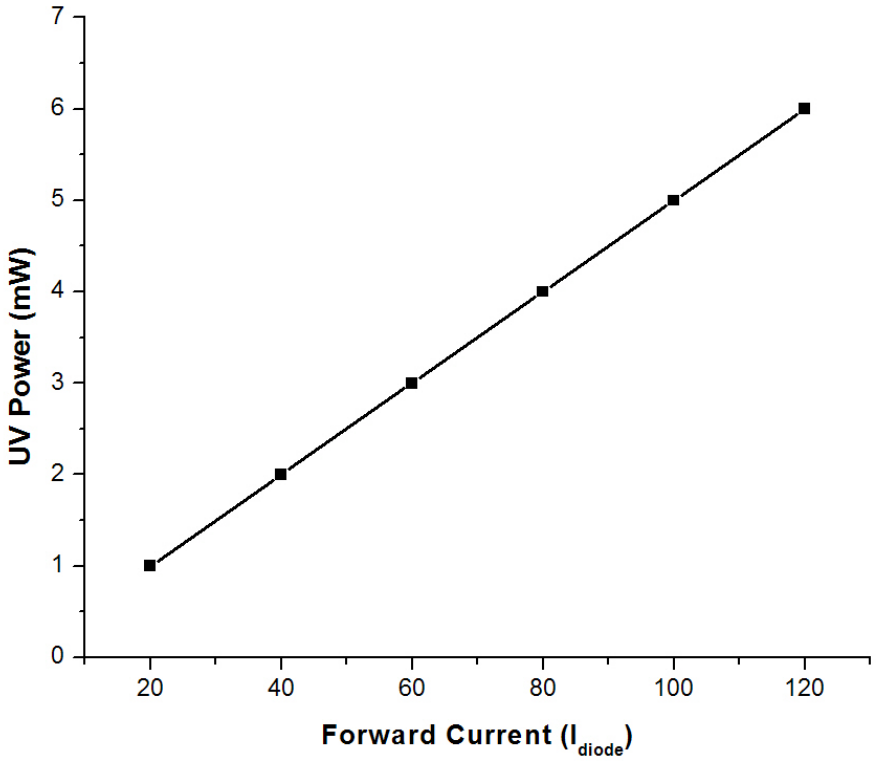

Fig. 5.8 Forward current (I_{diode}) vs *UV LED* power (*mW*) calibration curve

The *LED* power output is calibrated for the diode current I_{diode}. Fig. 5.8 shows the *UV* calibration curve for the *LED*. The plot describes the amount of *UV* light coupled from the *LED* to the other end of the unjacketed fiber as a function of I_{diode}. The light emerges out at the other end of the fiber with a very large divergence angle. Hence, even though the fiber is placed very close to the quantum wire array, all the light is not used for the excitation. We estimate that approximately *20%* of this light is actually used in the experiment. It is a very small value, on account of the smaller diameter (*~2mm*) of the probe beam, although the sample diameter is approximately *5mm*.

One of the mirrors is moved in the direction of probe beam propagation using the precision stage such that output voltage of the photo detector corresponds to the halfway point between the maxima and minima of the interference curve. The *UV pump* modulated at *1 KHz* when turned ON, creates a *1 KHz ac* component in this output detected by the detector. This ac component is measured using the *lock-in amplifier*. The output of the photo detector consists of both the *DC* and *ac* components. The required ac component is first filtered out using a simple *RC* filter circuit, as shown in Fig. 5.9. The filtered *ac* component coming out of the capacitor is then fed to the lock in amplifier. The *DC* component is detected by connecting point *B* to a *DC* scope. The voltage at point *B* indicates the position of the bias point on the interference curve. The experimental readings are valid only when this voltage remains very close to the point midway between the minima and the maxima. We also measure the voltage at point *B* using the lock-in amplifier to trace the *ac* component with the variations in the bias point. The

lock-in amplifier is also able to measure the *DC* voltage at point *B*, when it is connected to the *ADC AUX* input of the lock-in amplifier as shown in Fig. 5.9.

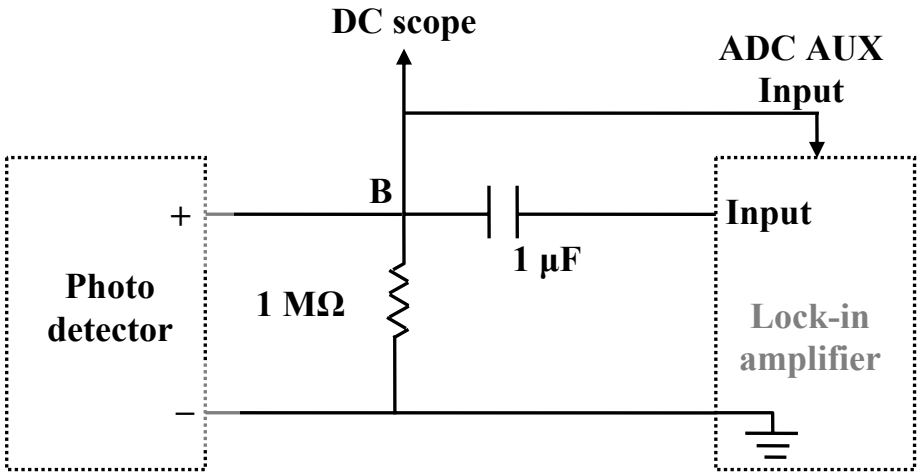

Fig. 5.9 Detection of the *ac* component

We use a single-phase analog lock-in amplifier by *Perkin Elmer Instruments* (*model 5209*) to measure the desired *ac* component in the photodetector output. The lock-in amplifier enables us to recover signals in the presence of a noise background. The fundamental purpose of a lock-in amplifier is to measure the amplitude of the component of the input voltage or current signal which is at the same frequency as that of a pre-set reference frequency (*1 KHz* in our case). *Model 5209* is able to authentically detect and measure the signals in the frequency range of *0.5 Hz* to *120 KHz*, which are as small as *100nV* to *3V*.

As shown in Fig. 5.9, the output of the photo detector is connected to *DC* scope to follow the possible drift of the bias point. It is also connected to *ADC AUX* input present at the back of the lock-in amplifier. Hence, the bias point is displayed on the lock-in output display, as well as can be measured using a computer interface. The *ac* component in the detector output is filtered using an *RC* circuit and connected to an input connector of the lock-in amplifier utilized for the voltage-sensitive mode measurements. A float type of grounding is chosen, in which the shells of the input connector are returned to chassis ground through a *1 kΩ* resistance in order to improve the ground loop interference rejection. The output display of the lock-in amplifier show four different types of outputs, namely, *OUT, NOISE, RATIO* and, *LOG-R* mode. Moreover, all these modes can measure the corresponding values in *%FS* (percentage of full scale deflection) and *SIGNAL* display mode. When the display is set at *SIGNAL/OUT* mode, the displayed value is the actual signal. On the other hand, when the display is set at *%FS/OUT* mode, the displayed value is calculated as

$$Actual\_Output = \frac{Sensitivity}{100} \times \%FS$$

Depending on the amplitude of the *ac* signal detected by the detector, we choose the sensitivity settings of the amplifier. If the detected signal is greater than the sensitivity setting, an overload (*OVLD*) indicator turns ON. We have used *10μV* and *100μV* sensitivity for all our measurements.

The *34 dB* attenuation of power line frequency (*60Hz*) as well as its second harmonic (*120 Hz*) is achieved using a line frequency rejection filter. Following this line-notch

filter, the signal passes through the main filter. The main filter is operated in low-pass, band-pass, notch and flat mode, and can even be bypassed. We choose band-pass type of main filter setting, and the filter frequency is set at *1 KHz*. The filter frequency can be tuned manually or can automatically be set to track the reference frequency. The main filter achieves the roll-off of the frequencies both below and above the reference by *12 dB*, and therefore the interfering noise components in both the frequency regions are rejected. We use external reference mode. Hence, the *SYNC* output of the function generator (which modulates the *LED* amplitude at *1 KHz*) is used as a reference signal and connected to the *TTL-logic* level input of the lock-in amplifier. In case, if the external reference is disconnected, the *UNLK* (unlink) indicator lights. Hence, the lock-in measures the amplitude of the *1 KHz* signal detected, and whose phase does not vary with the external reference input. Moreover, the time variation of the output of the lock-in should follow the time variations of the input, as well as its magnitude and phase. The output filters are chosen accordingly to reduce the level of unwanted time variations. These unwanted time variations could be random or deterministic in nature, and are referred as output noise. One major source of this output noise is the shape of the input signal waveform. The output filters implement either 1^{st} order (*6dB*) or 2^{nd} order (*12dB*) low-pass functions by the use of a combination of analog and digital techniques and are normally specified by means of a time constant. As *6dB* setting does not give satisfactory rejection of the non-random interfering signals which could possibly generate aliasing problems in analog to digital converts in the output stages, we choose *12dB* option. As the random noise is expected to be present in the input signal, the output time constant is

increased to a value such that there appears to be a compromise between the output noise reduction and the amplifier response time. We have chosen the output time constant of about *10-100 ms*. For smaller values of the amplitude of the input signal (when lock-in works at high sensitivity settings), lock-in sometimes show a non-zero value, called as a zero error. It is attributed to the unwanted coupling, or cross-talk between the reference channel and the input signal, and has to be taken care of by using a proper offset.

The amplitude of the detected *ac* signal, as well as the bias point (*DC*) voltage provided at the *ADC AUX INPUT* of the lock-in is read via the computer interface. The communication between the lock-in and the computer is achieved using National Instrument's *GPIB PCI* card. The data acquisition is performed using *Signal Recovery's Acquire* data acquisition software. Using Acquire, we generate the plot of detected *ac* signal and the bias voltage as a function of time.

Fig. 5.10 is the photograph of the experiment that was incorporated on the optical table.

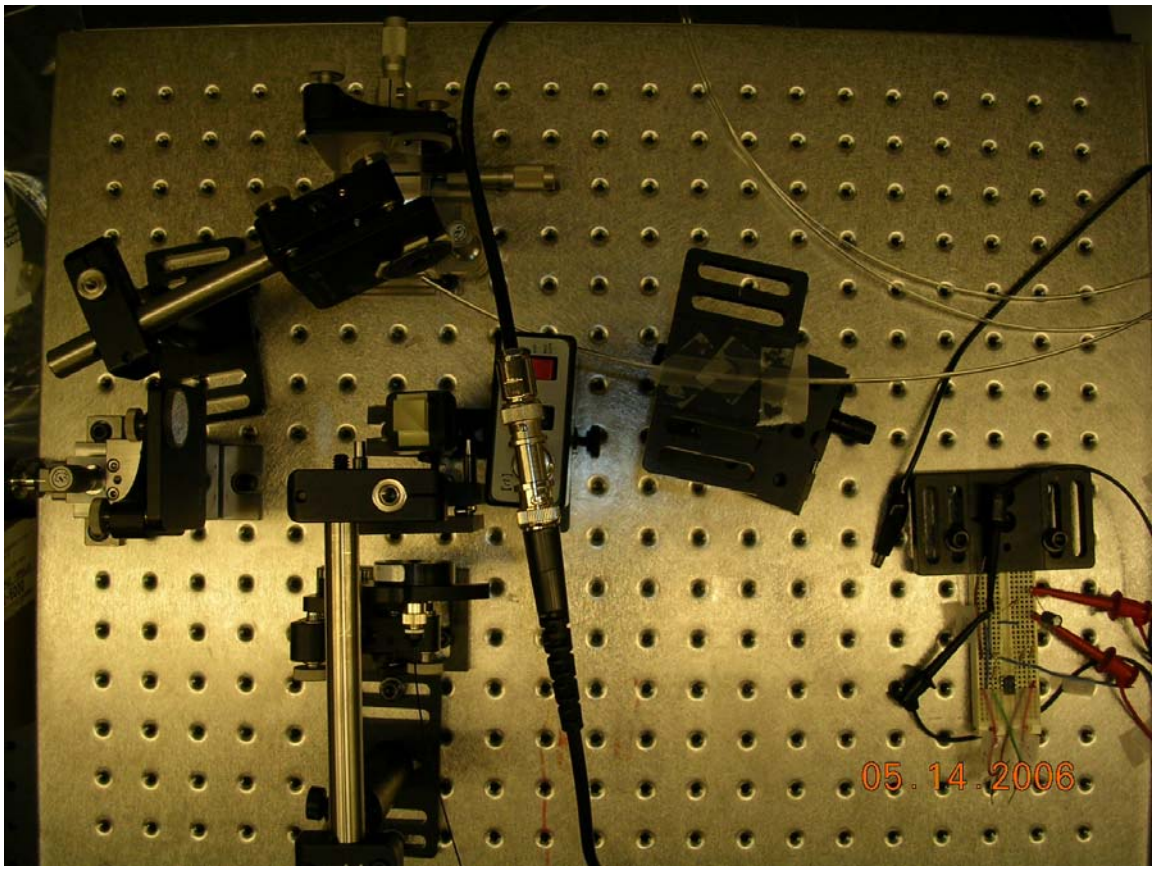

. **Fig. 5.10** Photograph of experimental setup

5.5 Experimental Procedures

We have investigated the optical properties of the electrochemically self-assembled quantum wire array using a Michelson interferometer in *pump-probe* excitation scheme. We have used four different types of semiconductor materials for the quantum wires, namely *CdS, ZnSe, ZnO* and *CdSe*. Each type of quantum wires is fabricated for three different diameters, *50 nm*, *25 nm* and *10 nm*. Moreover, we have used four samples from different batches of one type of quantum wire samples, each for one type of material and

one diameter. Hence, we use *12 CdS* samples, four each with *50-, 25-* and *10-nm* wire diameters. Thus we utilized, in all, *48* different quantum wire array samples in our experiments. In our experimental setup, we basically measure the phase shift caused by each type of the array, when excited by the *UV* light of *365 nm*. The experiment is performed at six different intensities of the *UV* light for one type of the quantum wire sample. Hence, six readings are taken for each of the *48* samples, thus generating *288* different values in total. As we generate four readings for the phase shifts for the quantum wires of one diameter and one type of material, one for each set, we average the recorded readings, making sure that the variations in the recorded values are not too large. All the fabrication processes for the quantum wire arrays are well refined; it is possible, however, that the sample might have some bad areas, discontinuities, etc. in its structure. If the probe beam is focused on that particular part of the array, the readings would be very much different than the rest of the samples. In that case, we disregard this sample and measure the test data for one more sample of the same type.

Some of the important points and the procedure to perform one set of readings is as follows.

1) Make sure that the *IR* laser is warmed up before the beginning of the experiment. We set the *IR* laser wavelength at *1308 nm*.
2) After the quantum wire array sample is installed in one of the beam paths, photo detector voltages for the individual beampath intensities, P_1 and P_{20} are recorded, the sum of which yield the bias point as can be seen in Fig. 5.3.

3) The precision translation stage is used to adjust the path difference between the beams so as to generate the detector output voltage equal to the bias voltage as in step 2.
4) The output of the detector is connected to the lock-in amplifier input via *RC* filter circuit to measure the *ac* component. All the settings in the lock-in are adjusted as described in the previous section. Bias point is followed by connecting it to the *ADC AUX* input.
5) The function generator voltage (V_{GS} for the *MOSFET*) is raised to *5 V, 1KHz* and *2.5 V* offset. Hence, *UV* is ON for 0.5 ms and OFF for 0.5 ms.
6) The intensity of *UV* light is increased by increasing the diode forward current. Fig. 5.8 describes the intensity of the *UV* light at various values of forward current. We take the measurements at six different values including *20, 40, 60, 80, 100* and *120 mA*. These current setting correspond to *UV* light intensities of *1, 2, 3, 4, 5, 6 mW* respectively. However, as mentioned previously, approximately only *20%* of this light is actually utilized to generate the *electron-hole* pairs in the quantum wires.
7) Before we record the first set of readings (for 6 intensities), the sample is rotated around the direction of beam propagation and fixed at a point which generates the maximum voltage at the detector.
8) Make sure that the position of the unjacketed fiber end (source of *UV* in the system) remains absolutely constant throughout the period of all the *48* sets of experiments. We have used a reading for one specific *50nm* diameter *CdS* sample

as a reference measurement. Before every set of experiments, we check that the set of outputs measured by the lock-in for that particular sample has not changed. This particular step fulfills the requirement that the experiment is performed when all the other conditions are constant.

9) The sensitivity, input/output filters, reference signal, time constants and the output display of the lock-in are adjusted so as to display the correct value of the *1 KHz ac* component generated due to *UV* excitation.

10) Using *Acquire* data acquisition software, the bias voltage and amplitude of the *ac* component is recorded. The data is recorded for about *one* minute at the rate of about *1* data point per *10* milliseconds. We make sure that the bias point remains midway between the maxima and minima throughout the period of *one* minute measurement. The reading is repeated in case if any unexpected disturbance drastically changes the value. We later average the curve over one minute to obtain the accurate value of the phase shift measurement.

Fig. 5.11 shows the one such measurement taken. In Fig. 5.11, the upper curve indicates the bias point, which remains constant around *2V* (right Y-Scale) throughout the *60* seconds for which above data has been collected. Each data point is collected after every *10 milliseconds*. The lower curve represents the *ac* component of the photo detector output. The reading indicates the *ac* component to be around *20-25 μV* value, according to the left Y-Scale.

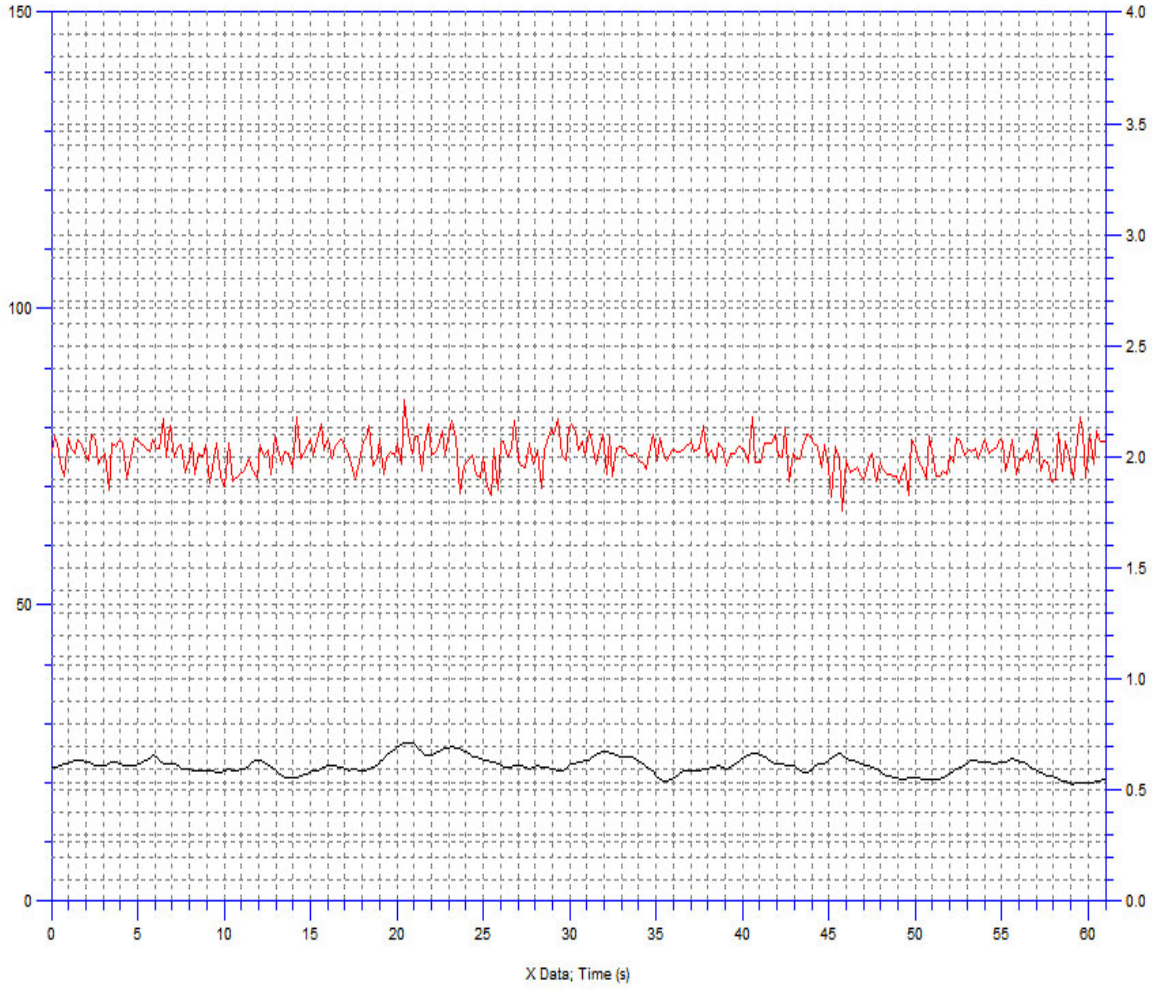

Fig. 5.11 The Acquire data acquisition plot

Table 10 and Table 11 describe the magnitude of the *ac* components (*in μV*) recorded for *10/25/50 nm* diameter quantum wire arrays of *CdS, Znse, ZnO and CdSe* materials, for six different *UV* intensities. Note that every single value in each table represent the average of the recorded readings of four separate quantum wire array samples of the same type, each of which is in turn averaged over the period of about one minute. The range of measured data points vary between 3-7% of their corresponding average values.

UV LED Forward Current (mA)	Wire diameters (nm)					
	CdS			ZnSe		
	50	25	10	50	25	10
20	*19.7125*	*22.74*	*16.5025*	*23.35*	*27.17*	*21.14*
40	*48.7175*	*51.4475*	*39.5325*	*53.09*	*55.275*	*46.84*
60	*73.5725*	*81.575*	*58.8575*	*83.4475*	*88.4825*	*73.76*
80	*99.21875*	*109.6125*	*80.995*	*111.635*	*119.275*	*97.0675*
100	*128.1075*	*143.9325*	*103.4675*	*145.75*	*150.415*	*122.045*
120	*157.2748*	*176.7375*	*126.5475*	*179.0625*	*184.4625*	*151.2225*

Table 10 LED Forward Current vs the *ac* component of the detector output (*in* μV) for *UV* excited *CdS* and *ZnSe* quantum wire arrays.

UV LED Forward Current (mA)	Wire diameters (nm)					
	ZnO			CdSe		
	50	25	10	50	25	10
20	*25.73*	*31.39*	*22.068*	*21.295*	*20.05*	*16.81*
40	*55.075*	*63.784*	*47.554*	*51.53*	*44.63*	*36.8033333*
60	*85.515*	*101.504*	*75.184*	*81.5625*	*71.06*	*57.6633333*
80	*114.535*	*132.416*	*98.626*	*107.1875*	*92.89*	*75.3433333*
100	*144.8475*	*169.476*	*129.052*	*136.325*	*117.6175*	*95.3366667*
120	*173.8675*	*202.804*	*152.448*	*163.37*	*141.3825*	*115.033333*

Table 11 LED Forward Current vs the ac component of the detector output (*in μV*) for *UV* excited *ZnO* and *CdSe* quantum wire arrays

Note that the *IR probe* beam passes through the device under test twice in a Michelson interferometer, as could be seen in Fig. 5.2 and Fig. 5.5. Therefore, even though the actual length of quantum wires fabricated is approximately *1 micron*, the phase changes we obtained are effectively due to *2 micron* long wires.

Fig. 5.12 shows the *1 KHz* ac component detected by the lock in amplifier as a function of *UV* power, for four different samples of *ZnSe* wires of *10-nm* diameter. As all the

corresponding values for each sample do not vary much from their mean, the average value of the four samples is completely valid for the calculations.

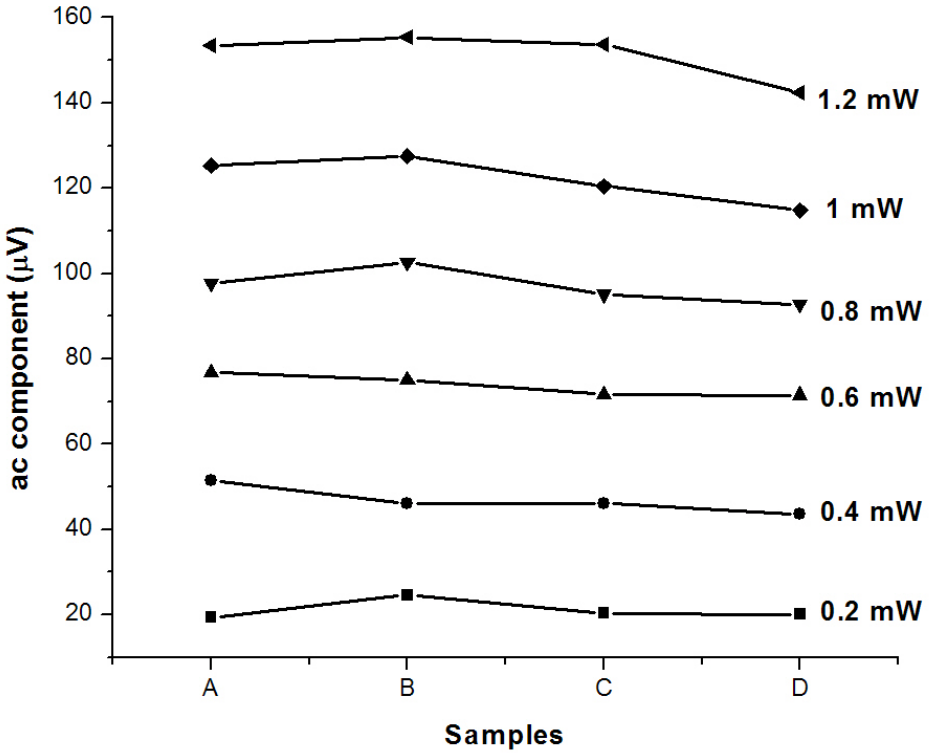

Fig. 5.12 *ac* component (in μV) detected by the lock-in amplifier for four different *10-nm* diameter *UV* excited *ZnSe* quantum wire array samples

The actual value of the changes in phase shift ($\Delta(\varphi)$ and refractive index change of the quantum wire array) is calculated using equations (5.10) and (5.11). The value of the amplitudes of the individual IR probe beam intensities are calculated in terms of the photodetector voltages. Fig. 5.13 shows the calibration of the photodetector voltage with respect to the probe beam intensity as measured using the New Focus photodetector and a

Newport precision power meter. The slope of the curve is *1 Volt* per *16 μW* of light when operated at the photodetector medium gain setting.

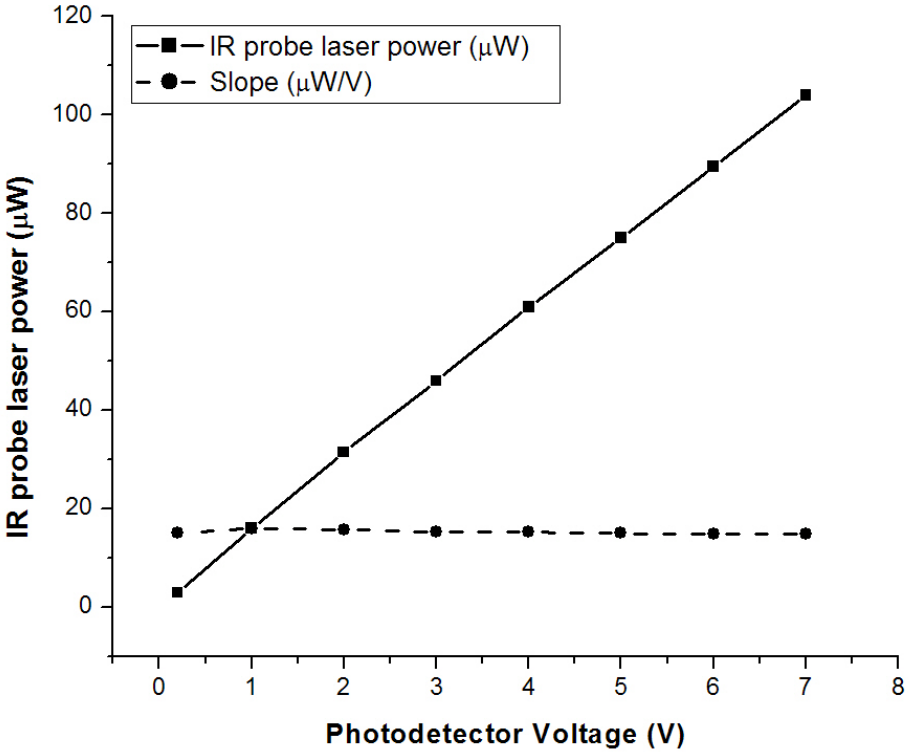

Fig. 5.13 IR probe laser power vs photodetector voltage calibration curve

The actual phase shift differences between the two beams in a Michelson interferometer, as the quantum wire array is excited by *UV* light at six different intensity levels, are presented and discussed in the next chapter, where we correlate all the theoretical model data (Mathematica and HFSS) and the experimental results.

CHAPTER 6

Results and Discussion

6.1 The plausible sources of size-dependent non-monotonic optical behavior

As we observe in Table 10 and Table 11 in Chapter 5, the quantum wire arrays display a size-dependent non-monotonic behavior when excited by *UV* light. This non-monotonic behavior is explicitly demonstrated in the next section where we plot the changes in the optical behavior of the quantum wire arrays of *CdS/ZnSe/ZnO/CdSe* under stationary *UV* excitation. In this chapter, we analyze the plausible physical processes responsible for this size-dependent non-monotonic behavior, which include screening effect, phase-space-filling effect, dielectric de-confinement, quantum confined Stark effect, effect of polarization, quantum confinement effect including the changes in the density of states function with wire diameter and the effect of filling factor variation with wire diameter. Although all these processes co-exist and compete with each other, in particular, the last two phenomena are dominantly responsible for the size-dependent non-monotonic nature of the optical behavior observed. In case of *ZnO* where energy bandgap is very close to the *UV* pump energy used in the experiment, the excitonic effects are also extremely important. In the next few sections, we explore these possible physical effects responsible for the non-monotonic behavior observed.

6.1.1 Screening effects

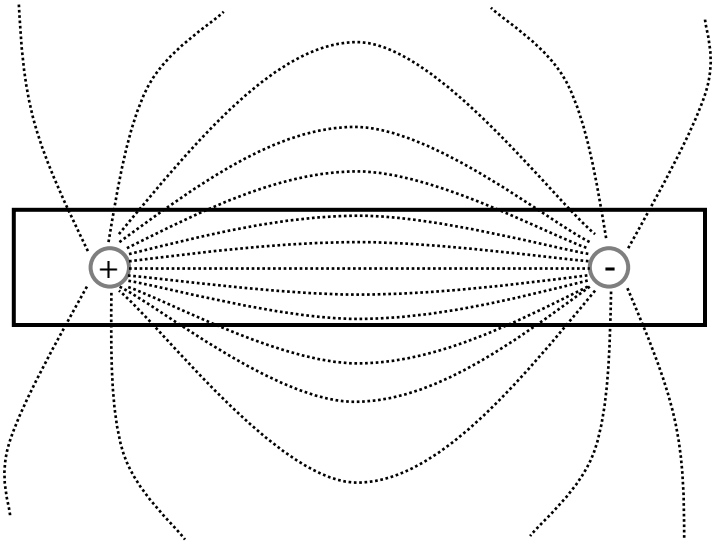

Fig. 6.1 Electric field lines in quantum wire

The term *screening* represents the shielding of the electric field by the mobile charge carriers. We already discussed the Coulomb interaction between the charge carriers. The charge carriers present in the vicinity of two interacting particles causes a damping effect on the electric field lines between them. This is called the screening effect.

Figure 6.1 shows the electric field lines between two interacting particles. As the dimensionality of the system decreases, more and more field lines pass through the neighboring material. In case of quantum wires, most of the field lines pass through the material which surrounds them. Moreover, in our case, as the band gap of alumina is much larger (*~8-10 eV*) than the UV excitation energy, the carriers are not created in

alumina, and the photo-generated electrons and holes are confined to the quantum wire only. As there are no photogenerated charge carriers in the surrounding alumina, the electric field lines there cannot be screened. However, as very few lines pass through the wire material as depicted in Fig. 6.1, the effect of screening is extremely weak in quantum wires [53]. The effect of screening further diminishes as the wire diameter is reduced. Although this screening effect, which gives rise to spatial redistribution of electrons and holes, is usually suppressed in quantum wires, it might be intensified if the effects of image charges are taken into account [110].

6.1.2 Phase Space filling effect

As the dimensionality of the system is reduced, so is its density of states, as shown in Fig. 1.1. The density of states function is narrower in a *1-dimensional* system, and diverges at the bottom of each sub-band. Moreover, due to the additional spatial confinements, fewer states are available for transitions. In case of an exciton, which consists of a bound pair of an electron and hole, both of which follow Pauli's exclusion principle, only those electron-hole states may be utilized to create an exciton which are not occupied by the free carriers. For increasing excitation energy, when large numbers of electron-hole pairs are generated, the absorption peaks reaches saturation due to the filling of the phase space. The effect of phase-space-filling in excitonic absorption is described extensively in [110]-[112]. However, in case of the width of the saturated peaks being too large, it might be attributed to the size dispersion of the wires (non-uniform filling of the porous alumina), rather than the phase space filling effect.

Both phase space filling effect and screening cause the bleaching or saturation of the absorption effects in presence of high density of carriers, by reducing the Coulomb interaction potential. In case of quantum wires, screening effect is of minor importance as compared to the effect of filling the reduced number of states. Moreover, at higher excitation when large numbers of electron-holes pairs are generated, the filling of the states by the carriers, not screening, is mainly responsible for the ionization of excitons. As the wire diameter reduces, the effect of phase space filling is even more prominent than the screening effect. However, as no bleaching or saturation effect is observed in our experiments with low UV excitation energies, phase space filling as well as screening effects are expected to be unimportant.

6.1.3 Dielectric confinement and image potentials

It is possible to control the strength of Coulomb interactions and the exciton binding energy in a quantum well or wire by properly combining the semiconductor and barrier materials of different dielectric constants, and described as a realization of *Coulomb interaction engineering* by Keldysh in [113]. The exciton binding energy as well as its oscillator strength is dramatically increased when the barrier material surrounding the semiconductor (in a well or wire) is an insulator with smaller dielectric constant than the quantum well / wire material. The phenomenon is termed dielectric confinement or dielectric enhancement effect, and was first theoretically reported in [114]-[117]. The larger the mismatch between their permittivities, the larger is the dielectric enhancement effect. We know that there is weak Coulomb interaction between the charges in materials

with high dielectric constant, and a stronger interaction in materials with smaller dielectric constant. As shown in Fig. 6.1, in quantum wires, most of the electric field lines between the charge carriers pass through the surrounding insulator (with smaller permittivity), and thus enhances the Coulomb interaction between them.

The effect could also be understood in terms of image potentials. Due to the large difference between the permittivities of the wire and surrounding material, image potentials play an extremely important role in determining the *quasi-1D* character of the excitons. The electrostatic field of a charge placed close to an interface can be represented in terms its unit charge and a mirror-like reflection of the charge placed on the opposite side of the interface. The strength of the field depends on the ratio of the dielectric constants from both sides of the interface. As the dielectric constant changes abruptly at the interface, the Coulomb-like divergence occurs when a charge encounters its image. In a semiconductor, the charge is repelled away from the interface, while it is attracted towards the interface in the surrounding insulator. This greatly modifies the wire shape by reducing its diameter, and primarily affects the band gap, as well as exciton peak intensity and position [118]-[120]. Others have also explained the dielectric enhancement effect and suggested certain improvements with great details. [121]-[122].

References [123]-[125] observed a large enhancement in the exciton binding energies and their oscillator strengths in quantum wires deposited in electrochemically self-assembled porous alumina, which they attributed to the dielectric enhancement effect. But these groups erroneously assumed the dielectric constant of alumina to be ~2.2 which is much

smaller than that of CdS (5.4) and CdSe (6.26) quantum wire materials which they investigated. Actually, the value of alumina permittivity varies between *8-10* [107],[126]-[127]. Although, such low value of permittivity of alumina has been reported in references [108] and [128], the reduction in the permittivity is attributed to the nano-porosity of the porous alumna templates. In other words, the permittivity value in their work is averaged over the air-filled pores with dielectric constant of 1, which is not relevant in our case, as the pores in the alumina templates are filled with *CdS/ZnSe/ZnSe/CdSe* semiconductor materials. The absorption enhancement effects at smaller diameters observed in our experiments are actually in the presence of a dielectric *de-confinement* effect. This fact is recently corroborated by Bandyopadhyay in [129].

6.1.4 Direction of optical field polarization

One of the important properties of the low-dimensional nanostructures, which is also manifested in its optical spectra, is the significant anisotropy of optical signal with respect to the polarization of the applied electromagnetic field. [130]-[131]. In the nanostructures like the quantum array we have, for the wire radius much smaller than the wavelength of light, the light electromagnetic field inside the array can be treated as a plane wave modulated on the scale of a wire radius. When the excitation EM field is perpendicular to the wire axis, the local field inside the array is strongly modulated, while no such modulation takes place when the field is in the direction of the wire axis. Under such condition, the field component of light with polarization normal to wire axis is

weakened which minimizes the absorption for that component. Any absorption is completely attributed to the field component in the direction of the wire growth.

It must be noted that inter-subband transitions like those in the far-infrared photo detectors (*QWIPs*), only *TM* polarization ($\vec{E}$ field perpendicular to well layers or wire axis) is absorbed. However, in case of inter-band transitions, *TE* polarization ($\vec{E}$ field parallel to well layers or wire axis) of the excitation light is also absorbed [132].

As we use unpolarized *LED* light for the sample excitation, this effect is not relevant to us. Moreover, the quantum wire array is excited with the *UV* light incident at an angle to the quantum wire axis to nullify any possible such effects.

6.1.5 Quantum confined Stark effect

When the electric field is applied across the quantum wire with a component perpendicular to the wire axis, there are significant changes in its optical properties like absorption, reflectance, photoluminescence, etc. This effect is termed as quantum confined Stark effect (*QCSE*) and was first reported in [133]-[135]. It is an extension to the Franz-Keldysh phenomenon in the low-dimensional systems, but its effects are extremely different in character from the Franz-Keldysh effect seen in bulk materials. Very distinct physical effects are found in quantum wells when the applied electric field is in the direction parallel to the well layers and when the electric field is perpendicular to the well layers.

When electric field is parallel to the quantum well layers, the exciton peaks are broadened with the field. This broadening is essentially is due to the reduction in the

exciton lifetime due to the field ionization from the applied electric field. When the applied field is strong enough, no bound electron-hole pairs exist, as the particles tunnel through the resulting Coulomb potential barrier. This is qualitatively similar to the electro-absorption in bulk, or Franz-Keldysh effect.

On the other hand, in addition to the broadening of the peaks, large energy shifts (to longer wavelength) are observed in the exciton peaks when the field is applied perpendicular to the well layers, while the peaks remain resolvable even for larger values of applied electric fields. Miller [135] also showed that the shifts in heavy hole exciton energy is more than the light hole exciton energy, making the phenomenon mass dependent. The electro-absorption effect due to the applied field is considered as the quantum confined Stark effect. As the electron and holes are pulled away from each other under the influence of the field, it increases the separation between them and reduces the Coulomb interaction. This causes an overall net reduction in the energy of electron-hole pair and a Stark shift is in the exciton absorption. But due to the confinement, the walls of the well impede the electrons and holes from tunneling out of the well, and hence the *e-h* interaction, although slightly weakened by their separation, might still be strong. Thus well defined exciton states still exist in stronger electric fields. The broadening due to tunneling of electrons and holes is important only at very strong electric fields.

In case of quantum wires, the quantum confined Stark effect is due to the influence of the field perpendicular to the wire axis. The single electron particle energies under the influence of the electric field are given as

$$\varepsilon_k^j = \frac{\hbar^2 k^2}{2m_j} + \frac{\Omega_j}{2} - \frac{e^2 E^2}{2m_j \Omega_j^2} \tag{6.1}$$

where $j = e$ and h, while Ω represents the inter-subband spacing, and E is the applied electric field in the direction normal to wire axis. This clearly suggests that the particle energies decrease with the increase in the field strength. However, the influence of the field is reduced for materials with heavier charge carriers. Under the influence of external electric field, the overlap between the lateral electron and hole wave function is reduced, which effectively reduces the electron-hole interaction. Furthermore, there is also a reduction in the optical dipole transition element as

$$d_{eh}(E) = d_{eh}(E=0) \times e^{-\frac{m\Delta^2\Omega}{2}} \tag{6.2}$$

where Δ is the measure of field induced electron-hole separation.

Benner and Haug [61] showed the influence of the electric field on the linear optical absorption spectra of quantum wires. In the absence of the field, one may expect a small red-shift of the absorption peaks due to the reduction of the binding energy by Coulomb blocking. For weaker field though, there is a small blue shift in the exciton peaks, which indicate the stronger confinement effect. However, for large electric fields, the Stark effect dominates and the absorption peaks shift red. Under the influence of the electric field, the exciton absorption peaks consistently bleach due to the reduced electron-hole overlap. However, the reduction in oscillator strengths in extremely narrow quantum wires are reported to be largely dominated by the phase space filling effect, rather than the quantum confined stark effect [136].

6.1.6 Interface states, Fermi level pinning and built-in field effects

Interface states, also known as surface states, interface trapped charges, defects, and fast states, are formed by incomplete covalent bonds at the surface (or interface) of the semiconductor [137] and are found only at the atom levels closest to the surface (or interface). While the surface states are present at any semiconductor surface, they can also be caused by impurities such as oxygen. The surface (interface) states exist within the forbidden gap due to the interruption of the periodic lattice structure at the surface of the crystal or at the interface of two materials, and due to the presence of the impurities, and result in energy levels within the band gap. These states do not have an equivalent in the band structure of the crystal, which peak near the surface (or interface) plane and decay in amplitude away from the surface. These surfaces or interfaces typically contain a large number of recombination centers because of the abrupt termination of the semiconductor crystal, which leaves a large number of electrically active dangling bonds. They could be donor or acceptor states depending on weather or not they are neutral when occupied. The surface state, or the interface trap is considered donor if it becomes neutral (or positive) by donating an electron. On the other hand, it is acceptor if it becomes neutral (or negative) by accepting an electron.

The surface states cause the *Fermi* energy to be pinned, i.e. electrons from the valence band fall into the surface states until the *Fermi* energy coincides with the level to which the surface states are filled. This causes a natural surface depletion in the material where they exist (near the surface/interface), and a built-in potential is also created. However

pinning does not happen on every semiconductor surface, as the surface states are not necessarily positioned inside the band gap of some semiconductor surfaces.

Here, the Charge Neutrality Level (*CNL*) concept is also important. At low temperatures, the surface states are populated from lowest energy level to the Fermi level. If electrons are filled to the point short of *CNL*, i.e. when Fermi level is lower that *CNL*, the closest surface region (i.e. the first few atomic planes on the surface) has net positive charge. When Fermi level is above the *CNL*, the surface has an excess of electrons and has negative charge. Even a relatively low density of surface states can fixe the surface Fermi level very close to the *CNL*, and Fermi level is said to be pinned by the surface states.

As described above, any field present in the nanostructures in the absence of the external electric field is attributed to the built-in fields produced by these interface states or trapped charges. Built-in fields have already been reported to be very strong, of the order of *10 MV/cm*, in *AlGaN/GaN* quantum wells [138]. It has been reported in [129] and [139] that strong built-in electric fields are also present in the alumina templates that we have used in the experiments. These built-in fields might have possibly caused the quantum confined Stark effect in *ZnO* samples.

6.1.7 Quantum confinement effect

The density of states function changes with the reduction in wire diameter. The joint density of states (DOS) function in quantum wires (plotted in Fig. 1.1) is given as,

$$DOS^{1D}(E) = \frac{L}{\pi}\left(\sqrt{\frac{2m_r}{\hbar^2}}\right)\sum_{n,p}\frac{1}{\sqrt{E-\varepsilon_{n,p}}}\Theta\left(E-\varepsilon_{n,p}\right) \tag{6.3}$$

where L is the wire length, m_r is reduced effective mass, Θ is the Heaviside unit step function and $\varepsilon_{n,p}$ are the intersubband transition energies. With the reduction in wire diameter, blue shifts in $\varepsilon_{n,p}$ are caused by additional quantum confinement, leading to an increase in the *DOS* function, as depicted in Fig. 6.2. As the confinement length (wire diameter) is reduced, more states are available for absorption for any excitation energy E_1 in wires with smaller diameters. Therefore, optical activity is expected to increase as the diameter of the wire is reduced.

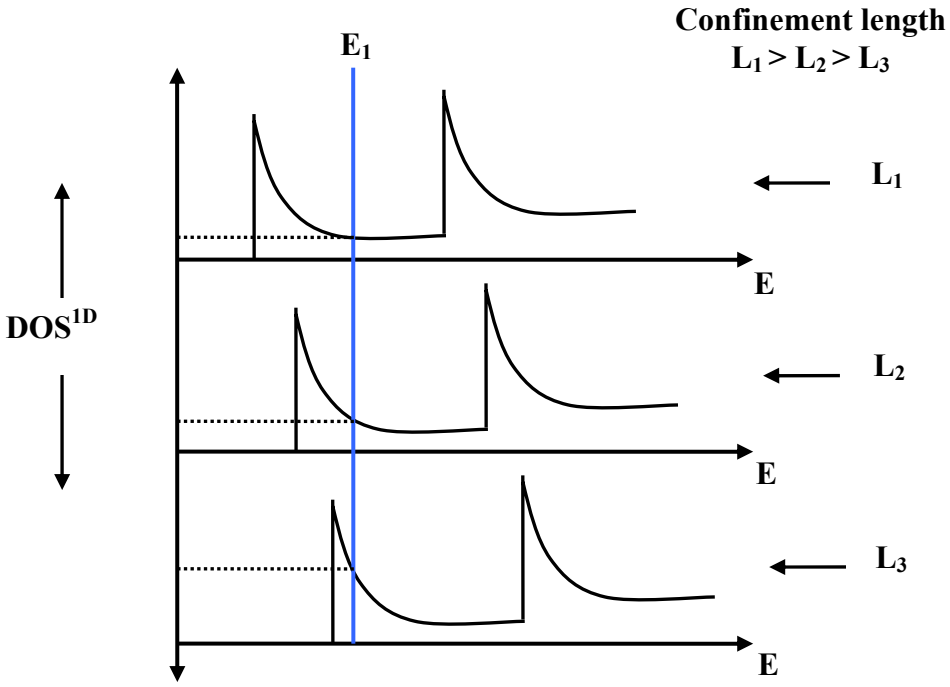

Fig. 6.2 Changes in the DOS function with the reduction in wire diameter.

The excitonic activity is also affected by the reduction in confinement lengths. The electron-hole Coulomb interaction in semiconductors leads to bound excitonic states,

which, at relatively low carrier densities, are found to be very crucial in determining the optical response of the system. When the exciton binding energy exceeds the thermal energy at room temperature, excitonic effects become dominant. It is possible to obtain a large enhancement of the binding energy and the oscillator strength by confining electron and hole wave functions in nanostructures of low dimensionality. The phenomenon is called as quantum confinement effect, which is more regular with the *1-dimensional* systems. In quantum wires where carriers and excitons move freely in only one direction and are confined in other two, the exciton binding energy and their oscillator strength increases. The restriction of motion reduces the distance between an electron and a hole, which effectively enhances their Coulomb interaction and hence their binding energy. It has been predicted in [70] that for semiconductor quantum wires of radii comparable to or smaller than the bulk exciton Bohr radius, there is considerable increase in the exciton binding energies and their oscillator strengths. Keldysh [113] provided a detailed discussion to prove that the confinement in nanostructures with linear sizes smaller in comparison with the exciton Bohr radius is responsible for the enhancement of binding energy and oscillator strength. The binding energy for extremely thin quantum wire where $r \approx a_0$, or $r < a_0$ is evaluated in [113] as

$$E_b \propto 4 * Ry * \left[\ln\left(r / a_0\right)\right]^2 \tag{6.4}$$

where a_0 is the bulk exciton Bohr radius, Ry is the Rydberg energy unit, and r is the wire radius. Thus in case of extremely thin quantum wires, as the wire diameter is reduced as compared to the bulk exciton radius, the two dimensional confinement itself leads to a

significant increase in the binding energy. The oscillator strengths are also reported to be considerably enhanced.

6.1.8 The effect of filling factor

Classically, UV pump absorption should decrease in narrower wires since the amount of optical material present is reduced. As shown in Table 7 in Ch. 4, in the nanowire arrays used in the experiments, center-to-center distances between the pores in 50-, 25- and 10-nm diameter wires are approximately 100-, 80- and 60-nm, respectively. Accordingly, the wire density is in the range of $10^9 - 10^{12}$ cm^{-2}. This monotonically reduces the amount of optically active material per unit area of the wire array. Hence, the optical activity seen by the nanowire array is expected to reduce as the wire diameter decreases. Since the nanowire array has a honeycomb structure as shown in Fig. 4.6 and 4.8, filling factor *f*, the approximate ratio of total cross-sectional area of the wires to the total array area exposed to the IR probe, is calculated as the ratio of a single wire area to the area of the hexagonal unit cell. For an unperturbed wire array, the effective permittivity is approximated by

$$\varepsilon = f\varepsilon_{wire} + (1 - f)\varepsilon_{alumina} \tag{6.5}$$

where ε_{wire} and $\varepsilon_{alumina}$ are the permittivity of wire material and alumina, respectively. Under UV pump excitation, only the permittivity of the wire material changes. Hence, the effective permittivity of the UV excited wire array becomes,

$$\varepsilon' = f\varepsilon'_{wire} + (1 - f)\varepsilon_{alumina} \tag{6.6}$$

Therefore, the change in permittivity of the array sample, $\Delta\varepsilon = \varepsilon' - \varepsilon$, is given as

$$\Delta\varepsilon = f(\varepsilon'_{wire} - \varepsilon_{wire}) \tag{6.7}$$

where we have assumed that there is no change in the permittivity of the alumina since its bandgap is much larger than the UV photon energy. Since $\delta n \approx (1/2\sqrt{\varepsilon})\Delta\varepsilon$, change in phase shift becomes directly proportional to the filling factor f as,

$$\delta\varphi \cong \left[\frac{2\pi}{\lambda} \times l \times \frac{1}{2\sqrt{\varepsilon}}\left(\varepsilon'_{wire} - \varepsilon_{wire}\right)\right] \times f \tag{6.8}$$

Filling factor f is approximately calculated as *0.2267, 0.0886* and *0.0252* for *50-, 25-*, and *10-nm* diameter wires, respectively. Since the filling factor reduces with the wire diameter, the optical activity in the DUT sample is expected to monotonically reduce as the wire diameters in the array decrease.

6.2 Experimental Data Analysis

We had discussed experimental procedure in detail in Ch. 5. As shown in Table 10 and Table 11 in Ch. 5, we measured the *ac* component of the photodetector output as function of forward current of the *UV LED*. The ac component output is then converted into the actual change in the phase shift induced by the quantum wire array under *UV* excitation, as per the discussion in section 5.2. The photodetector voltage output is converted to power using the photodetector power calibration curve as shown in Fig. 5.13, while equations 5.10 and 5.11 are used for the actual conversions. The actual power of the *UV LED* used for excitation is calculated using the calibration curve shown in Fig. 5.8. Figures 6.3-6.6 display the actual changes in phase shifts induced by the *UV* light at five

different intensities, for *CdS/ZnO/ZnSe/CdSe* quantum wire arrays respectively. Note here that changes in phase shifts are extremely small for the perturbational UV excitation used and are expressed in terms of *parts per million* (*ppm*). Moreover, as the *IR* laser passes twice through the quantum wire array in the Michelson interferometer, the effective length of the wires inducing the phase shift changes is *2 microns*, double the actual length of the wires in the array.

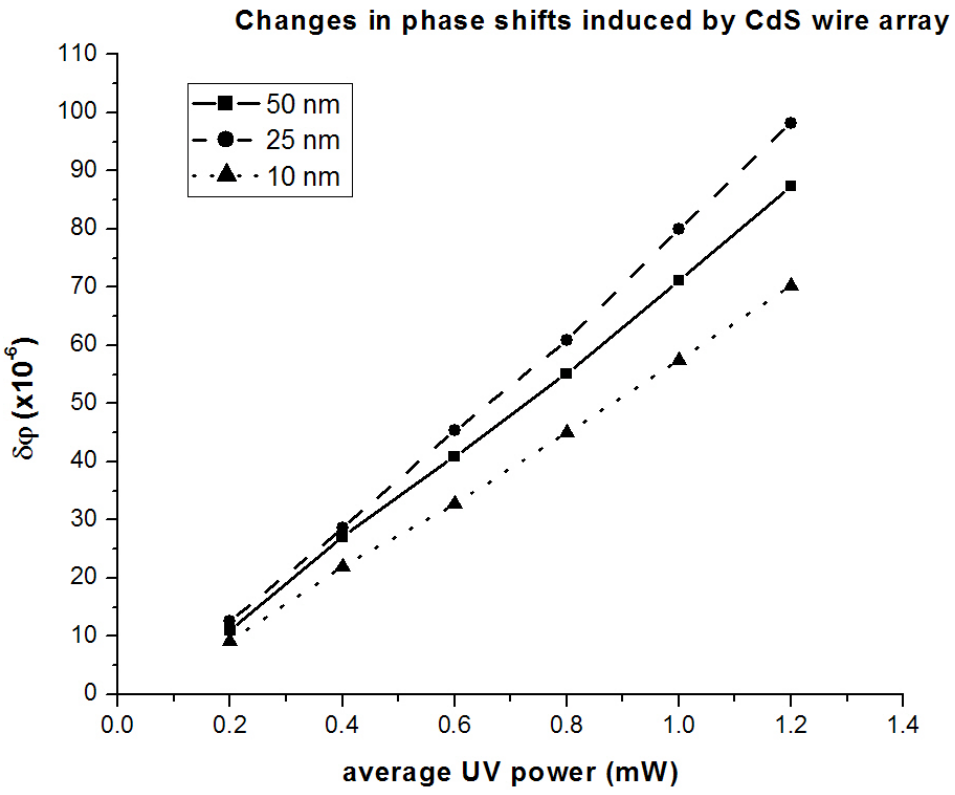

Fig. 6.3 Changes in phase shifts induced by *UV* light in *CdS* quantum wire array

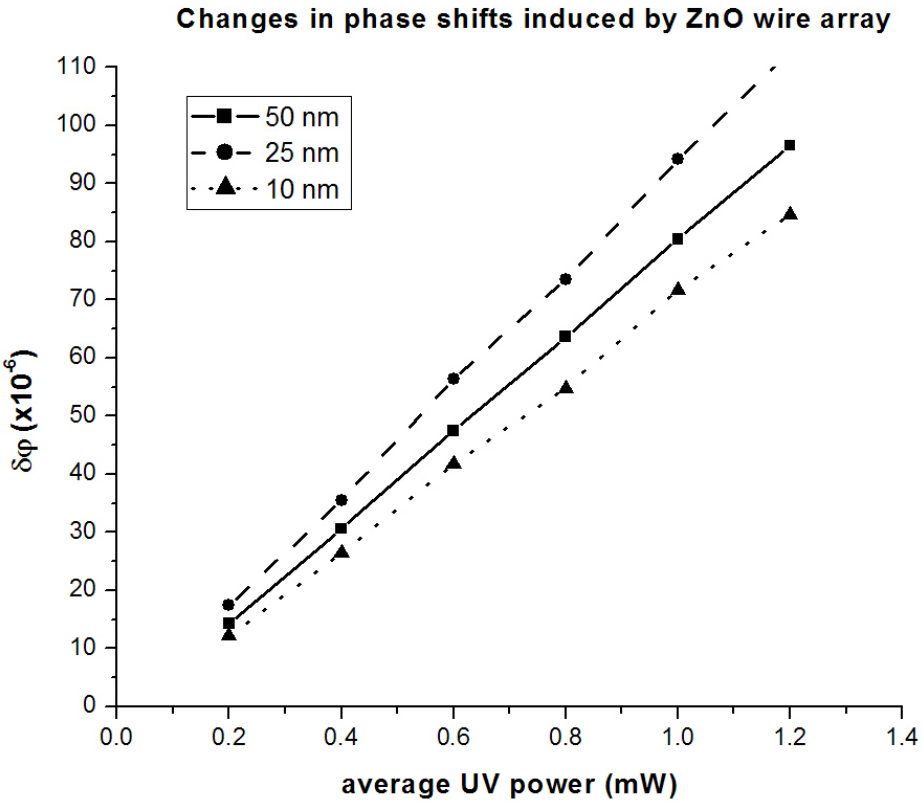

Fig. 6.4 Changes in phase shifts induced by *UV* light in *ZnO* quantum wire array

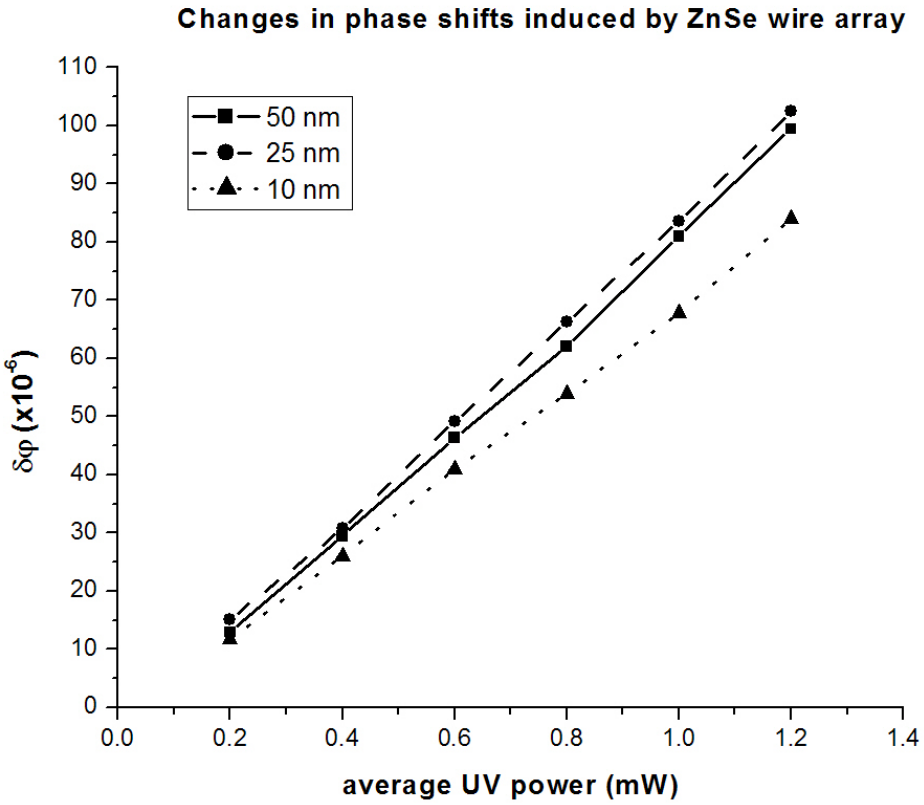

Fig. 6.5 Changes in phase shifts induced by *UV* light in *ZnSe* quantum wire array

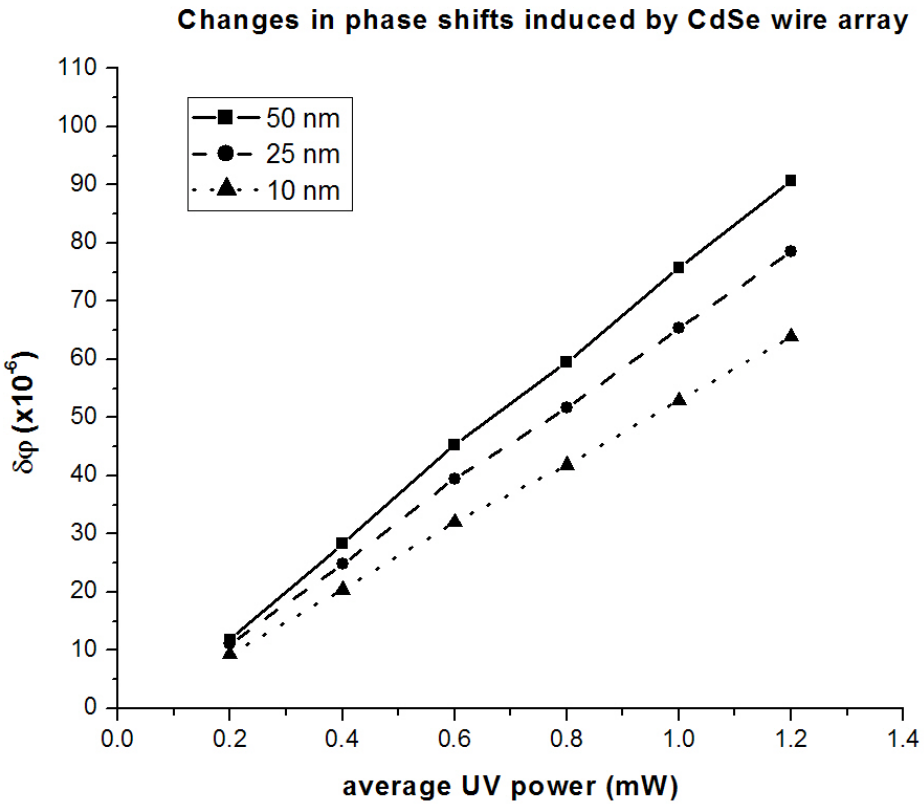

Fig. 6.6 Changes in phase shifts induced by *UV* light in *CdSe* quantum wire array

There is an extremely peculiar behavior that the optical response of the entire sample shows in Figures 6.3 - 6.6. Although, the phase shift changes increases gradually with the *UV* intensity in all the samples, the activity shown by *CdS* and *ZnO* quantum wires does not vary linearly with the variations in their diameter. The optical activity (or the phase shift changes) shows a distinct increase as the wire diameter is decreased from *50* nm to

25 nm. This behavior is against the initial expectation that the changes in phase shifts would gradually reduce with decreasing filling factor as the wire diameter decreases.

Using the data shown in Table 7 in Ch. 4, we estimate that the filling factor of the semiconductor in the quantum wire array falls rapidly with decreasing wire diameter. As mentioned in section 6.1.8, filling factors for *50-, 25-* and *10-nm* diameter wires are calculated as 0.*2267, 0.0886* and 0.0*254* respectively. Although, semiconductor material available for UV absorption reduces by approximately *60%* as the wire diameter is changed from *50 to 25 nm*, the actual activity (changes in phase shifts) in 25 nm wires is significantly enhanced.

As the wire diameter (in *CdS* and *ZnO* samples) is further reduced to *10 nm*, the phase shift changes decline and reach the minimum value of all three wire diameters at the same *UV* intensity.

A similar effect is also observed in *ZnSe* quantum wire arrays, although the increment in the optical activity as the wire diameter changes from *25 nm* to *50 nm* is suppressed as compared to that in case of *CdS* and *ZnO* samples. In case of *CdSe* quantum wire arrays, however, the phase shift changes reduce gradually as the wire diameter is decreased from *50 nm* to *25 nm* and finally to *10 nm*.

The effect of the diameter variations in the quantum wires is displayed for all four types of samples, namely *CdS / ZnO / ZnSe / CdSe*, in Fig. 6.7, where we plot the phase changes induced by *1.2 mW UV* excitation for all the four types of arrays.

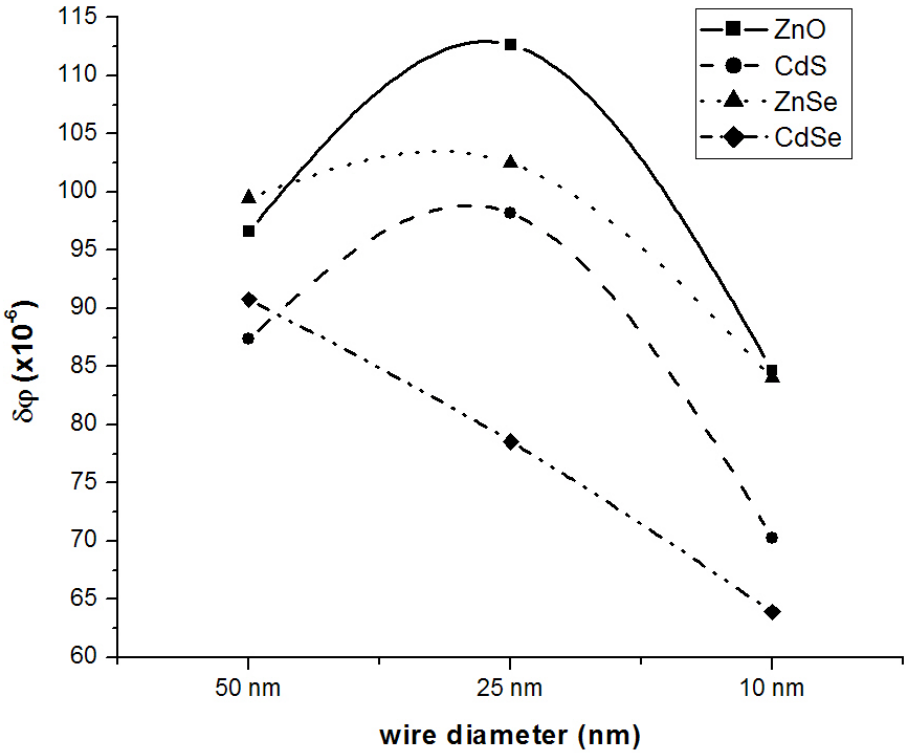

Fig. 6.7 Changes in phase shifts as function of wire diameter. The values displayed here are the changes observed at *1.2 mW* of *UV* excitation as a function of wire diameters.

Fig. 6.8 is a similar plot which depicts these size-dependent non-monotonic changes in the refractive index of the quantum wire array samples, when excited by UV pump.

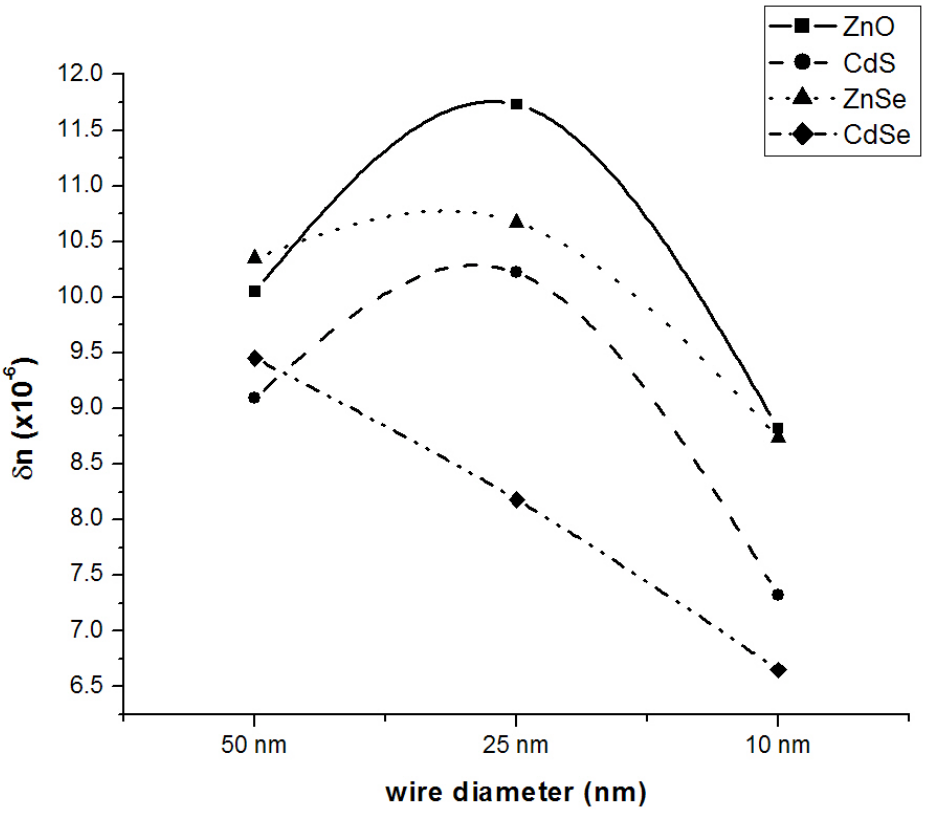

Fig. 6.8 Changes in refractive index as function of wire diameter. The values displayed here are the changes observed at *1.2 mW* of *UV* excitation as a function of wire diameters.

As can be seen in Fig. 6.7 (and 6.8), the changes in phase shifts and refractive index are very sharp in *CdS* and *ZnO* as compared to *ZnSe*, as diameter is changed from *50 to 25 nm*. This is also confirmed in Fig. 6.9, where we plot the *%*-change in the phase shifts with the wire diameters. We define a *change coefficient* η, calculated as

$$\eta(\%) = \frac{[\delta\phi(25nm) - \delta\phi(50nm)]}{\delta\phi(50nm)} \times 100 \qquad (6.9)$$

However, the actual values of the phase changes $\delta\varphi$ in *ZnSe* are comprehensively larger than those observed in *CdS*, as clearly indicated in Fig. 6.7. Therefore, although, *CdS*

shows stronger non-monotonic behavior in the phase variations as the wire diameter is reduces from *50*- to *25-nm*, the actual phase changes are larger in *ZnSe*.

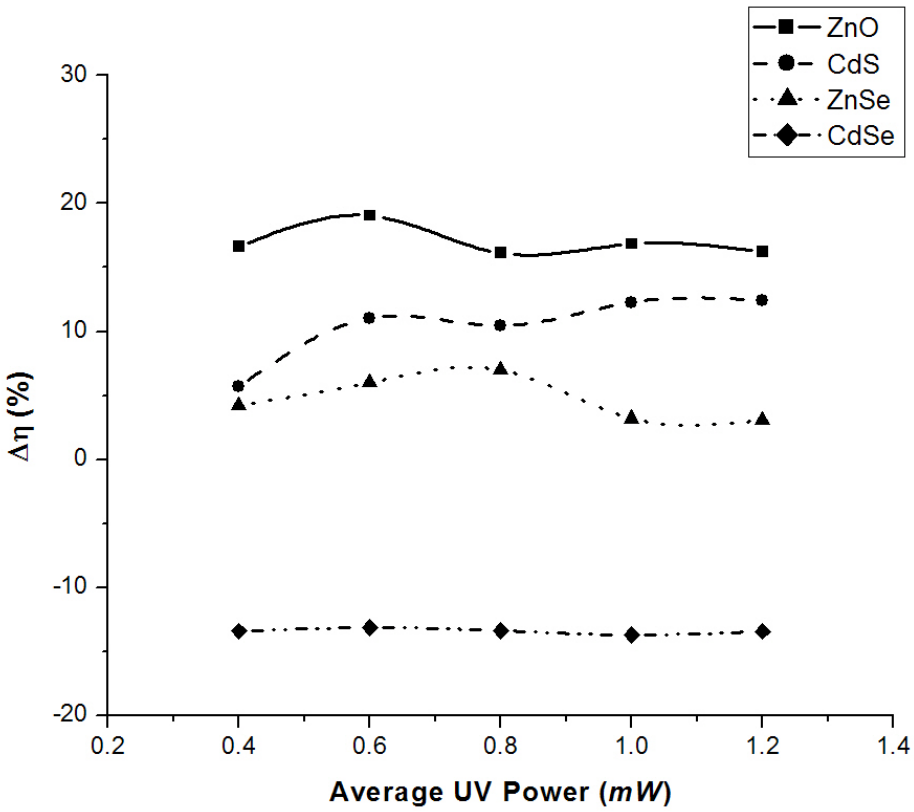

Fig. 6.8 Normalized changes in phase shifts $\Delta\eta$. The plot shows the normalized variations in the phase changes observed by *25-nm* diameter samples as compared to *50-nm* diameter samples, for all four materials, as a function of *UV* Power. $\Delta\eta$ values are calculated as $\%\left[\delta\varphi(25)-\delta\varphi(50)\right]/\delta\varphi(50)$

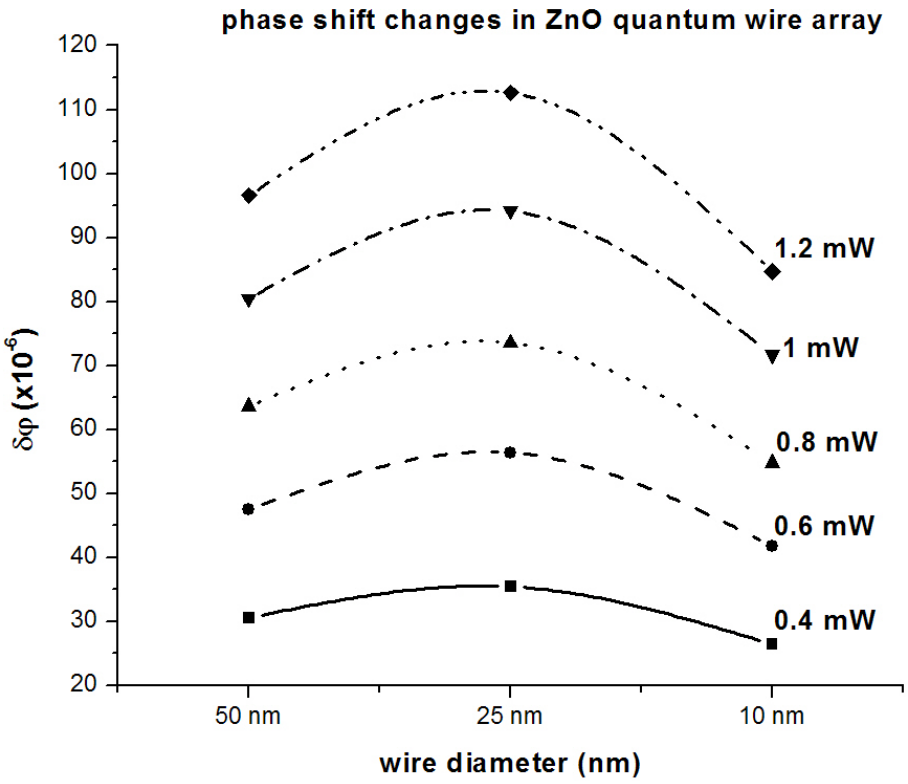

Fig. 6.10 Changes in phase shifts vs wire diameters as a function of *UV* excitation power in *ZnO* quantum wire array.

Fig 6.10 shows the phase shift variations $\delta\varphi$ as a function of wire diameter in *ZnO* for various *UV* excitations. We can observe a fairly uniform increase in the changes in phase shifts $\delta\varphi$ at all diameters, including *25 nm* sample. The changes $\delta\varphi$ do not reach saturation, which would have compressed the curves in Fig. 6.10, i.e. the separation between the curves would have gradually decreased with every (or higher) increment(s) of the *UV* excitation. The saturation could also have been indicated in Fig. 6.9, if all (or any) of the curves had demonstrated a downward trend, or even flattened ends. Although

fig. 6.9 shows a very slight decrease at higher *UV* intensities in *ZnSe*, the possibility of saturation cannot be concluded due to the extremely small values (however almost constant) of the percent variations in the changes in phase shifts $\delta\varphi$. The lack of any saturation phenomenon in the samples verifies the absence of an absolute phase space filling effect, as explained in the last section. The phase space filling, which has a damping effect on the coulomb interaction potentials and the oscillator strengths, is definitely not dominant in our samples, not even at highest *UV* intensities for narrowest wires. Note here that even the unexcited nanowires have a large carrier density background (~10^{18}-10^{19} /cm^3) due to an unintentional doping of the wire materials on account of a high interface state density, ~10^{13} /cm^2 [106]. More and more states are being filled as the UV intensity is increased, but that all the states are not completely filled to display saturation.

Fig. 6.11 shows the normalized phase shift variations as a function of *UV* intensity for the *25*- and *10-nm* wire diameters, where we plot,

$$\Delta\eta = \frac{\left[\delta\varphi(25nm) - \delta\varphi(10nm)\right]}{\delta\varphi(25nm)} \times 100 \qquad (6.10)$$

The separation between the *CdSe* and ZnSe curves and the curves for *CdS* and *ZnO* is distinctly visible. Although some variations are observed in the samples, they are small, and only appear larger being displayed on a small scale.

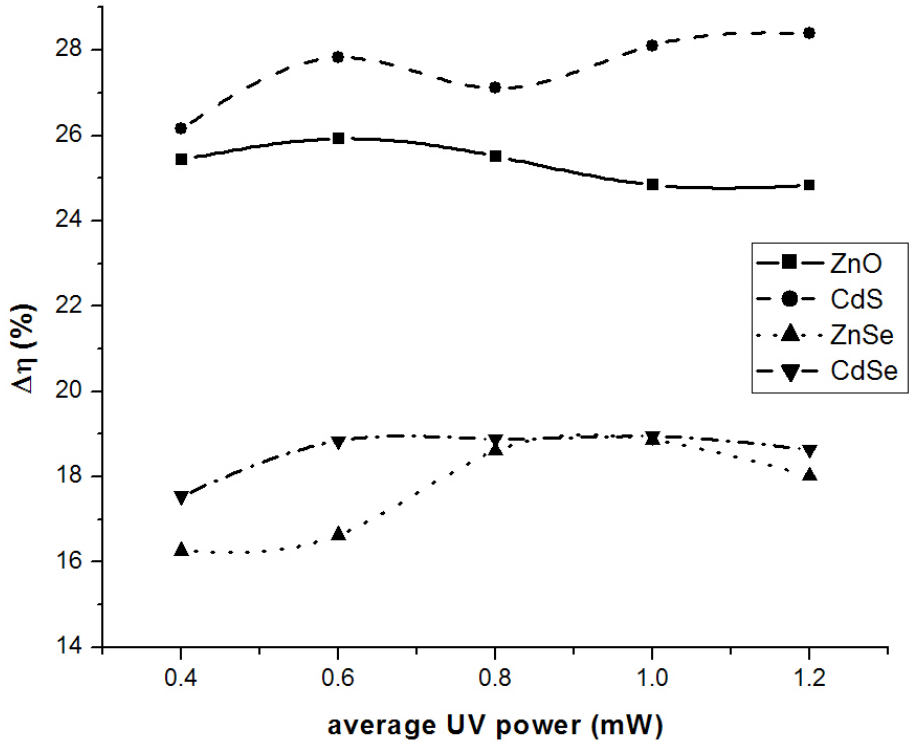

Fig. 6.11 The normalized changes in phase shifts Δη observed by *10-nm* diameter samples as compared to 25- *nm* diameter samples, for all four materials, as a function of *UV* Power. Δη values are calculated as $\%\left[\delta\varphi(25)-\delta\varphi(10)\right]/\delta\varphi(25)$.

A sharp increase in the activity (or absorption) by the *ZnO, CdS* and *ZnSe* quantum wire arrays as the wire diameter is reduced from *50 nm* to *25 nm* is attributed to the changes in the density of states function with the reduction in wire diameter. The joint density of states (DOS) function in quantum wires is given as,

$$DOS^{1D}(E)=\frac{L}{\pi}\left(\sqrt{\frac{2m_r}{\hbar^2}}\right)\sum_{n,p}\frac{1}{\sqrt{E-\varepsilon_{n,p}}}\Theta\left(E-\varepsilon_{n,p}\right) \tag{6.9}$$

where L is the wire length, m_r is reduced effective mass, Θ is the Heaviside unit step function and $\varepsilon_{n,p}$ are the intersubband transition energies. The increase in optical absorption in narrower wires (ZnO / CdS / ZnSe) is attributed to blue shifts in $\varepsilon_{n,p}$ caused by additional quantum confinement, leading to an increase in the DOS function. This is depicted in Fig. 6.12.

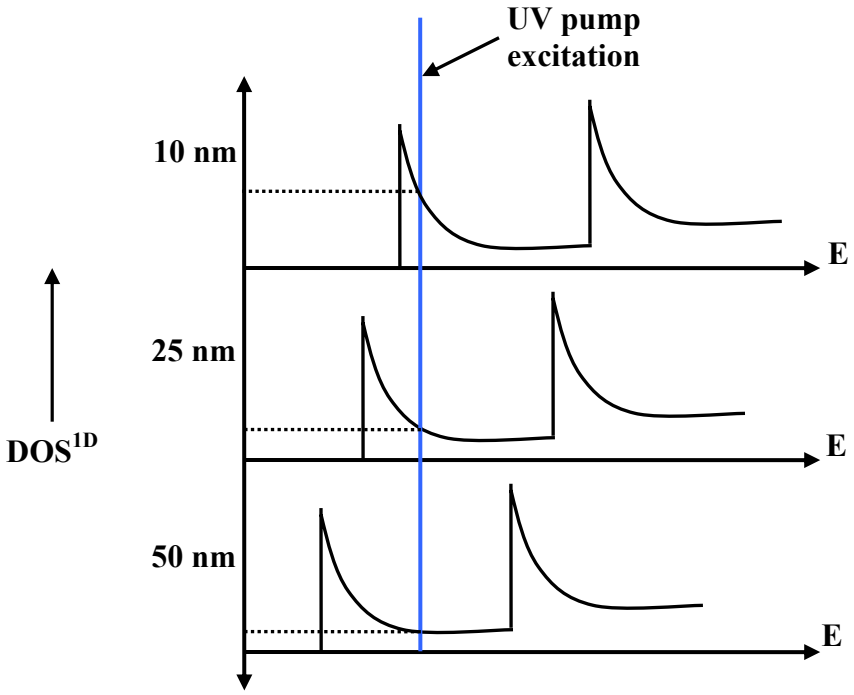

Fig. 6.12 1-dimensional density of states as a function of wire diameter.

While the rapidly decreasing filling factor acts to reduce the optical activity in narrower wire arrays, the shifting of the DOS function with additional confinement serves to increase it. It is these competing effects that give rise to the size-dependent non-

monotonic optical activity experimentally observed in CdS / ZnO / ZnSe nanowire arrays, as shown in Fig. 6.7 and 6.8.

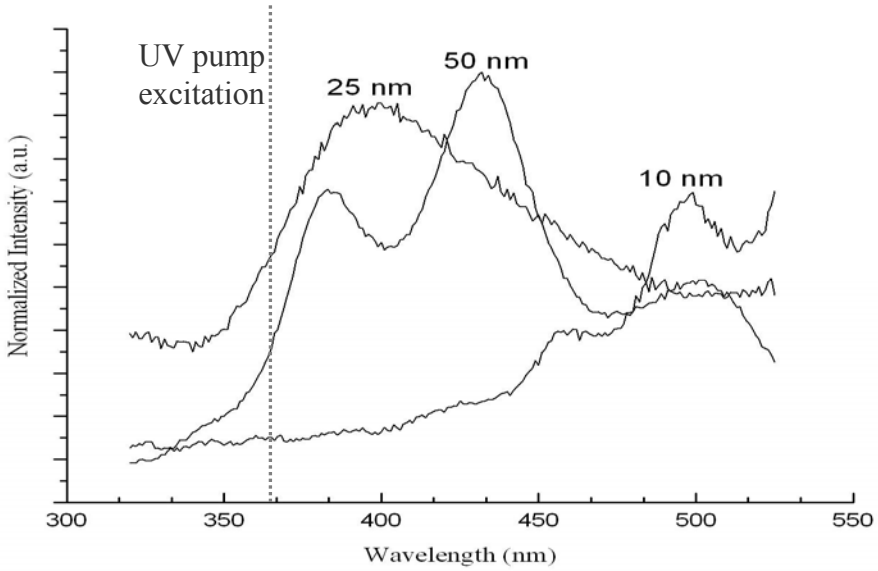

Fig. 6.13 PL spectra of ZnO quantum wire array [139]

ZnO nanowires are a special case in our experiments as ZnO bandgap energy (3.35 eV in bulk) is very close the UV pump excitation energy (3.4 eV). As shown in Fig. 6.12, since pump excitation wavelength is very close to the exciton peaks in ZnO [139], the increased optical activity may also be due to the enhancement in the excitonic effects due to progressively stronger quantum confinement effects in narrower wires, as explained in section 6.1.7. This quantum confinement effect becomes more dominant when confined dimensions (radius of the wires in this case) become comparable to the exciton Bohr radius in bulk. But as we have calculated in Table 3 and Table 5 in Ch. 3, the bulk exciton Bohr radius of *ZnO* is *4.7* nm which is still very small as compared to the actual

wire diameter (*25 nm*). However, it has already been reported for the electrochemically self-assembled quantum dots formed in porous alumina that the active size of the dots is considerably smaller than that shown by the *TEM* images [140]-[142]. This reduction in effective diameter is attributed to the side depletion of the dots caused by *Fermi* level pinning due to the presence of interface states. As mentioned in the previous section, the *Fermi* level pinning causes a natural depletion of the quantum wire semiconductor material. Bandyopadhyay [140] reported a *~7 nm* side depletion which reduces the *CdS* quantum dot diameter from *~13 nm* (*±1 nm*) to a mere *6 nm*. Balandin [141] also reported the side depletion to reduce the dot diameter from *~10 nm* to *~3.8 nm*. More recently, similar reduction in the active wire diameter as compared to the *TEM* images are also reported in *ZnO* and *CdS* quantum wires in [129] and [142], where side depletion accounts for the reduction from *25 nm* diameter to *6.8 nm*. This side depletion is a plausible explanation for the strong quantum confinement effect in ZnO. As the effective wire diameter is now comparable to the exciton Bohr radius in the bulk, a strong confinement considerably enhances the exciton binding energy and the oscillator strength, which is reflected in the enhanced phase shift changes as the ZnO wire diameter is decreased from *50 nm* to *25 nm*.

Unlike *CdS*, *ZnO* and *ZnSe*, however, quantum wires made of *CdSe* show a complete absence of size-dependent non-monotonic optical activity. More research is needed to find out the plausible explanation for this completely different behavior of CdSe wire array as compared to the rest of the wires we tested.

6.3 Mathematica and HFSS output

In this section, we connect the experimental and theoretical analysis, i.e. the generated experimental outputs are obtained in the electromagnetic wave simulator using the optical parameters calculated by solving the theoretical models in Mathematica. Using a pump-probe excitation scheme in a Michelson interferometer, the amplitudes of the *ac* component of the output is converted into corresponding phase shift changes induced by the quantum wire array when excited by *UV* light. To match the experimental outputs and the theory, these exact same phase shift changes are then re-created in *HFSS* simulation environment. As explained in Chapter 3, theory developed to model the quantum wire array is utilized to generate the permittivity and loss tangent values for various quantum wire materials at *1308 nm*, which are incorporated into *HFSS*. The *UV* excitation creates photo-generated carriers which effectively change the optical behavior of the array, i.e. its permittivity. In Mathematica, we change a fitting parameter, effectively the carrier concentration values, which generate the excited values of the permittivity of the quantum wires. These changed values of permittivity are then incorporated in *HFSS* so as to obtain the exact same phase shift changes observed experimentally.

The quasi Fermi levels (QFL) inside the quantum wires are redistributed due to the photogenerated carriers in the presence of the UV pump. We use these QFLs as adjustable parameters in our theoretical analysis to obtain the changes in the permittivity of the individual quantum wires. The electromagnetic wave simulations are then performed for the nanowire arrays to match the simulated phase shift changes (using the changed model values of the individual wire permittivities) with the experimentally

observed non-uniform phase shift changes of Fig. 6.3 – 6.6. The electromagnetic wave simulations accurately take into account the material parameters, the true filling factor, and the exact field distributions in the nanowire array structures to obtain its optical response.

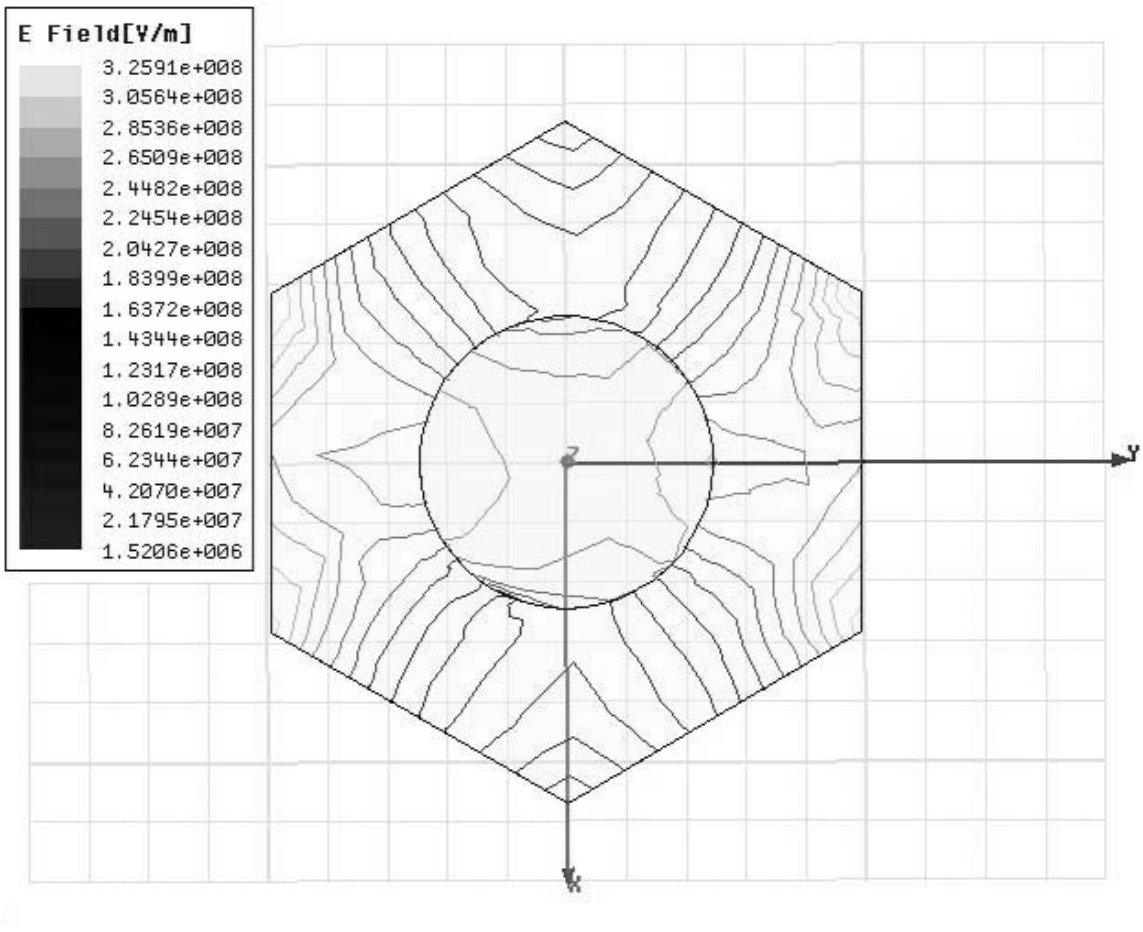

Fig. 6.14 Electric field distribution inside the unit cell of a *50-nm* diameter *CdS* nanowire array structure. Circular semiconductor wire is embedded inside the hexagonal alumina.

Fig 6.14 depicts the electric field distribution in a hexagonal unit cell of the 50-nm diameter CdS array structure. Since field lines generally concentrate in materials with higher permittivity, we can see that the field flux is stronger outside the wires, since the

permittivity of subject semiconductors is smaller than that of alumina. The simulation results show a rapid increase in the changes in effective permittivity values of the individual quantum wires as diameter decreases. The increase in quantum wire permittivity at *1.2 mW* of *UV* pump power is shown in Fig. 6.15. Changes in the real part of the permittivity in *10-nm* diameter wires are approximately 8-10 times larger than those in *50-nm* diameter wires.

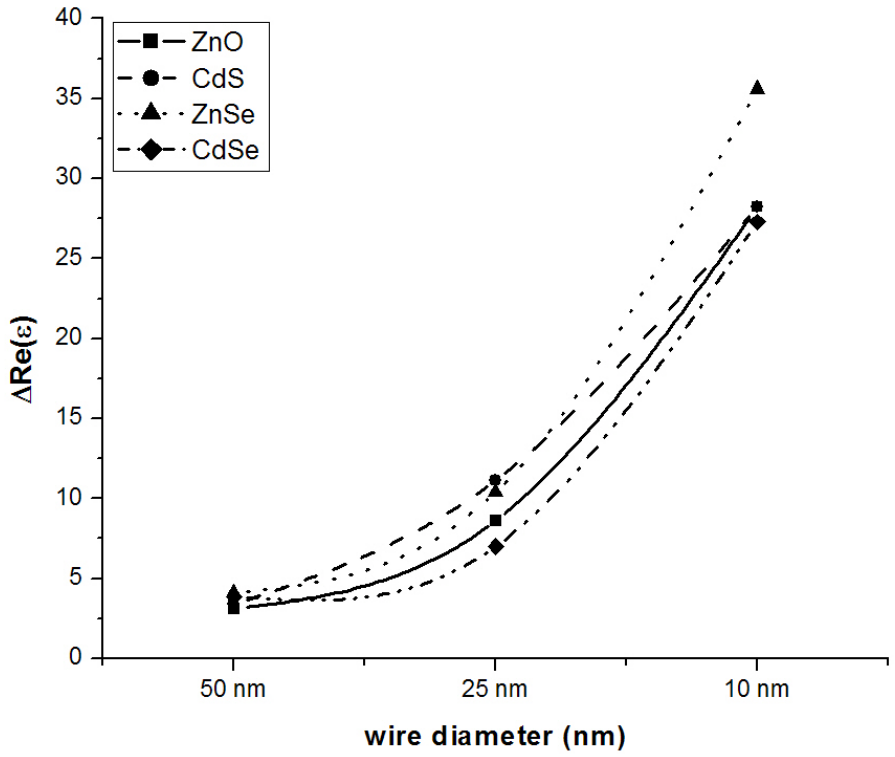

Fig. 6.14 Changes in the real part of permittivity $\Delta\mathrm{Re}(\varepsilon)$ of the quantum wire as calculated using *HFSS* to match experimentally observed phase shift changes at *1.2 mW* of *UV* pump power.

Tables 12-13 give the changes in the real part of permittivity ΔRe(ε) calculated in *HFSS* and the refractive index Δn and absorption coefficient Δα as calculated in Mathematica for the *CdS/CdSe/ZnO/ZnSe* quantum wires as a function of *UV* intensity.

	UV	Wire diameters and optical parameters								
		ΔRe(ε) (×10^{-6})			Δα /cm (×10^{-6})			Δn (×10^{-6})		
	(mW)	50nm	25nm	10nm	50nm	25nm	10nm	50nm	25nm	10nm
CdS	0.2	*0.42*	*1.44*	*3.68*	*4.25*	*14.69*	*36.9*	*0.09*	*0.32*	*0.82*
	0.4	*1.02*	*3.25*	*8.82*	*10.42*	*32.96*	*87.97*	*0.22*	*0.71*	*1.94*
	0.6	*1.6*	*5.14*	*13.13*	*16.03*	*52.03*	*130.84*	*0.34*	*1.12*	*2.89*
	0.8	*2.13*	*6.91*	*18.07*	*21.64*	*69.9*	*180.42*	*0.46*	*1.5*	*3.99*
	1.0	*2.75*	*9.08*	*23.08*	*27.66*	*91.74*	*230.74*	*0.59*	*1.97*	*5.10*
	1.2	*3.38*	*11.1*	*28.23*	*34.07*	*112.4*	*282.56*	*0.73*	*2.41*	*6.25*
CdSe	0.2	*0.5*	*1*	*3.99*	*5.6*	*11.21*	*43.19*	*0.1*	*0.204*	*0.847*
	0.4	*1.2*	*2.21*	*8.74*	*13.41*	*24.74*	*94.54*	*0.242*	*0.45*	*1.855*
	0.6	*1.93*	*3.52*	*13.69*	*21.56*	*39.35*	*148.1*	*0.389*	*0.717*	*2.907*
	0.8	*2.54*	*4.6*	*17.89*	*28.35*	*51.31*	*193.5*	*0.511*	*0.934*	*3.798*
	1.0	*3.23*	*5.82*	*22.63*	*35.99*	*64.59*	*244.8*	*0.648*	*1.17*	*4.804*
	1.2	*3.87*	*7*	*27.3*	*43.12*	*77.88*	*295.3*	*0.777*	*1.42*	*5.796*

Table 12 Changes in the optical parameters as calculated in HFSS and Mathematica for CdS and CdSe quantum wires

Material	UV	Wire diameters and optical parameters								
		ΔRe(ε) (×10^{-6})			Δα/cm (×10^{-6})			Δn (×10^{-6})		
	(mW)	50nm	25nm	10nm	50nm	25nm	10nm	50nm	25nm	10nm
ZnO	0.2	0.46	1.33	4.09	6.4	7.03	56.583	0.119	0.345	1.07
	0.4	0.98	2.71	8.81	13.64	18.55	122.02	0.253	0.704	2.31
	0.6	1.53	4.31	13.92	21.28	37.78	193.23	0.395	1.12	3.65
	0.8	2.04	5.62	18.26	28.4	60.11	253.27	0.528	1.46	4.79
	1.0	2.59	7.2	23.9	36.04	78.34	331.8	0.67	1.87	6.27
	1.2	3.1	8.61	28.23	43.16	120.05	391.46	0.802	2.24	7.4
ZnSe	0.2	0.54	1.5	4.97	3.92	10.79	35.49	0.11	0.31	1.04
	0.4	1.22	3.12	11.03	8.84	22.58	78.97	0.25	0.64	2.31
	0.6	1.92	4.99	17.36	13.76	36.13	123.97	0.39	1.03	3.63
	0.8	2.57	6.73	22.85	18.5	48.32	163.03	0.52	1.38	4.78
	1.0	3.35	8.48	28.73	24.06	60.96	204.98	0.68	1.74	6.01
	1.2	4.12	10.4	35.6	29.62	74.78	253.97	0.84	2.13	7.44

Table 13 Changes in the optical parameters as calculated in HFSS and Mathematica for ZnO and ZnSe quantum wires

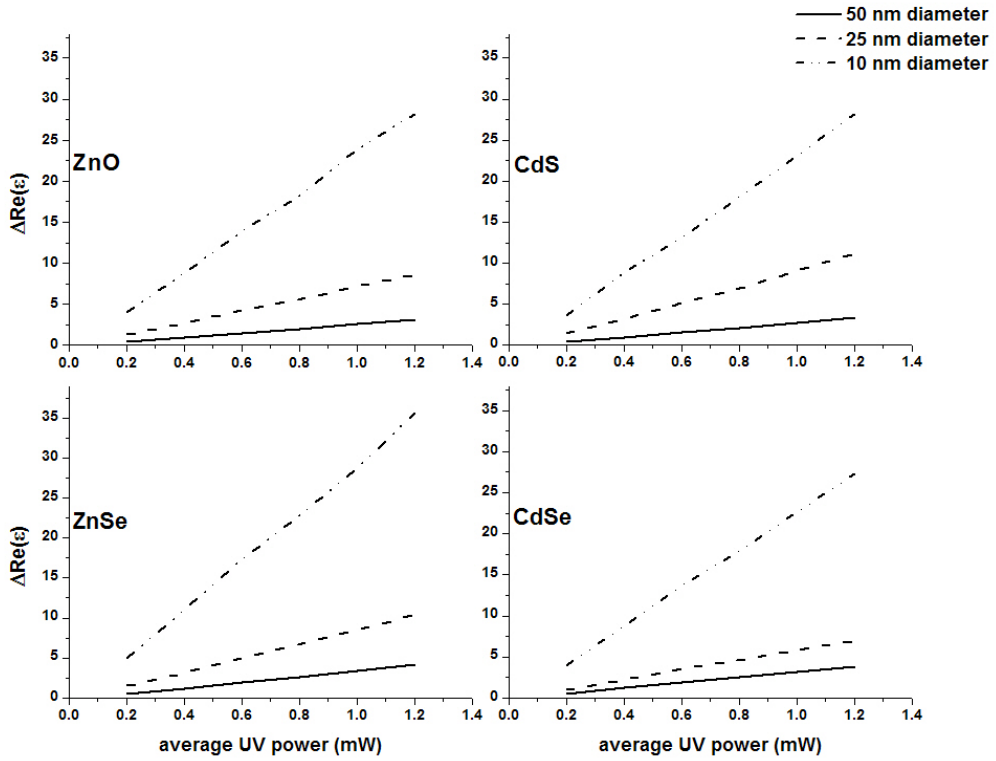

Fig 6.16 Changes in the real parts of permittivity of all quantum wires at various UV pump powers as calculated using experimental data and *HFSS*

Fig. 6.16 shows the permittivity change observed in all the quantum wires for various *UV* intensities. Note that these changes in the permittivity are with respect to their corresponding values in un-excited quantum wires. Fig. 6.17 shows the theoretically calculated variations in the real and imaginary parts of the permittivity of the quantum wires at 1308 nm as a function of their diameters in the absence of UV excitation. Both real and imaginary parts of the permittivity progressively decrease as the wire diameter is reduced.

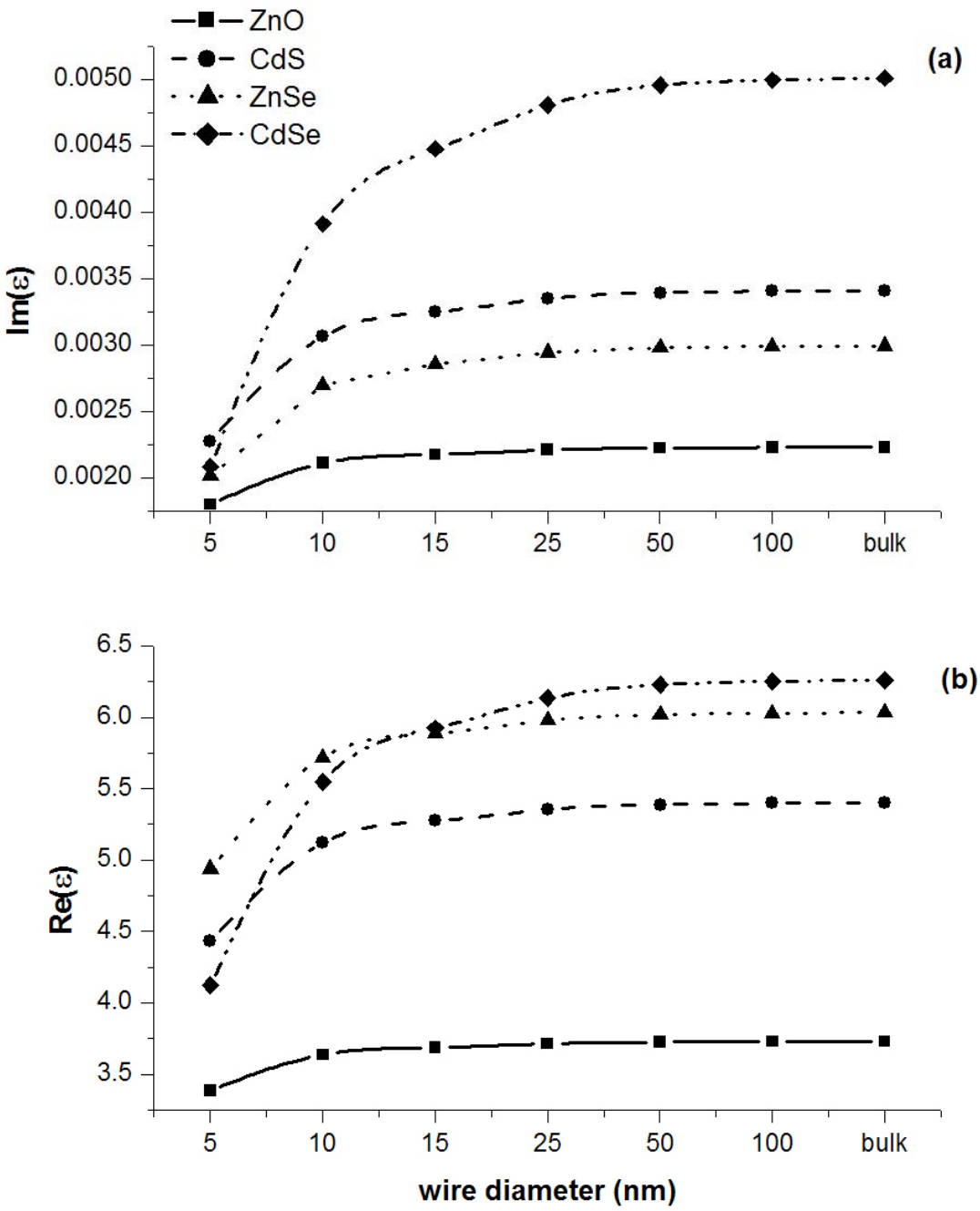

Fig. 6.16 Variations in the theoretically calculated (a) real and (b) imaginary parts of the permittivity (ε) as functions of quantum wire diameter in the absence of pump.

The size dependence of the (unpumped) permittivity in low-dimensional semiconductors is well known. The theoretical treatment of the size dependence of the permittivity in quantum wells, wires and dots indicate the reduction in the value of the permittivity with the increase in quantum confinement [143]-[147]. A significant reduction in the permittivity is reported in the low-dimensional structures when the confinement is of the order of few nanometers, comparable to the Bohr radius in the semiconductor materials. We also observe similar effects in this theoretical treatment for quantum wires. According to Fig. 6.16, there is an extremely small reduction in the dielectric permittivity in thick wires. The reduction, however, becomes sharper in CdS, ZnSe and CdSe quantum wires below approximately 10 nm, which is close to the Bohr diameter for these materials (7.65-, 7-nm and 9-nm respectively). The bulk Bohr diameter is 4.6 nm in ZnO, below which its permittivity is expected to decrease sharply.

CHAPTER 7

Summary and Conclusions

In this work, we have investigated the optical behavior of the quantum wires array when excited by a stationary high energy *UV* light. The quantum wires are fabricated by selectively electrodepositing the semiconductor material in electro-chemically self-assembled porous alumina templates. The quantum wires are very distinct in their optical behavior amongst the low-dimensional structures on account of a very peculiar nature of their density of states. It has very sharp peaks which diverge at the bottom of each sub-band. This gives rise to an enhanced binding energy and oscillator strength of excitons, and potentially to stronger optical absorption. Although all types of transitions like free carrier transitions, band-to-band transitions, exciton transitions, impurity-to-band transitions etc. take place, the effects we observed are more dominated by band-to-band transitions and exciton transitions.

We developed a theoretical model to calculate the optical response of the quantum wire arrays to a *UV* excitation. The *UV* excitation light is modulated at *1 KHZ* frequency; hence the excitation time is very large compared to the carrier scattering and recombination times. Therefore, the photo-generated carriers have sufficient time to reach thermal equilibrium amongst themselves within their respective bands, although the

complete structure is out of thermodynamic equilibrium. This gives rise to a quasi-equilibrium regime. We derived a polarization equation which is solved numerically to calculate the bound state (exciton) and continuum state solutions at very low or virtual zero excitation. We also derive the solutions for higher excitation, which is still smaller than required to generate the carrier density exceeding the Mott density. The solutions are generated by taking into account the effects of screening, Coulomb interaction between the carriers as well as the many body effects on the excitons. A program is developed in Mathematica to solve these complex set of equations iteratively using an Accelerated Fixed Point (AFP) method. The real and imaginary parts of the theoretically calculated permittivity progressively decrease as the wire diameter is reduced. The optical parameters generated for individual quantum wires are then incorporated into an electromagnetic wave simulator, *HFSS*, to investigate the behavior of an array of wires. In *HFSS*, a unit cell consists of a single *1 micron* long quantum wire embedded in a hexagonal alumina material. This unit cell is replicated with a desired periodicity so as to generate a *2-dimensional* array structure identical to the actual quantum wire array. We have used four different types of quantum wire materials, namely *CdS, ZnSe, ZnO* and *CdSe*. Each type is investigated for three different wire diameters, i.e. *50, 25* and *10 nm*. The Mathematica and *HFSS* models are developed for each of these types.

Our experimental setup consists of a pump-probe excitation scheme in a Michelson interferometer. The interferometer is constructed using *1308 nm IR* laser, which correspond to *0.95 eV* of optical energy. As band gap of all the quantum wire semiconductor materials is much larger than this energy, the quantum wires are

completely transparent to *IR* laser, which is used as a probe. A Nichia *LED* is used as a source of *UV* light at *365 nm* wavelength (*3.4 eV*). As this pump energy is higher than the band gap of the wire materials, electron-hole pairs are generated which effectively alter the optical behavior of the array. This changes the probe beam intensity (due to change in absorption coefficient of the sample) and the phase difference of the interfering beams (on account of the changes in actual path difference due to a changed refractive index of the sample). However, due to the direct dependence of the absorption coefficient on the extremely short length of the wires as well as very small filling factor, the change in beam intensity is too small to be detected. But the change in the phase difference induced due to *UV* excitation is effectively amplified due to its inverse dependence on the wavelength of light, which is extremely small. Therefore, we are able to experimentally measure the changes in the phase difference of the interfering beams, which constitutes a direct measure of the changes in refractive index. As the UV is modulated at *1 KHz* frequency, any *1 KHz ac* component present at output of the Michelson interferometer has to be due to the perturbation caused by *UV* light. The interference curve is biased halfway between its minima and maxima, where the slope of the curve and hence the output of the interferometer is almost uniform. As the slope is also maximum there, this biasing makes the interferometer extra-sensitive to any small perturbations. The generated *ac* component is captured using a combination of *RC* filter and a lock-in amplifier, which is numerically converted in terms of a change in phase difference.

We observe a very strong size-dependent non-monotonic optical behavior of the *ZnO, CdS* and *ZnSe* quantum wires. As the diameter of the wires reduces, their optical activity

was also expected to reduce monotonically on account of the reduced amount of optically active material in the narrow wires. However, as the wire diameter is reduced from *50-nm* to *25-nm*, the optical activity is actually found to increase substantially. Array optical activity further reduces as the wire diameter is reduced to *10-nm* creating a hump shaped (non-monotonic) characteristic. This size-dependent non-monotonic behavior is attributed to two major competing physical effects: the classical filling factor effect and the quantum confinement effect in the 1-dimensional density of states function with the reduction in wire diameter.

The increase in optical absorption in narrower wires is attributed to blue shifts in the inter-subband energies caused by additional quantum confinement, leading to an increase in the joint DOS function. On the other hand, since the filling factor, a measure of optically active material present in the arrays, decreases with narrower quantum wires, the optical activity progressively reduces. While the decreasing filling factor acts to reduce the optical activity in narrower wire arrays, the shifting of the DOS function with additional confinement serves to increase it. These competing effects give rise to the size-dependent non-monotonic optical activity experimentally observed in the nanowire arrays. In case of ZnO, where the pump excitation energy is very close to the exciton peaks, the enhancement in the excitonic effects due to progressively stronger quantum confinement effects in narrower wires may also contribute to the increased optical activity. Unlike *CdS*, *ZnO* and *ZnSe*, however, quantum wires made of *CdSe* show a complete absence of such non-monotonic optical activity. More research is needed to find out the plausible explanation for this completely different behavior of CdSe wire array as

compared to the rest of the wire material arrays we tested. Note here that due to the presence of interface states, there is a formation of depletion region inside the semiconductor material on account of *Fermi* level pinning, and hence the actual effective wire diameter is smaller than that shown in the SEM pictures of the array structures.

Since the probe beam size samples the optical behavioral changes in a large number of quantum wires induced by the *UV* excitation, some important local effects might have been averaged out. A smaller beam size might be used to give better understanding of more local optical phenomenon. The large changes observed in the permittivity for arrays with intermediate wire diameter sizes may be suitable for optical phase shifting, intensity modulation, and switching applications.

List of References

[1] J. Nagle, C. Weisbuch, *" Science and Engineering of 0 and 1 Dimensional Semiconductor Systems*". New York : Plenum, 1990**.**

[2] H. Sakaki, "*Scattering Suppression And High-Mobility Effect Of Size Quantized Electrons In Ultrafile Semiconductor Wire Structures*", Japanese Journal of Applied Physics, Vol. 19, No. 12, pp. L735-738, 1980.

[3] P. M. Petroff, A. C. Gossard, R. A. Logan and W. W. Wiegmann, "*Toward quantum well wires: Fabrication and optical properties*", Applied Physics Letters, Vol. 41, No. 7, pp. 635-638, 1982.

[4] C. M. Lieber, "*Nanoscale Science and Technology: Building a Big Future from Small Things*", MRS Bulletin, Vol. 28, pp. 486-491, 2003.

[5] Jianfang Wang, Mark S. Gudiksen, Xiangfeng Duan, Yi Cui, and Charles M. Lieber, "*Highly Polarized Photoluminescence and Photodetection from Single Indium Phosphide Nanowires*", Science, Vol. 293, pp. 1455-1457, 2001**.**

[6] X. F. Duan, Y. Huang, Y. Cui, J. Wang, C. M. Lieber, "*Indium phosphide nanowires as building blocks for nanoscale electronic and optoelectronic devices*", Nature, Vol. 409, pp. 66-69, 2001.

[7] X. F. Duan, Y. Huang, R. Agarwal, C. M. Lieber, "*Single-nanowire electrically driven lasers*", Nature, Vol. 421, pp. 241-245, 2003.

[8] J.C. Johnson, H. Yan, P. Yang, and R.J. Saykally, "*Optical Cavity Effects in Single Zinc Oxide Nanowire Lasers and Waveguides*" Journal of Physical Chemistry B, Vol. 107, pp. 8816-8828, 2003.

[9] A. V. Maslov and C. Z. Ning, "*Reflection of guided modes in a semiconductor nanowire laser*", Applied Physics Letters, Vol. 83, No. 6, pp. 1237-1239, 2003.

[10] J.C. Johnson, H.-J. Choi, K.P. Knutsen, R.D. Schaller, P. Yang, and R.J. Saykally, "*Single Gallium Nitride Nanowire Lasers*", Nature Materials, Vol.1, No. 2, pp. 106-110 2002.

[11] Michael H. Huang, Samuel Mao, Henning Feick, Haoquan Yan, Yiying Wu, Hannes Kind, Eicke Weber, Richard Russo, and Peidong Yang, "Room-Temperature Ultraviolet Nanowire Nanolasers", Science, Vol. 292, pp. 1897-1899, 2001.

[12] J. A. Zapien, Y. Jiang, X.M. Meng, W. Chen, F.C.K. Au, Y. Lifshitz, and S.T. Lee, "*Room temperature single nanoribbon lasers*", Applied Physics Letters, Vol. 84, No. 7, pp. 1189-1191, 2004.

[13] X. Bai, K. Lewis., C. Kurdak, M. Msall, S. Ghos, S. Krishna, P. Bhattacharya, abstract # S22.013, American Physical Society, Annual APS Meeting, 2003.

[14] D. Borca-Tasciuc, G. Chen, A. Prieto, M. Martin-GonzalezA. Tacy, T. Sands, M. Ryan, J. Fleurial, "*Thermal properties of electrodeposited bismuth telluride nanowires embedded in amorphous alumina*", Applied Physics Letters, Vol. 85, pp. No. 24, pp. 6001-6003, 2004.

[15] O. Jessenskey, F. Muller and U. Gosele, "*Self organized formation of hexagonal pore arrays in anodic alumina*", Applied Physics Letters, Vol. 72, No. 10, pp. 1173-1175, 1998.

[16] L. Menon, "*Quantum dots and nanowires*", edited by S. Bandyopadhyay and H. S. Nalwa, American Scientific, 2003, Steven Ranch, CA, 2003.

[17] B. E. Collins, K.P.S. Dancil, G. Abbi, and M.J. Sailor, "*Determining Protein Size Using an Electrochemically Machined Pore Gradient in Silicon*", Advanced Functional Materials, Vol. 12, No. 3, pp. 187-191, 2002.

[18] L. M. Karlsson, P. Tengvall, I. Lundström, and H. Arwin, "*Adsorption of human serum albumin in porous silicon gradients*", physica status solidi (a), Vol. 197, Issue 2, pp. 326-330, 2003.

[19] L.M. Karlsson, R. Tengvall, I. Lundstrom and H. Arwin, "*Penetration and loading of human serum albumin in porous silicon layers with different pore sizes and thicknesses*", Journal of Colloid and Interface Science, Vol. 266, Issue 1, pp. 40-47, 2003.

[20] Seigo Kodera, Toshihide Okajima, Hidehiko Iwabuki, Daisuke Kitaguchi, Shunichi Kuroda, Tatsuo Yoshinobu, Katsuyuki Tanizawa, Masamitsu Futai and Hiroshi Iwasaki, **"***Detection of protein–protein interactions on SiO_2/Si surfaces by spectroscopic ellipsometry*", Analytical Biochemistry, Vol. 321, issue 1, pp. 65-70, 2003.

[21] N. Koulin, L. Menon, A. Z. Wong, D. W. Thompson, J. A. Woolam, P. F. Williams and S. Bandyopadyay, "*Giant Photoresistivity and optically controlled switching in self-assembled nanowires*", Applied Physics Letters, Vol. 79, No. 26, pp. 4423-4425, 2001.

[22] S. Bandyopadhyay, and A. E. Miller, in *"Handbook of advanced electronic and photonic materials and devices*", edited by H. S. Nalwa, Vol. 6, CH. 1, pp. 1-27, Academic press, San Diego, 2000

[23] M. Moscovitz, U.S. Patent 5, 202, 290, 1993.

[24] D. AlMawlawi, N. Coombs and M. Moskovitz, "*Magnetic properties of Fe deposited into anodic aluminum oxide pores as a function of particle size*", Journal of Applied Physics, Vol. 70, Issue 8, pp. 4421-4425, 1991.

[25] R. Karmhag, T. Tesfamichael, E. Wachelgard, G.A. Nicklasson, M. Nygren, "*Oxidation Kinetics of Nickel Particles: Comparison Between Free Particles and Particles Embedded in a Dielectric Matrix*", Solar Energy, Vol. 68, pp. 329-333, 2000.

[26] G. Che, B.B. Lakshmi, C.R. Martin, E.R. Fisher, R.S. Ruoff, "*Chemical Vapor Deposition (CVD)-Based Synthesis of Carbon Nanotubes and Nanofibers Using a Template Method* **",** Chemistry of Materials, Vol. 10, No. 1, pp. 260-267, 1998.

[27] K. Nielsch, R.B. Wehrspohn, J. Barthel, J. Kirschner, K. Schwirn, U. Gosele, S. "*Fischer, H. Kronmuller, Hexagonally ordered 100 nm period nickel nanowire arrays*" Applied Physics Letters, Vol. 79, Issue 9, pp. 1360-1362, 2001.

[28] L. Ward, in *Handbook of Optical Constants of Solids II*, edited by E..D. Palik, Academic Press, Boston, 1991.

[29] I Broser, Ch. Fricke, B. Lummer, R. Heitz, H. Pearls, and A. Hoffman, "*Optical nonlinearity and fast switching due to birefringence and mode coupling in CdS crystals",* Journal of. Crystal Growth, Vol. 117, pp. 788-792, 1992.

[30] A. Yoshikawa and Y. Sakai, "*High efficiency n-CdS/p-InP solar cells prepared by the close-spaced technique"***,** Solid State Electronics, Vol. 20, Issue 2, pp. 133-134, 1977.

.

[31] K. Nakao and A. Ishibashi, in *Procss of wide band-gap II-VI semiconductors*, EMIS data-reviews series No. 17, edited by R. Bhargava (INSPEC (IEE)), London, 1997.

[32] G. D. Studtmann, R.L. Gunshor, L.A. Koloddzieski, M.R. Melloch, J.A. Cooper, R.F. Pierret, D.F. Munich, C. Choi, and N. Otsuka, Appl. Phys. Lett. 60, 192, 1992.

[33] T. Saiki, K. Takeuchi, M. Kuwata-Gonokami, T. Mitsuyu, and K. Ohkawa, "*Giant nonlinear phase shift at exciton resonance in ZnSe",* Applied Physics Letters, Vol. 60, Issue 2, pp.192-194, 1992.

[34] J.A. Arnowich, D. Golmayo, A.L. Fahrenbrunch, and r.H. Bube, "*Photovoltaic properties of ZnO/CdTe heterojunctions prepared by spray pyrolysis",* Jpurnal of Applied Physics, Vol. 51, Issue 8, pp. 4260-4268, 1980.

[35] S. Pizzini, N. Butta, D. Narducci, and M. Palladino, "*Thick Film ZnO Resistive Gas Sensors: Analysis of Their Stationary and Kinetic Behaviour*", Journal of The Electrochemical Society, Vol. 136, pp. 1945-1948, 1989.

[36] F.S. Hickernell, "*Zinc-oxide thin-film surface-wave transducers",* Proceedings of the IEEE, Vol. 64, pp. 631-635, 1976.

[37] T. Shiosaki, N. Kitamura, and A. Kawabata, Proceeding of the IEEE Seventh International Symposium on the Applications of Ferroelectrics, 296, 1990.

[38] D.C. Reynolds, D.C. Look, and B. Jogai, "*Optically pumped ultraviolet lasing from ZnO***"**,Solid State Communications, Vol. 99, Issue 2, pp. 873-875, 1996.

[39] R. Tenne. R. Jager-Waldau, M. Lux-Steiner, E. Bucher, J. Rioux, and C. Levy-Clement, "*Transport and optical properties of low-resistivity CdSe*", Physical Review B, Vol. 42, Issue 3, 1763-1772, 1990.

[40] S. L. Chuang, "*Physics of Optoelectronics Devices"*, A Wiley-Interscience publication, New York, 1995.

[41] Vladimir V. Mitin, Viatcheslav A. Kochelap, Michael A. Stroscio, "*Quantum Heterostructures*", Cambridge University Press, Cambridge, U.K.,1999.

[42] A. Graja, "*Low dimensional organic conductors"*, World Scientific, Singapore, 1992.

[43] B.E. A. Saleh and M.C. Teich, "*Fundamentals of Photonics*", A Wiley-interscience publication, 1991.

[44] K. Nielsch, J. Choi, K. Schwirn, R. B. Wehrspohn, U. Gosele, "*Self-ordering regimes of porous alumina: the 10% porosity rule",* Nano Letters, Vol. 2, No. 7, pp. 677-780, 2002.

[45] S. Bandyopadhyay and H.S. Nalwa, "*Quantum Dots and Nanowires*", American Scientific publishers, CA, 2003.

[46] A. Banerjee, "*Nanosynthesis using porous anodic alumina"*, M.S. Thesis, Virginia Commonwealth University, 2004.

[47] H. Masuda, K. Fukuda, "*Ordered Metal Nanohole Arrays Made by a Two-Step Replication of Honeycomb Structures of Anodic Alumina*", Science, Vol. 268, pp. 1466-1468, 1995.

[48] L. I. Schiff, "*Quantum Mechanics"* , 3rd ed., McGraw Hill, New York, 1968.

[49] A. S. Davydov, "*Quantum Mechanics"*, Pergamon, New York, 1965.

[50] Erwin Kreyszig, "*Advanced Engineering Mathematics*", 9th edition, John Wiley and Sons Inc., New York, 2005.

[51] Karl Blum, *Density Matrix Theory and Applications*, 2nd ed., Plenum Publishing Corporation, New York, 1996.

[52] Stephen Gasiorowicz, *Quantum Physics*, 2nd ed., John Wiley and Sons, Inc, 1996.

[53] H. Haug and S. W. Koch, *Quantum theory of the optical and electronic preperties of semiconductors*, 4th ed., World Scientific, 2001.

[54] L. Allen and J. H. Eberly, "*Optical resonance and two level atom"s*, Willey and Sons, New York, 1975.

[55] H. Haug, S. W. Koch, "*Semiconductor laser theory with many body effects"*, Physical Review A, Vol. 39, No. 4, pp. 1887-1898, 1988.

[56] H. Haug and D. B. Tran, "*Gain Spectrum of an e-h Liquid in Direct Gap Semiconductors***",** Physica Status Solidi (b), Vol. 98, Issue. 2, pp.581-589, 1980.

[57] M. P. Kessler and E.P. Ippen, "*Subpicosecond gain dynamics in GaAlAs laser diodes*", Applied Physics Letters, Vol. 51, Issue 22, pp. 1765-1567, 1987.

[58] R. Loudon, "*Singular potentials in one dimension*", American Journal of Physics, Vol. 44, Issue 11, pp.1064-1066, 1976.

[59] M. Lindberg and S.W. Koch, "*Effective Bloch equations in semiconductors"*, Physical Review B, Vol. 38, No. 5, pp. 3342-3350, 1988.

[60] T. Ogawa and T. Takagahara, "*Interband absorption spectra and Sommerfeld factors of a one-dimensional electron-hole system*", Physical Review B, Vol. 43, No. 17, pp. 14325-14328,1991.

[61] S. Benner and H. Haug, "*Influence of external electric and magnetic fields on the excitonic absorption spectra of quantum well wires*", Physical Review B, Vol. 47, No. 23, pp. 15750-15754, 1993.

[62] F. Rossi and E. Molinari, "*Linear properties of realisic quantum-wire structures: The dominant role of coulomb correlation"*, Physical Review B, Vol. 53, No. 24, pp. 16462-16473, 1996.

[63] C. Ell, R. Blank, S. Benner and H. Haug, "*Simplified calculations of the optical spectra of two and three dimensional laser excited semiconductors"*, Journal of Optical Society of America B, Vol. 6, No. 11, pp. 2006-2012, 1989.

[64] H. Haug and S. Schmitt-Rink, "*Electron theory of the optical properties of laser excited semiconductors"*, Progress Quantum Electronics, Vol. 9, pp. 3-100, 1984.

[65] T. Ogawa and Y. Kanemitsu, "*Optical properties of low dimensional materials"*, World Scientific, 1995.

[66] R. Loudon, "*One-Dimensional Hydrogen Atom*", American Journal of Physics, Vol. 27, Issue 9, pp. 649-655, 1959.

[67] R. J. Elliot, and R. Loudon, "*Theory of fine structure on the absorption edge in semiconductors*"' Journal of Physics and Chemistry of Solids, Vol. 8, pp. 382-388, 1959.

[68] R. J. Elliot, and R. Loudon, "*Theory of the absorption edge in semiconductors in a high magnetic field*", Journal of Physics and Chemistry of Solids, Vol. 15, Issues 3-4, pp. 196-207, 1960.

[69] S. Abe, "*Exciton versus Interband Absorption in Peierls Insulators*", Journal of the Physical Society of Japan, Vol. 58, No. 1, pp. 62-65, 1989.

[70] L. Banyai, I. Galbraith, C. Ell and H. Haug, *Excitons and biexcitons in semiconductor quantum wires*, Phys. Rev. B, Vol. 36, No. 11, pp. 6099-6104, 1987.

[71] L. Landau and E. Lifshitz*, "Quantum Mechanics"*, Pergamon, 1958.

[72] F. Madarasz, F. Szmulowicz, F.Hopkins, and D. Dorsey, Physical Review B, Vol. 49, 13528, 1994.

[73] S. Glutch, F. Bechstedt, "*Effects of the Coulomb interaction on the optical spectra of quantum wires*", Physical Review B, Vol. 47, Issue 8, pp. 4315-4326, 1993.

[74] S. Glutch, F. Bechstedt, "*Interplay of Coulomb attraction and spatial confinement in the optical susceptibility of quantum wires*", Physical Review B, Vol. 47, Issue 11, pp. 6385-6389, 1993.

[75] P. Lefebvre, P. Christol, H. Mathieu, S. Glutch, "*Confined excitons in semiconductors: Correlation between binding energy and spectral absorption shape*", Physical Review B, Vol. 52, Issue 8, pp. 5756-5759, 1995.

[76] T. Ogawa and T. Takagahara, , "*Optical absorption and Somerfield factors of one dimensional semiconductors : An exact treatment of excitonic effects"*, Physical Review B, Vol. 44, No. 15, pp. 8138-8156, 1991.

[77] A. Forshaw and D. Whittaker, "*Optical absorption of wide quantum wires"*, Physical Review B, Vol. 54, No. 12, pp. 8794-8798, 1996.

[78] S. Glutch and D. Chemla, "*Transition to one-dimensional behavior in the optical absorption of quantum-well wires*", Physical Review B, Vol. 53, Issue 23, pp. 15902-15909, 1996.

[79] M. Abramowitz and I. Stegun, "*Handbook of Mathematical functions"*, Dover, 1970.

[80] I. Gradshteyn and I. Ryzhyk, "*Table of integrals, series and products"*, Academic Press, New York, 1965.

[81] S. Benner and H. Haug, "*Plasma density dependence of the optical spectra for quasi-one-dimensional quantum well wires"*, Europhysics Letters Vol. 16, No. 6, pp. 579-583, 1991.

[82] D. Wang, S. Sarma, *Many body effects on excitonic optical properties of photoexcited semiconductor quantum wire structures*, Physical Review A, Vol. 64, 195313, pp. 1-16, 2001.

[83] H. Haug and S. Schmitt-Rink, "*Electron theory of the optical properties of laser excited semiconductors"*, Progress in Quantum Electronics, Vol. 9, pp. 3-100, 1984.

[84] Gregory B. Tait, "*Heterostructure semiconductor device analysis: A globally convergent solution method for the nonlinear Poisson equation*", Solid-State Electronics, Vol. 32, No. 5, pp. 369-376, 1989.

[85] P. Graves-Moris, *Pade approximants and their applications*, Academic Press, New York, 1973.

[86] X. F. Wang, and X. L. Lei, "*Polar-optic phonons and high-field electron transport in cylindrical GaAs/AlAs quantum wires*", Physical Review B, No. 49, Issue 7, pp. 4780-4789, 1993.

[87] Sadao Adachi, "*Optical constants of crystalline and amorphous semiconductors, Numerical data and Graphical information",* Kluwer Academic Publishers, Boston, 1999.

[88] N. K. Abrikosov, V. F. Bankina, L.V. Poretskosov, L.E. Shelimova and E.V. Skudnova, "*Semicnducting II-VI, IV-VI, and V-VI compounds*", Plenum Press, New York, 1969.

[89] S. Adachi, T. Taguchi, "*Optical properties of ZnS*", Physical Review B, Vol. 43, Issue 12, pp. 9569-9577, 1991.

[90] A. Danueville, D. Tanner, and P.H. Holloway, "*Optical constants of ZnSe in the far infrared*", Physical Review B, Issue 8, pp. 6544-6550, 1991.

[91] D. Berlincourt, H. Jaffe, and L.R. Shiozawa, "*Electroelastic Properties of the Sulfides, Selenides, and Tellurides of Zinc and Cadmium*", Physical Revie, Vol. 129, pp. 1009-1017, 1963

[92] I. Stralkowski, S. Joshi, and C.R. Crowell, "*Dielectric constant and its temperature dependence for GaAs, CdTe, and ZnSe*", Applied Physics Letters, Vol. 28, Issue 6, pp. 350-352, 1976.

[93] C. K. Yang and K.S. Dy, "*Band structure of ZnO using the LMTO method*", Solid State Communications, Vol. 88, Issue 6, pp. 491-494, 1993.

[94] Y. N. Xu and W. Y. Ching, "*Electronic, optical, and structural properties of some wurtzite crystals*", Physical Review B, Vol. 48, Issue 7, pp. 4335-4351, 1993.

[95] D. Vogel, P. Kriiger, and J. Pollmann, "*Self-interaction and relaxation-corrected pseudopotentials for II-VI semiconductors*", Physical Review B, Vol. 54, Issue 8, pp. 5495-5511, 1996.

[96] E. F. Venger, A.V. Melnichuk, L. Yu. Melnichuk, and Yu. A. Pasechnik, "*Anisotropy of the ZnO single crystal reflectivity in the region of residual rays*", Physica Status Solidi B, Vol. 188, No. 2, pp. 823-831, 1995.

[97] T. Hattori, Y. Homma, A. Mitsuishi, and M Tacke, "*Indices of refraction of ZnS, ZnSe, ZnTe, CdS, and CdTe in the far infrared*", Optics Communications, Vol. 7, Issue 3, pp. 229-232, 1973.

[98] H. W. Verlueur and A. S. Barker Jr., "*Optical Phonons in Mixed Crystals of* $CdSe_ySI_{-y}$", Physical Review, Vol. 155, Issue 3, pp. 750-763, 1967.

[99] A. Manabe, A. Mitsuishi, and H. Yoshinaga, "*Infrared lattice reflection spectra of II-VI compounds*", Japanese Journal of Applied Physics, Vol. 6, No. 5, pp. 593-600, 1967

[100] S. Ninomiya and S. Adaachi, "Optical properties of wurtzite CdS", Journal of Applied Physics, Vol. 78, Issue 2, pp. 1183-1190, 1995.

[101] P. Shroerer, P. Kriiger, J. Pollman, "Ab initio calculations of the electronic structure of the wurtzite compounds CdS and CdSe", Physical Review B, Vol. 48, Issue 24, pp. 18264-18267,1993.

[102] A. Koyabashi, O. F. Sankey, S. M. Volz, and J. D. Dow, "*Semiempirical tight-binding band structures of wurtzite semiconductors: AlN, CdS, CdSe, ZnS, and ZnO*", Physical Review B, Vol. 28, Issue 2, pp. 935-945, 1983.

[103] R. Geick, C. H. Perry, and S.M. Mitra, "*Lattice Vibrational Properties of Hexagonal CdSe*", Journal of Applied Physics, Vol. 37, Issue 5, pp. 1994-1997, 1967.

[104] R.T. Senger and K.K. Bajaj, "*Optical properties of confined polaronic excitons in spherical ionic quantum dots*", Physical Review B, Vol. 68, pp. 453131-453138, 2003.

[105] Marvin J. Weber, "*Handbook of Optical Materials"*, CRC Press, New York, 2003.

[106] V. Pokalyakin, S. Tereshin, A. Varfolomeev, D. Zaretsky, A. Baranov, A. Banerjee, Y. Wang, S. Ramanathan, and S Bandyopadhyay, "*Proposed model for bistability in nanowire nonvolatile memory*", Journal of Applied Physics, Vol. 97, pp. 124306-1 – 124306-8, 2005.

[107] M. Bass and Optical Society of America, "*Handbook of Optics*", 2nd ed., McGraw-Hill, New York, 1995.

[108] D. W. Thompson, P.G. Snyder, L. Castro, L. Yan, P. Kaipa, J.A. Woollman, "*Optical characterization of porous alumina from vacuum ultraviolet to midinfrared*", Journal of applied physics, Vol. 97, pp. 113511-1 – 113511-9, 2005.

[109] E. S. Kooij, H. Wormeester, A.C. Galca, and B. Poelsema, Electrochemical Solid-State Letters, 6, B52, 2003.

[110] V. S. Dneprovskii, E.A. Zukov, E. Muljarov, S. Tikhodeev, "*Linear and nonlinear excitonic absorption in semiconductor quantum wires crystallized in a dielectric matrix*" Journal of Experimental and Theoretical Physics, Vol. 87, No. 2, pp. 382-387, 1998.

[111] Ch. Greus, A. Forchel, R. Spiegel, F. Faller, S. Benner and H. Haug, "*Phase space filling and band gap renormalization of luminescence of highly excited InGaAs/GaAs quantum wires*", Europhysics Letters, Vol. 34, Issue 3, pp. 213-218, 1996.

[112] V. S. Dneprovskii, E.A. Zukov, "*Strong dynamic Optical nonlinearities of semiconductor quantum wires*", Phys. Stat. Sol., Vol. 206, pp. 469-476, 1998.

[113] L. V. Keldysh, "*Excitons in Semiconductor-Dielectric nanostructures*", Phys. Stat. Sol. (a), Vol. 164, No. 3, pp. 3-12, 1997.

[114] N. S. Rytova, Dokl. Akad. Nauk SSSR, Vol. 163, pp. 1118, 1965.

[115] N. S. Rytova, Sov. Phys. Dokl. Vol. 10, pp. 754, 1966.

[116] A. V. Chaplik and M.V. Entin, Journal of Experimental and Theoretical Physics, Vol. 61, pp. 2469, 1971.

[117] L. V. Keldysh, "*Coulomb interaction in thin semiconductor and semimetal films*", Journal of Experimental and Theoretical Physics Letters, Vol. 29, pp. 658, 1979.

[118] E. A. Mulyarov and S.G. Tikhodeev, N.A. Gippius, T. Ishitara, "*Excitons in self organized semiconductor/insulator supperlattics : PbI-based perovskite compounds*", Physical Review B, Vol. 51, No. 20, pp. 14370-14378, 1994.

[119] E. A. Mulyarov and S.G. Tikhodeev, "*Dielectric enhancement of excitons in semiconducting quantum wires*", Journal of Experimental and Theoretical Physics, Vol. 84, No. 1, pp. 151-155, 1997.

[120] E. A. Muljarov, E.A Zukov, V.S. Dneprovskii, Y. Masumoto, "*Dielectrically enhanced excitons in semiconductor-insulator quantum wires : Theory and Experiment*", Physical Review B, Vol. 62, No. 11, pp. 7420-7432, 2000.

[121] F. Rossi, G. Goldoni, O. Mauritz and E. Molinari, "*Theory of excitonic confinement in semiconductor quantum wires*", J. Phys: Condens. Matter, Vol. 11, pp. 5969-5988, 1999.

[122] G. Goldoni, F. Rossi, E. Molinari, "*Strong exciton binding in quantum structures through remote dielectric confinement*", Physical Review Letters, Vol. 80, No. 22, pp. 4995-4998, 1998.

[123] V. Dneprovskii, S. Gavrilov, E. Muljarov, A. Syrnicov, e. Zukov, "*Optical properties of CdS nanostructures crystallized in the pores of insulating templates*" Proceedings of 9th International Symposium of Nanostructures: Physics and Technology, St. Petersburg, Russia, June 18-22, 2001.

[124] S. A. Gavrilov, V. Gusev, V. Dneprovskii, E. Zukov, A. Syrnikov, I Yaminskii and E. Muljarov, "*Optical properties of excitons in CdS semiconductor-insulator quantum wires*", Journal of Experimental and Theoretical Physics, Vol. 70, pp. 216, 1999.

[125] V. Dneprovskii, E. Zukov, O. A. Shalygina, V.L. Lyaskovskii, E. Muljarov, S. Gavrilov, and Y. Masumoto , "*Excitons in CdS and CdSe semiconducting quantum wires with dielectric barriers*", Journal of Experimental and Theoretical Physics, Vol. 94, No. 6, pp. 1169-1175, 2002.

[126] L. L. "*Young Anodic oxide Films*", Academic Press, New York, 1971.

[127] William E. Courtney, "*Analysis and evaluation of a method of measuring the complex permittivity and permeability of microwave insulators*", IEEE Transactions on Microwave Theory and Techniques, MTT-18, No.8, pp. 476-485, 1970.

[128] S. Lazarouk, S. Katsouba, A. Leshok, A. Demianovich, V. Stanovski, S. Voitech, V. Vysotski, and V. Ponomar, "*Porous alumna as a low-ε insulator for multilevel metallization*", Microelectronic Engineering, Vol. 50, Issue 1-4, pp. 321-327, 2000.

[129] S. Ramanathan and S. Bandyopadhyay, "*Exciton binding energy in semiconductor nanowires in the presence of dielectric de-confinement*", IEEE-Nano2006, Cincinnati, Ohio, July 17-20, 2006.

[130] P. Ils, Ch. Greus, A. Forchel, V.D. Kulakovskii, N.A. Gippius, and S.G. Tikhodeev, "*Linear polarization of photoluminescence emission and absorption in quantum-well wire structures: Experiment and theory*", Physical Review B, Vol. 51, Issue 7, pp. 4272-4277, 1995.

[131] D. Kovalev, M. Chorin, J. Diener, F. Koch, Al.L. Efros, M. Rosen, N.A. Gippius, and S.G. Tikhodeev, "*Porous Si anisotropy from photoluminescence polarization",* *A*pplied Physics Letters, Vol. 67, Issue 11, pp. 1585-1587, 1995.

[132] Gregory B. Tait and David B. Amin, "*Barrier-enhanced InGaAs/InAlAs photodetectors using quantum well intermixing*", Solid State Electronics, Vol. 48, pp. 1783-1790, 2004.

[133] D.A.B. Miller, D.S. Chemla, T.C. Damen, A.C. Gossard, W. Wiegmann, T.H. Wood, and C.A. Burrus, "*Band-edge electroabsorption in quantum well structures : The quantum confined Stark effect*", Physical Review Letters, Vol. 53, No. 22, pp. 2173-2176, 1984.

[134] D.A.B. Miller, D.S. Chemla, S. Schmitt-Rink, "*Relation between electroabsorption in bulk semiconductor and in quantum wells : The quantum confined Franz-Keldysh effect*", Physical Review B, Vol. 33, No. 10, pp. 6976-6982, 1986.

[135] D.A.B. Miller, D.S. Chemla, T.C. Damen, A.C. Gossard, W. Wiegmann, T.H. Wood, and A.C. Burrus, "*Electric field dependence of optical absorption near the band gap of quantum-well structures*", Physical Review B, Vol. 32, Issue 2, pp. 1043-1060, 1985.

[136] N.B. An, And H. Haug, "*Theory of excitonic optical Stark effect in quasi-one-dimensional semiconductor quantum wires*", Physical Review B, Vol. 46, No. 15, pp. 9569-9576, 1992.

[137] S. M. Sze, "*Physics of semiconductor devices*", 2nd edition, A Wiley-Interscience publication, New York, 2004.

[138] N. Grandjean, B. Damilano, S. Dalmasso, M. Leroux, M. Laugt, J. Massies, "*Built-in electric field in wurtzite AlGaN/GaN quantum wells*", Journal of applied physics, Vol. 86, No. 7, pp. 3714-3720, 1999.

[139] S. Ramanathan, S. Patibandla, S. Bandyopadhyay, "*Flourescence and infrared spectroscopy of electrochemically self assembled ZnO nanowires:Evidence of quantum confined Stark effect*", Journal of material Science: Materials in Electronics, to be published.

[140] S. Bandyopadhyay, A.E. Miller, H.C. Chang, G. Banerjee, V. Yuzhakov, D.F. Yue, R.E. Ricker, S. Jones, J.A. Eastman, E. Baugher, and M. Chandrasekhar, "*Electrochemically assembled quasi-periodic quantum dot arrays*", Nanotechnology, Vol. 7, pp. 360-371, 1996.

[141] A. Balandin, K.L. Wang, N. Kouklin, and S. Badyopadhyay, "*Raman Spectroscopy of electrochemically self-assembled CdS quantum dots*", Applied Physics Letters, Vol. 76, No. 2, pp. 137-139, 2000.

[142] Y. Wang, S. Ramanathan, Q. Fan, F. Yun, H. Morcoc, and S. Bandyopadhyay, "*Electric field modulation of infrared absorption at room temperature in electrochemically self assembled quantum dots*", Journal of Nanoscience and Nanotechnology, Vol. 6, pp. 1-4, 2006.

[143] R. Tsu, and L. Ioriatti, "Longitudinal dielectric constant for quantum wells", Superlattices and Microstructures, Vol. 1, No. 4, pp. 295-297, 1985.

[144] R. Tsu, D. Babic, and L. Ioriatti, "Simple model for the dielectric constant of nanoscale silicon particle", Journal of Applied Physics, Vol. 82, No. 3, pp. 1327-1329, 199).

[145] G. Bastard, “Hydrogenic impurity sates in a quantum well: A simple model”, Physical Review B, Vol. 24, pp. 4714-4722, 1981.

[146] L.W. Wang and A. Zunger, “Dielectric constants of silicon quantum dots”, Physical Review Letters, Vol. 73, No. 7, pp. 1039-1042, 1994.

[147] A. D. Yoffe, “Low-dimensional systems: Quantum size effects and electronic properties of semiconductor microcrystallites (zero-dimensional systems) and some quasi-two-dimensional systems”, Advances in Physics, Vol. 42, No. 2, pp. 173-262, 1993.

VITA

Rajesh A. Katkar was born in a small town of Katol in central India in July, 1978. Brought up in the city of Nagpur, he received his Bachelor of Engineering degree (in Electronics and Power) from National Institute of Technology, Nagpur, India in May 2000. Later, he joined a premier automobile manufacturing company, Bajaj Auto Ltd. in Pune as an Electrical Engineer, and also briefly worked for Mahindra British Telecom Ltd. as a software Engineer. He came to VCU School of Engineering as a graduate student and received his M.S. degree in 2003.